CUKUROVA UNIVERSITY
INSTITUTE OF NATURAL AND APPLIED SCIENCES

PhD THESIS

Aerodynamic Investigation and Flow Control on DrivAer Models Using Numerical (CFD) Methods

Oğuz BAŞ

Automotive Engineering Department

April, 2023

CUKUROVA UNIVERSITY

INSTITUTE OF NATURAL AND APPLIED SCIENCES

PhD THESIS APPROVAL

Aerodynamic Investigation and Flow Control on DrivAer Models Using Numerical (CFD) Methods

---

Oğuz BAŞ

Automotive Engineering Department

This Doctorate Thesis was evaluated by the following Jury Members on …/.../…… and was approved by unanimity / majority of votes.

Jury	: Assoc. Prof. Dr. M. Atakan AKAR	(Advisor)	…………
	: Prof. Dr. Name SURNAME		…………
	: Assoc. Prof. Dr. Name SURNAME		…………
	: Assoc. Prof. Dr. Name SURNAME		…………
	: Asst. Prof. Dr. Name SURNAME		…………

This Thesis was written in the Department of Automotive Engineering, Institute of Natural and Applied Sciences.
Thesis Number:

Prof. Dr. Sadık DİNÇER
Director
Institute of Natural and Applied Sciences

This work was supported by the XXXXX.
Project ID: XXX-XXXX-XXXX

CONTENTS

CUKUROVA UNIVERSITY
INSTITUTE OF NATURAL AND APPLIED SCIENCES

PhD THESIS

Aerodynamic Investigation and Flow Control on DrivAer Models Using Numerical (CFD) Methods

Oğuz BAŞ

Advisor: Assoc. Prof. Dr. Mustafa Atakan AKAR
2nd Advisor: Prof. Dr. Coşkun ÖZALP

Department of Automotive Engineering

ABSTRACT

Drag reduction is one of the most critical subjects for vehicles, especially considering the emerging trend of electric vehicles that have been known to drive range and efficiency issues. In this work, deflector plates were tested numerically as a passive flow control element at the upper and lower regions of the rear end of the closed body estateback, fastback, and notchback DrivAer generic car models. Plate slant angles varied to find optimum deflectors. CFD simulations have been conducted by the k-ω SST RANS turbulence model and the setup of the base model is verified with the drag force coefficient of previous experimental works. Then, parametric, genetic algorithm response surface and adjoint optimization stages were applied on the upper and lower deflectors, respectively. Consequently, simultaneous usage of these two deflectors with optimum angles resulted in reductions of C_D by 17.90%, 4.82%, and 7.25% for estateback, fastback, and notchback respectively. However, detailed qualitative analysis is shown that upper and lower deflectors have different drag reduction mechanisms at the wake. The upper deflector reduces wake statistics and attains pressure recovery at the back surface by improved downwash for all models. On the other hand, the lower deflector restricts airflow beneath the car for the estateback. Hereby, this provides pressure recovery at the slanted diffuser section by blocking its functionality while the restricted airflow is deflected to the upperbody and results in pressure recovery at the rear surface, too by improved upwash, although it increases the wake region. For the fastback model, the lower deflector provides flow control by improving the upwash, while for the notchback model, it provides a flow control by preventing the flow interaction between the downwash and the upwash.

Keywords: Drag, Lift, Aerodynamic, DrivAer, Deflector.

ÇUKUROVA ÜNİVERSİTESİ
FEN BİLİMLERİ ENSTİTÜSÜ

DOKTORA TEZİ

DrivAer Modellerinde Sayısal (CFD) Yöntemlerle Aerodinamik İnceleme ve Akış Kontrolü

Oğuz BAŞ

Danışman: Doç. Dr. Mustafa Atakan AKAR
2. Danışman: Prof. Dr. Coşkun ÖZALP

Otomotiv Mühendisliği Anabilim Dalı

ÖZ

Sürüklemenin azaltılması, özellikle menzil ve verimlilik sorunları yarattığı bilinen elektrikli araçların yükselen trendi düşünüldüğünde, araçlar için en kritik konulardan biridir. Bu çalışmada, saptırıcı plakalar, DrivAer jenerik araba modellerinin kapalı gövdeli estateback, fastback ve notchback modellerinin arka ucunun üst ve alt bölgelerinde pasif akış kontrol elemanı olarak sayısal olarak test edilmiştir. Plaka eğimi, optimum saptırıcıları bulmak için parametrize edilmiştir. CFD simülasyonları k-ω SST RANS türbülans modeli ile gerçekleştirilmiş ve temel modelin benzetimi önceki deneysel çalışmaların sürükleme kuvveti katsayısı ile doğrulanmıştır. Ardından parametrik, genetik algoritmalı yanıt yüzeyi ve eklenik optimizasyon aşamaları sırasıyla üst ve alt saptırıcılar üzerinde uygulanmıştır. Sonuç olarak, bu iki deflektörün optimum açılarla aynı anda kullanılması, C_D değerlerinde, station, fastback ve notchback için sırasıyla %17,90, %4,82 ve %7,25 oranında azalma sağlamıştır. Bununla birlikte, ayrıntılı niteliksel analiz, üst ve alt saptırıcıların izde farklı sürükleme azaltma mekanizmalarına sahip olduğunu göstermektedir. Üst deflektör, tüm modellerde, art izi istatistiklerini azalmış ve iyileştirilmiş aşağı akım ile arka yüzeyde basınç geri kazanımı sağlamıştır. Öte yandan, alt deflektör estateback modelinde, araç altındaki hava akışını kısıtlar. Böylelikle eğimli difüzör bölümünde, kısıtlı hava akımı üst gövdeye saptırılırken işlevselliğini bloke ederek basınç geri kazanımı sağlar ve iz bölgesini artırmasına rağmen iyileştirilmiş yukarı akım ile arka yüzeyde de basınç geri kazanımı sağlamıştır. Fastback modelinde alt saptırıcı yukarıakımı iyileştirerek akış kontrolü sağlarken, notchback modelinde ise aşağıakım ve yukarıakım arasında etkileşimi engelleyerek akış kontrolünü sağlamıştır.

Anahtar Kelimeler: Sürükleme, Kaldırma, Aerodinamik, DrivAer, Saptırıcı.

EXTENDED ABSTRACT

Minimizing energy consumption is the main concern in the automotive industry to improve efficiency and pollute the environment less. Generally, there are several approaches to improve vehicle efficiency such as increasing the performance of the engine, reduction of the vehicle weight, and minimizing the aerodynamic drag. In the WLTP driving cycle, it has been shown that fuel consumption can be decreased by 3.3% when %10 mass reduction obtained. When the aerodynamic drag coefficient (C_D) of a car with a C_D=0.3 is reduced by %10, fuel efficiency can be enhanced by 2.6%. Material improvement and engine downsizing strategies can reduce mass; however, this would cause to remarkable cost rise. Shape modifications on the exterior body can be alternative cost-effective strategy for obtaining the better fuel efficiency.

Approximately 50-70% of the total power is consumed to overcome the aerodynamic drag by a vehicle at 100 km/h. Investigations show that minimizing C_D by 10% may lead to a 5% reduction in fuel consumption for ICE vehicles. On the other hand, with the trend of electrical vehicles (EV), scientists and the automotive industry focus to ameliorate EV components electrical motors, batteries, and their management systems recently since the main problem of EVs is the driving range. Aerodynamic performance improvement is a way to overcome this issue. Hence, reducing C_D by 10% can increase the driving range for EVs by up to 5%. So, improving the aerodynamic performance of a vehicle has a significant effect on improving efficiency and can reduce barriers to electric vehicle adoption. Besides, the aerodynamic performance of a vehicle is not only responsible for reducing energy consumption but also for handling, stabilization, and driving performance in the sense of downforce (of lift coefficient C_L), and side forces.

For these purposes, in the research and improvement investigations of vehicle aerodynamics performed for many years, the Ahmed body, which has dimensions similar to a ground vehicle, has been the subject of research. Because of the simple shape of these generic models, they have been studied in numerous investigations to elucidate flow characteristics and improve the aerodynamic performances of these models. Additionally, their being open source to literature led to the adoption of generic models widespread. Researchers have been able to share and verify their works utilizing these models. For instance, because of sharing experimental data with the ERCOFTAC database, it is possible to verify not only aerodynamic force coefficients but also the flow profiles of Ahmed body.

Nonetheless, generic models are too abstract and far from reflecting the shapes of streamlined passenger vehicles these days. Application of flow control strategies and methods which were tested on generic models directly to the production cars may be rather optimistic and not feasible. On the other hand, despite there being some rare studies, mass-production vehicles are not open-source and brands are generally distant to share CAD data of their models due to concerns about privacy policies of their know-how. Moreover, these rare studies are far from creating

widespread literature. At this point, BMW and AUDI AG in cooperation with the Technical University of Munich presented a new realistic and representative generic car model, namely DrivAer to close this gap in 2011. The first findings in the preliminary studies have shown that DrivAer models are more representative and have realistic flow properties similar to production cars. With the introduction of DrivAer, automotive aerodynamic literature got a realistic, relatively simple enough that researchers can focus on, an open-source model.

DrivAer ground vehicle model has various configurations such as estateback, notchback, and fastback in the sense of rear-end design; wheelless, smooth wheeled, and detailed wheeled (with rims) in the sense of wheel inclusion; smooth and detailed underbody designs; mirrored and without mirrors: open-grilled and closed grilled in the sense of air induction of engine compartment. These interchangeable parameters allow to researchers choose the desired configuration according to their focal points, demands, and facilities.

Passive flow control methods are advantageous over the active flow control methods in that they do not require extra energy from the outside. However, passive methods do not react to flow changes such as flow separation, force requirements in various conditions, and air-flow velocity except for flexible add-on components. Their efficiencies are questionable and may decline for variable-state applications.

Since the introduction of the DrivAer model, whether active or passive, various flow control strategies have been started to test for these realistic bodies. Dimpling, vortex generators, tailpipe positioning, and fluidic oscillators are some of these active and passive flow control methods implemented on realistic car models.

A deflector, as the name implies, is a flow control method that tries to improve aerodynamic properties by directing the airflow from one direction to another desired direction. They can be mounted in different regions of a vehicle such as wheel fronts, windows, rear ends, mirrors etc. Deflectors which are the focal point of this paper have been one of the most frequently studied flow control strategies.

From this point of view, the application and optimization of deflectors mounted to the rear end of a realistic model are deficient in automotive aerodynamic literature considering the introduction of the realistic DrivAer models. In this work, efficiencies of deflectors mounted on the upper and lower closed-body DrivAer estateback, fastback, and notchback generic models were investigated. Upwash and downwash flow of the vehicle models were tried to be controlled by upper and lower deflectors with optimum angle. Optimum deflector angles were tried to find out for design objective of minimum drag, numerically by commercial tool of Ansys Fluent CFD code. Step-by-step optimization procedure was followed taking advantage of the positive aspects of optimization techniques and avoiding their disadvantages. Parametric, response surface with genetic algorithm, and adjoint optimizations were performed, respectively. With parametric optimization, global minimum was sought without additional computational cost, mesh problems, and convergency issues of adjoint tool. Then, parametric optimization data set was used as DOE for response surface. At the response surface optimization stage, global minimum of drag coefficients of DrivAer models were reached further. Finally, flow simulations of response surface optimized models were used as primal solutions. Five design iterations were performed to obtain optimum design of combined upper and lower deflectors on DrivAer models.

Grid independence tests were performed using numerical techniques of Richardson extrapolation and Grid Convergency Index for three different mesh levels. To assure desired levels of accuracy, 4^{th} and a new mesh resolution was generated by using these techniques. With this mesh level, GCI values were kept GCI<1 and drag coefficient results of the base estateback, fastback, and notchback models were resulted in good accuracy with experimental data.

As a result of response surface simulations, DrivAer models with the optimum designed upper and lower deflectors were obtained. Beside these two configurations for each DrivAer model, combined upper and lower deflector on models was improved by adjoint tools, hence upper + lower model has attained. Detailed qualitative and quantitative investigations on base, upper, lower, and upper + lower models were conducted to find drag reduction mechanisms of the flow control elements.

Consequently, simultaneous usage of these two deflectors with optimum angles resulted in reductions of C_D by 17.90%, 4.82%, and 7.25% for estateback, fastback and notchback respectively. However, detailed qualitative analysis is shown that upper and lower deflectors have different drag reduction mechanisms at the wake. The upper deflector reduces wake statistics and attains pressure recovery at the back surface by improved downwash for all models. On the other hand, the lower deflector restricts airflow beneath the car for estateback model. Hereby, this provides pressure recovery at the slanted diffuser section by blocking its functionality while the restricted airflow is deflected to the upperbody and results in pressure recovery at the rear surface, too by improved upwash, although it increases the wake region. For the fastback model, the lower deflector provides flow control by improving the upwash, while for the notchback model, it provides a flow control by preventing the flow interaction between the downwash and the upwash.

With this study, deflectors can be a remedy for improving vehicle efficiency. Considering heavy batteries of EV, driving range can be extended and increased lift can be compensated by the weight of batteries without sacrificing downforce.

GENİŞLETİLMİŞ ÖZET

Verimliliği artırmak ve çevreyi daha az kirletmek için otomotiv endüstrisinde enerji tüketiminin en aza indirilmesi gerekmektedir. Genel olarak, motor performansını artırmak, araç ağırlığını azaltmak ve aerodinamik sürtünmeyi en aza indirmek gibi verimliliği artırmak için çeşitli yaklaşımlar vardır. WLTP sürüş çevriminde, %10 kütle azaltımı yapıldığında yakıt tüketiminin %3.3 oranında azaltılabileceği gösterilmiştir. Öte yandan, C_D=0.3 olan bir arabanın aerodinamik sürükleme katsayısı (C_D) %10 azaltıldığında, yakıt verimliliği %2.6 oranında iyileştirilebilir. Malzeme geliştirme ve motor küçültme stratejileri kütleyi azaltabilir; ancak, bu dikkate değer bir maliyet artışına neden olacaktır. Dış gövde üzerindeki şekil değişimleri, daha iyi yakıt verimliliği elde etmek için gelecekte daha da alternatif ve uygun maliyetli bir strateji olabilir.

Toplam gücün yaklaşık %50-70'i, bir araç tarafından 100 km/s hızla aerodinamik sürtünmeyi yenmek için tüketilir. Araştırmalara göre C_D'nı %10 oranında düşürmenin, içten yanmalı motorlu araçlar için yakıt tüketiminde %5'lik bir azalma sağlayabilmektedir. Öte yandan, elektrikli araçların (EV) yükselen trendi ile bilim adamları ve otomotiv endüstrisi, EV' ların ana sorunu sürüş menzili problemini çözmek için, son zamanlarda EV bileşenlerini, elektrik motorlarını, pilleri ve batarya yönetim sistemlerini iyileştirmeye odaklanmaktadır. Aerodinamik performansı iyileştirme, bu sorunun üstesinden gelmenin yollarından biridir. Bu nedenle, C_D'yi %10 azaltmak, EV'ler için sürüş menzilini %5'e kadar artırabileceği bilinmektedir. Öte yandan, bir aracın aerodinamik performansını iyileştirmenin, verimliliği artırmada önemli bir etkisi vardır ve elektrikli araç kullanımının önündeki engelleri azaltacağı düşünülmektedir. Ayrıca, bir aracın aerodinamik performansı sadece enerji tüketimini azaltmakla kalmamakta, aynı zamanda yere basma kuvveti (C_L kaldırma katsayısı) ve yan kuvvetler anlamında yol tutuşu, stabilizasyon ve sürüş performansını da ilgilendirmektedir.

Bu doğrultuda uzun yıllardır araç aerodinamiği ile ilgili yapılan araştırma ve iyileştirme çalışmalarında bir kara aracına benzer boyutlara sahip olan Ahmed gövdesi araştırma konusu olmuştur. Bu jenerik modellin basit şekli nedeniyle, akış özelliklerini araştırmak ve bu modellerin aerodinamik performanslarını iyileştirmek için çok sayıda çalışma gerçekleştirilmiştir. Ayrıca literatüre açık kaynak olmaları, jenerik modellerin yaygınlaşmasını sağlamıştır. Araştırmacılar bu modelleri kullanarak çalışmalarını paylaşabilir ve doğrulayabilirler. Örneğin, deneysel verilerin ERCOFTAC veri tabanı ile paylaşılması sayesinde, Ahmed gövdesinin sadece aerodinamik kuvvet katsayılarını değil, aynı zamanda akış profillerini de doğrulamak mümkündür.

Bununla birlikte, bu jenerik modeller çok soyut ve günümüzün aerodinamik binek araçlarının şekillerini yansıtmaktan uzaktır. Jenerik modeller üzerinde test edilen akış kontrol stratejilerinin ve yöntemlerinin doğrudan üretim arabalarına uygulanması oldukça iyimser bir yaklaşım olmaktadır. Öte yandan, bazı nadir çalışmalar olmasına rağmen, seri üretim araçlar açık kaynaklı değildir ve markalar, know-how ve gizlilik politikalarıyla ilgili endişeler nedeniyle modellerinin CAD verilerini paylaşmaktan genellikle uzak dururlar. Üstelik bu nadir çalışmalar yaygın bir literatür oluşturmaktan uzaktır. Bu noktada BMW ve AUDI AG, Münih Teknik Üniversitesi ile iş birliği içinde, 2011 yılında bu açığı kapatmak için DrivAer adlı yeni gerçekçi ve temsili bir jenerik otomobil modeli sunmuştur. Ön çalışmalardaki ilk bulgular, DrivAer modellerinin kullanılmasının aerodinamik literatürü için daha gerçekçi olduğunu göstermiştir günümüz araçlarına benzer gerçekçi akış özelliklerine sahip olduğu ortaya koyulmuştur. DrivAer'in tanıtılmasıyla birlikte, otomotiv aerodinamiği literatürü gerçekçi, araştırmacıların odaklanabileceği kadar basit, açık kaynaklı bir modele kavuşmuştur.

DrivAer kara aracı modeli, arka tasarımında estateback, notchback, fastback; tekerlek tasarımında tekerleksiz, düz tekerlekli ve gerçekçi tekerlekli (jantlı); gövde altı tasarımında pürüzsüz ve detaylı gövde altı tasarımları; aynalı ve aynasız, hava girişi tasarımında açık-ızgara ve kapalı ızgara gibi farklı konfigürasyonlara sahiptir. Bu değiştirilebilir parametreler, araştırmacıların odak noktalarına, taleplerine ve olanaklarına göre istenen konfigürasyonu seçmelerine olanak tanımaktadır.

Pasif akış kontrol yöntemleri, dışarıdan ekstra bir enerji gerektirmemesi bakımından aktif akış kontrol yöntemlerine göre avantajlıdır. Bununla birlikte, pasif yöntemler, esnek tasarımlı pasif akış kontrolleri dışında, akış ayrımı, çeşitli koşullardaki kuvvet gereksinimleri ve hava akış hızı gibi akış değişikliklerine tepki vermez. Verimlilikleri bu bakımdan değişken durumlu uygulamalar için düşebilmektedir.

Öte yanda, DrivAer modelinin tanıtılmasından bu yana, aktif ve pasif çeşitli akış kontrol stratejileri bu gerçekçi araç modellerinde test etmeye başlanmıştır. Çukurcuklama, girdap üreteçleri, egzoz borusu konumlandırma ve akışkan osilatörler, gerçekçi araba modellerinde uygulanan bu aktif ve pasif akış kontrol yöntemlerinden bazılarıdır.

Bu noktadan hareketle, gerçekçi jenerik modellerinin ortaya çıktığı zamandan itibaren, gerçekçi bir modelin arka ucuna monte edilen deflektörlerle akış kontrolü uygulanması ve optimizasyonu, otomotiv aerodinamik literatüründe eksiktir. Bu çalışmada, kapalı gövde DrivAer estateback, fastback ve notchback jenerik modellerinin üst ve alt arka ucuna monte edilen deflektörlerin verimliliğini araştırılmıştır. Araç modellerinin yukarı ve aşağı yönlü akımları, optimum açıya sahip üst ve alt deflektörler tarafından kontrol edilmeye çalışılmıştır. Minimum aerodinamik sürüklenme elde etmek amacıyla, Ansys Fluent CFD ile optimum saptırma açıları bulunmaya çalışıldı. Optimizasyon tekniklerinin olumlu yönlerinden yararlanarak ve dezavantajlarından kaçınarak adım adım optimizasyon prosedürü izlendi.

Parametrik, genetik algoritmalı yanıt yüzeyi ve eşlenik optimizasyon aşamaları sırasıyla gerçekleştirilmiştir. Parametrik optimizasyonla, eşlenik optimizasyonda karşılaşılan ek hesaplama maliyeti, ağ sorunları ve yakınsama sorunları olmadan global minimum sonuç elde edilmeye çalışılmıştır. Daha sonra yanıt yüzeyi için DOE olarak parametrik optimizasyon veri seti kullanılmıştır. Yanıt yüzeyi optimizasyonu aşamasıyla, DrivAer modellerinin sürükleme katsayıları için global minimum daha da yaklaşılmıştır. Son olarak, yanıt yüzeyiyle optimize edilmiş modeller, eklenik optimizasyonun akış simülasyonları birincil çözümler olarak kullanıldı. DrivAer modellerinde kombine üst ve alt deflektörlerde optimum tasarımı elde etmek için beş tasarım eklenik optimizasyonu gerçekleştirilmiştir.

Ağdan bağımsızlık testleri, üç farklı ağ seviyesi için Richardson ekstrapolasyonu ve ağ yakınsama indeksi sayısal teknikleri kullanılarak yapılmıştır. İstenilen doğruluk seviyelerini sağlamak için bu teknikler kullanılarak 4. ve yeni bir ağ çözünürlüğü oluşturulmuştur. Bu ağ seviyesi ile GCI değerleri için GCI<1 şartı sağlanmış ve baz estateback, fastback ve notchback modellerinin sürükleme katsayısı sonuçları deneysel verilerle iyi bir doğrulukla modellenebilmiştir. Yanıt yüzeyi simülasyonları sonucunda optimum tasarımlı üst ve alt deflektörlere sahip DrivAer modelleri elde edilmiştir. Her DrivAer modeli için bu iki konfigürasyonun yanı sıra, modellerdeki kombine edilmiş üst ve alt saptırıcı, eklenik optimizasyonu ile geliştirilmiş ve nihai üst + alt model elde edilmiştir. Akış kontrol elemanlarının sürüklenmeyi azaltma mekanizmalarını araştırma için baz, üst, alt ve üst + alt modeller üzerinde ayrıntılı nitel ve nicel araştırmalar yapılmıştır.

Sonuç olarak, bu iki deflektörün optimum açılarla eşzamanlı kullanımı, estateback, fastback ve notchback modelleri için sırasıyla, C_D'nın %17.90, % 4.82 ve % 7.25 oranında azalmasını sağlamıştır. Bununla birlikte, ayrıntılı nitel analizler, üst ve alt deflektörlerin araç arkasındaki art izinde farklı sürükleme azaltma mekanizmalarına sahip olduğunu göstermiştir. Üst saptırıcı, tüm modeller için geliştirilmiş aşağı akım ile art izi istatistiklerini azaltış ve arka yüzeyde basınç geri kazanımı sağlamıştır. Öte yandan, alt saptırıcı, estateback modeli için arabanın altındaki hava akışını kısıtlayıp, difüzörün verimliliğini azaltarak eğimli araç altındaki bu eğimli yüzeyde basınç geri kazanımı sağlamıştır. Diğer taraftan, fastback DrivAer modelinde alt saptırıcı, yukarı akımı iyileştirerek akış kontrolü sağlarken, notchback modelinde ise aşağı akım ve yukarı akım arasındaki akış etkileşimini engelleyerek akış kontrolü sağlar.

Bu çalışma ile deflektörler, araç verimliliğini artırmak için bir çözüm olabileceği ortaya çıkmıştır. EV' ların ağır aküleri göz önüne alındığında, sürüş menzili uzatılabileceği ve artan kaldırma kuvvetiyle akülerin ağırlığının getirdiği ekstra yuvarlanma direnci kuvveti, yere basma kuvvetinden ödün vermeden azaltılabilir.

ACKNOWLEDGEMENTS

First of all, I would like to thank to my supervisor, Assist. Prof. Dr. Mustafa Atakan AKAR, for his support and encouragement throughout preparation of this thesis.

I sincerely thank Prof. Dr. Coşkun ÖZALP for sharing his knowledge and valuable time for this work.

I would like to heartfelt thank Salih Berkan AYDEMİR, Umut KUMLU, Arif Emre AKTAŞ, and Sinan KEİYİNCİ for their support and effective advice.

I would like to thank all my research assistant friends and all staff of Automotive Engineering Department at Çukurova University and Faculty of Engineering at Amasya University for their continuous support and motivation.

Finally, I want to dedicate this thesis my daughter, Beren BAŞ my wife, Meryem Ceren ERTOP BAŞ and my parents; Rafet BAŞ, Leyla BAŞ, and my brother İlkay BAŞ, my father-in law Metin ERTOP, my mother-in-law Zübeyde ERTOP. I wouldn’t have succeeded my thesis without their support and encouragement.

LIST OF TABLES

LIST OF FIGURES

LIST OF ABBREVIATIONS AND NOMENCLATURE

A	: Reference area (m^2)
A_F	: Frontal area (m^2)
C_D	: Drag coefficient
C_L	: Lift coefficient
C_P	: Coefficient of pressure
CFD	: Computational Fluid Dynamics
bhp	: Brake Horsepower (hp)
CAD	: Computer-Aided Design
CO	: Carbon Monoxide
CO_2	: Carbon Dioxide
EV	: Electrical Vehicles
F_D	: Aerodynamic Drag Force
F_L	: Aerodynamic Lift Force
ICE	: Internal Combustion Engine
kg-f	: Kilogram-Force
Km/h	: Kilometer per hour
kW	: Kilowatt
kWh	: Kilowatt-hour
N	: Newton
P_D	: Drag power consumption (kW)
P_s	: Estimated fuel saving rate (%)
Q_s	: Estimated power saving (kW)
RANS	: Reynolds-Averaged Navier-Stokes
SUV	: Sports Utility Vehicle
TKE	: Turbulent Kinetic Energy (m^2/s^2)
TKE_{ave}	: Average Turbulent Kinetic Energy (m^2/s^2)
TKE_{max}	: Peak Value of the Turbulent Kinetic Energy (m^2/s^2)
U	: Free stream velocity (m/s)
W_A	: Area covered by Negative X-component Velocity (m^2)
WLTP	: Worldwide Harmonized Light Vehicle Test Procedure
ρ	: Density (kg/m^3)
γ	: Slant angle of Ahmed body

1. INTRODUCTION

Minimizing energy consumption is the main concern in the automotive industry to enhance efficiency and pollute the environment less. Generally, there are several approaches to improve efficiency such as increasing the performance of the engine, reduction of the vehicle weight, and minimizing the aerodynamic drag. In the WLTP driving cycle, it has been shown that fuel consumption can be reduced by 3.3% when a %10 mass reduction is conducted. When the aerodynamic drag coefficient (C_D) of a car with a C_D=0.3 is reduced by %10, fuel efficiency can be improved by 2.6% (Mock et al., 2014). Material improvement and engine downsizing strategies can reduce mass; however, this would cause to remarkable cost rise. Shape modifications on the exterior body can be an alternative cost-effective strategy for obtaining better fuel efficiency.

Approximately 50-70% of the total power is consumed to overcome the aerodynamic drag by a vehicle at 100 km/h (Katz, 2016). Another important investigation reports that minimizing C_D by 10% may lead to a 5% reduction in fuel consumption for ICE vehicles (Bayındrılı et al., 2018). On the other hand, with the trend of electrical vehicles (EV), scientists and the automotive industry focus to ameliorate EV components electrical motors, batteries, and their management systems recently since the main problem of EVs is the driving range. Aerodynamic performance improvement is a way to overcome this issue. Hence, reducing C_D by 10% can increase the driving range for EVs by up to 5% (D'Hooge et al., 2012; Palin et al., 2012). So, improving the aerodynamic performance of a vehicle has a significant effect on improving efficiency and can reduce barriers to electric vehicle adoption. Besides, the aerodynamic performance of a vehicle is not only responsible for reducing energy consumption but also for handling, stabilization, and driving performance in the sense of downforce (of lift coefficient C_L), and side forces.

1.1. The history of aerodynamics

Aerodynamics is a science and subfield of gas dynamics and fluid mechanics which investigates the relationship between a moving object and the airflow around it. Although modern aerodynamics only dates to the 17th century, aerodynamic forces have aroused the attention of humans for thousands of years in sailboats and windmills, and images and stories of flight appear throughout recorded history, such as the Ancient Greek legend of Icarus and Daedalus. Fundamental issues in fluid mechanics such as continuum, drag, and pressure gradients can be seen in the work of Aristotle and Archimedes (Anderson, 1997).

Isaac Newton, one of the prior aerodynamicists was the first person to present a theory of air resistance, in 1726. Following to development of this theory, Swiss-Dutch scientists Daniel Bernoulli described the fundamentals of the relationship between pressure, density, and flow velocity for incompressible flow known today as Bernoulli's principle in 1738 with Hydrodinamica that allow us a method for determining lift force.

In 1757, the general formula of the Leonhard Euler was developed known as Euler equations that can be applied to both incompressible and compressible flow types. After that, these equations were extended by the inclusion of viscosity effects and consequently Navier-Stokes equations were found out in the early 19^{th} century. These nonlinear differential equations are the most general governing equations which can be applied to all types of flows however, it has not been still possible to solve them analytically for most cases.

In 1799, George Cayley identified the main four aerodynamic forces of an aircraft (weight, lift, drag, and thrust), and explained the relationships between them. His findings led the way for obtaining heavier flights for the next century. In 1871, Francis Herbert Wenham was the first person to construct a wind tunnel that achieved almost precise measurements of aerodynamic forces.

In 1889, a French aeronautical engineer Charles Renard predicted the power required to sustain a stable flight. After that, Otto Lilienthal succeeded notably by flying with glider flights, as well as inventing a thin, curved airfoil that produces higher lift force and comparably low drag force. Afterward of these developments and besides research conducted in their wind tunnel, the Wright brothers went down in history by accomplishing a flight with the first powered airplane on December 17, 1903 (Cengel and Cimbala, 2006).

Martin Kutta, Frederick Lanchester, and Nikolai Zhukovsky independently created their theories that related to the circulation of a fluid flow to generate lift, throughout the time of the first flights. Kutta and Zhukovsky were the first scientists that develop a two-dimensional wing theory. Ludwig Prandtl was able to reveal the mathematics behind thin-airfoil and lifting-line theories as well as understand the physics of boundary layers with the extensions of the work of Lanchester. After all these developments, aerodynamics scientists began to be confronted with problems related to air compressibility at speeds near the speed of sound as aircraft speed increased.

Controlling the aircraft, drag force rise due to shock waves, and the risk of structural failure due to aeroelastic vibrations were among these problems and these resulted from airflow characteristic differences under such conditions. Ernst Mach, investigating the properties of the supersonic flow, is the first person who identified the Mach number which is the ratio of the flow speed to the speed of sound. Jakob Ackeret developed early studies of the calculation of the lift and drag forces of supersonic airfoils, while Pierre Huguenot and Macquorn Rankine independently led the initial work of determining flow properties before and after a shock wave. Hugh L. Dryden and T. von Kármán developed the transonic term to describe speeds of flow between the critical Mach number. When the Mach number is higher than 1, drag force increases so rapidly that aerodynamicists and aviators were in agreement with the impossibility of successful supersonic flight until the sound barrier was broken in 1947 using the Bell X-1 aircraft. Scientists' knowledge of the subsonic and low supersonic flow had matured by the time the sound barrier was broken. High-performance aircraft evolved more and more during the Cold War.

In the 1940s, Computational fluid dynamics (CFD) began to be considered as a path to determine flow properties around complex objects. With the validation of numerical analysis results by the wind tunnel and flight tests, even entire aircraft design procedures could start to be carried out using CFD methodology. Moreover, scientists understanding of supersonic and hypersonic flows have been continued to mature since the 1960s. The way aerodynamicists aim has changed from understanding fluid flow behavior to equipping flight with such devices that determining and even manipulating the fluid flow would be possible. Aerodynamicists' motivation continues practical issues such as aircraft design for supersonic and hypersonic conditions, to ameliorate the current aircraft aerodynamic efficiency and propulsion systems. At the same time, theoretical investigations are carried out on essential issues in basic aerodynamic theory related to flow turbulence and the absence of analytical solutions for the Navier–Stokes equations, too.

Almost all the phenomenon in nature and on the earth is related to fluids or aerodynamics; weather, ocean flows, human organs such as the heart or lungs, or the flow of concrete and metals. Considering that this science has an impact on everything in life, it is inevitable that it will have important effects on automobiles. For automobiles, aerodynamics relates to ventilation/ air-conditioning, engine intake, exhaust flows, brake cooling, and exerted forces on the vehicle.

The drag force increases significantly with the vehicle speed. This fact was started to be considered in the 1920s by engineers and they start to find a way of reducing aerodynamic drag force at higher speeds by improving vehicle shape. By the 50s, German and British engineers became aware of the effects of drag force on a higher-performance car. On the other hand, an interesting product is residing in the German Museum in Munich, named Tropfenwagen (Figure 1.1). The creator of this interesting car, E. Rumpler, designed such a product that both the vehicle cabin and its body had a teardrop shape to minimize aerodynamic drag force on the whole body. Not only considering its debut in 1924 and its unique shape in those years but also the tested drag coefficient is superior to most modern cars and was found at $C_D = 0.28$ which was measured in the VW AG wind tunnel in 1979 making this car interesting. The Thopfenwagen car was then equipped with a mid-engine layout by racecar automotive engineers in the 1960s. However, this has resulted in commercial failure since it was rather traditional to customers in the market (Katz, 2016).

Figure 1.1. The original Tropfenwagen designed by E. Rumpler

In the 60s, automotive engineers started to consider the remarkable increase in sound levels emitted by cars at high speed. These problems were understood as the increment of the sound level intensity for the adjacent land at a non-linear rate. Later, road engineers started to design highways by considering aerodynamic drag generated higher sound levels at higher speeds, and car producers began to consider this fact in their automobile designs. Also in the same years, race car engineers realized that an increment in downforce provided a great advantage in races, and they achieved success in races with curvy laps by creating a significant amount of downforce from the inverted airplane airfoil. Hence, general trends of lateral acceleration over by years for various vehicle applications depict the importance of aerodynamic lift force (Figure 1.2) (Katz, 1995).

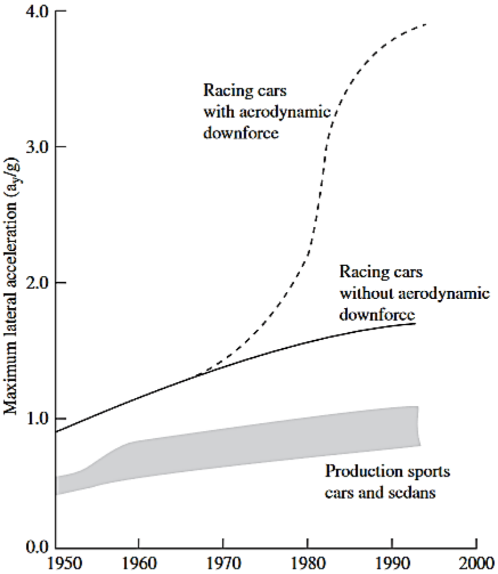

Figure 1.2. General trends of lateral acceleration over by years for various vehicle applications

However, until the oil crisis in the 1980s, great progress could not be made in reducing aerodynamic drag due to reasons such as the lack of development in sheet metal processing technologies and relatively reasonable oil prices (except race cars and exceptional concept vehicles). Moreover, the demands of customers in the automotive market for larger, wider, and more powerful vehicles have also led to this situation. After the great oil crisis in the 1980s, automobile designers began to dust up concerns about the aerodynamic drag on vehicle efficiency. Hence, general trends in automobile shapes (Figure 1.3) have shown that great developments were conducted in automotive aerodynamics. From the 1980s until today, automobiles made a rapid transition to production with streamlined forms rather than blunt shapes (Katz, 2016).

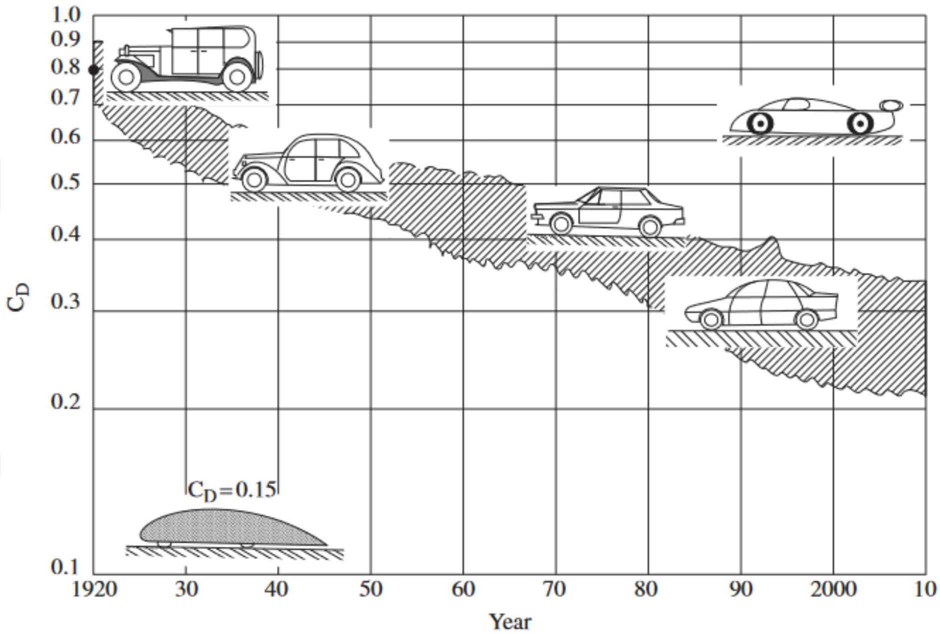

Figure 1.3. General trends of automobile shapes in the automotive industry

1.2. Aerodynamic Forces

A moving ground vehicle exposes three main aerodynamic forces: drag force which is reversed to the moving direction, lift is normal to the ground, and side forces. However, side forces are negligible in almost all cases except air flow coming with a yaw angle. Consequently, two main forces become prominent: drag and lift. The drag force has importance in the sense of energy/fuel consumption and less drag force means increased efficiency since it is resisting force to the moving vehicle. On the other hand, lift force must be assessed at different points. First, it must be lower otherwise excessive lift may cause a rollover, out-of-contact with the ground, and accidents. Nevertheless, too much lift may lead to a significant increase in rolling resistance, thus higher energy consumption and wheel wear. Aerodynamic forces on the vehicle are illustrated in Figure 1.4.

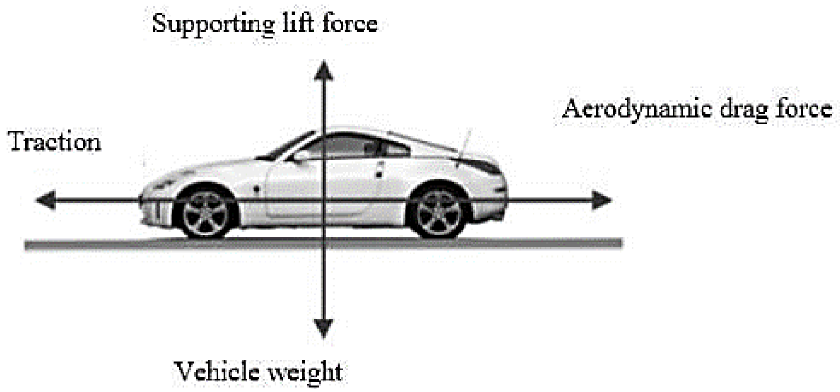

Figure 1.4. Main forces affected on a vehicle body.

The forces exerted on the ground vehicle must overcome increase with vehicle speed, and tire rolling resistance and drivetrain friction forces are shown in Figure 1.5, along with the total resisting force to the motion. It can be seen that aerodynamic drag force increases with the vehicle speed notably. Considering speed limits are increasing rapidly for both vehicles and in road legislation in the 21st century, it can be pretended that aerodynamic drag force should be controlled carefully.

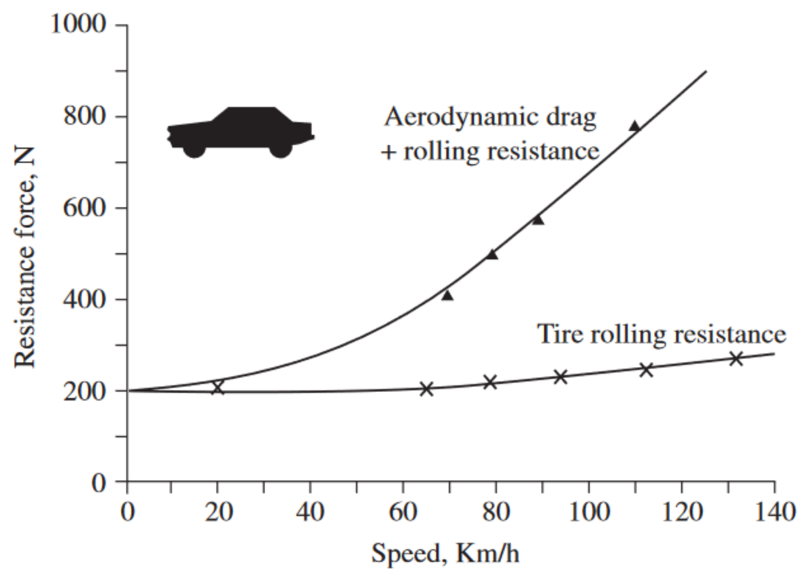

Figure 1.5. Change in aerodynamic drag force and tire Rolling resistance vs. vehicle speed.

A careful assessment of the curves in this graph illustrates that the drag force increases with the square of the vehicle speed while the other components of force sources vary only slightly. Hence, aerodynamicists focus on a non-dimensional coefficient which is called the drag coefficient (C_D). C_D determines the sleekness of a body in the air (for a car). The main advantage of this quantification is that scaling and changing the size is rather practical. Therefore, the aerodynamic performance of a vehicle can be easily determined and compared among similar vehicles. The definition of the drag coefficient is:

$$C_D = \frac{F_D}{0.5\rho U^2 A} \tag{1}$$

where F_D is the aerodynamic drag force, ρ is the density (air in vehicle aerodynamics), U is vehicle speed, and A is the characteristic area. Although there are different approaches for the characteristic area such as equivalent area, the most common adoption is vehicle frontal area (A_F) for automotive aerodynamics. It should be noted here that the drag force is directly proportional to the square of the speed. This means that aerodynamic drag becomes even more critical at high vehicle speeds. At this point, considering that the density term in the formula will change with the environmental condition, two important parameters will determine the drag force: C_D and A_F. For this reason, the use of the C_DA_F term can be seen in many cases. In other words, it can be thought that it would be more accurate to define the "most aerodynamic vehicle" with at least " C_DA_F ". Reducing A_F at this point is impossible due to design constraints. However, there are many different research and development efforts to reduce C_D. The most common is the more streamlined design. In addition, different active and passive control methods are available to reduce this coefficient. To numerically evaluate the effect of aerodynamic drag on fuel or energy efficiency, it is necessary to develop the above equation. In this case, aerodynamic power consumption comes into play:

$$P_D = F_D \times U \tag{2}$$

$$P_D = 0.5 C_D \rho A \times U^3 \tag{3}$$

Where P_D is aerodynamic drag power consumption. It can be said from Equation (3) that aerodynamic drag is quite important for the efficiency of the vehicle (especially at higher speeds) since drag power increases with the cube of the vehicle speed. Numerically, car manufacturers can produce mass-production vehicles with around C_D=0.2-0.3. Ten years ago, it was rare for a car with C_D=0.2 and it was most probably a concept or luxury car. However, factors such as the increasing efficiency race and environmental pollution concerns forced vehicle manufacturers to produce more aerodynamic vehicles than they had previously produced.

The second prominent force is the lift coefficient for ground vehicles can be calculated from the equation below:

$$C_L = \frac{F_L}{0.5\rho U^2 A_F} \tag{4}$$

where F_L is the aerodynamic lift force, ρ is the air density, U is vehicle speed, and A_F is the frontal area. C_L is the other critical aerodynamic performance parameter since it determines vehicle stability, handling, traction, safety, tire condition, and cornering performance of the vehicle. It is expected that the lift coefficient should not be excessively high or low. If it is too much safety problems may be occurred while too low cause excessive tire wear and rolling resistance. In general, aerodynamicists frequently use the expression “downforce” which means reversed (negative lift force) instead of lift force. Because engineers are faced with the fact that in many applications such as racing vehicles, much more downforce is required considering significant lateral forces in a race (Figure 1.6). To attain greater downforce, engineers utilize flow control methodologies such as spoilers and underbody diffusers.

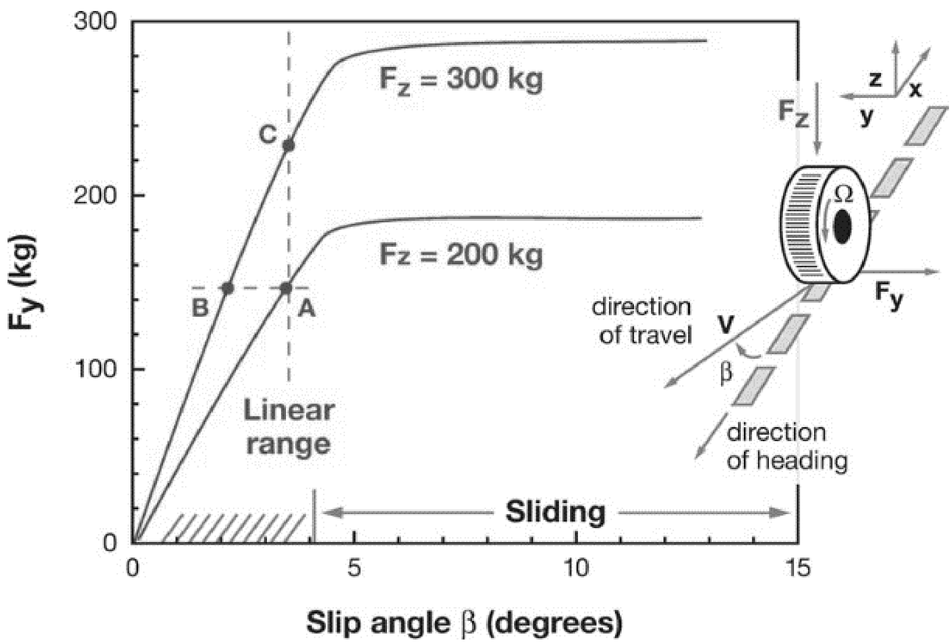

Figure 1.6. Slip angle vs. lateral force on the wheel.

1.3. General recent trends in Aerodynamics

With the overcoming of the 0.3 drag coefficient barrier, it does not seem very possible to achieve a lower drag coefficient in cars with internal combustion engines, except for exceptionally successful models. Because designs that require low cost and a fast design process have led to background concerns about improving aerodynamics in automobile designers. Even in these vehicles with good designs, more efficient engines and more technological equipment are at the forefront, the fuel savings achieved because of the concessions made in the design to achieve a lower drag coefficient have gradually decreased. Since the C_D of these vehicles is quite low 0.3-0.25 for hatchbacks and 0.2-0.25 for sedans. Moreover, drag sources such as wheelhouses and engine intake flow limits further reduction. To demonstrate the significance of drag force reduction for ICE vehicles numerically, consider a vehicle with C_D=0.3, A_F=2.25, traveling at 120 km/h, and having an ICE engine with 100 kW. A 10% reduction in drag force for this vehicle means %1.53 fuel efficiency improvements and for such a small improvement in efficiency, it's questionable whether major design changes are worth it. Moreover, it should also be noted that this efficiency improvement would be lower if the vehicle has a lower drag coefficient.

It is known that people and goods transportation was being provided by utilization of fossil fuels such as gasoline, diesel, compressed natural gas, liquefied petroleum gas, etc. until recently. Even though the diesel market share was very big among these EU nations, in the short term, diesel engine has lost their share in the market rapidly. Especially, considering the emission-cheating scandals in 2015, the development of alternative-fueled vehicles has been more and more essential for the future of the automotive industry. From this point of view, it can be said that gasoline engine has been developed more with turbo and supercharging, improved fuel-injection systems, and engine downsizing to find a remedy for powering vehicles in the mid-term. These innovative engine technologies have been adopted by almost all vehicle manufacturers and have begun to become standard for gasoline engines. On the other hand, with the increasing sales trend of electric vehicles, the rules in automobile design and vehicle aerodynamics are changing more than ever before. There are several reasons for this situation. First, electric vehicles do not require air intake for the engine as in internal combustion vehicles. This naturally results in a significant reduction in drag and requires a re-examination of the changing airflow around the vehicle. Secondly, the fact that electric vehicles have very heavy batteries changes the vehicle dynamics in many ways. Since the batteries are placed on the floor of the vehicle in electric vehicles, the center of gravity of the vehicle is considerably closer to the ground and the seating positions inside the vehicle are positioned a little higher. With the effect of the increasing SUV market, electric vehicle manufacturers have started to produce more SUV vehicle types. At this point, although the hatchback body type comes to the fore, fastback-designed SUV models, which are more advantageous in terms of aerodynamics, are now being produced more frequently. Returning to heavy batteries, if the weight brought by the vehicle batteries does not become less than the weight of the different equipment in the internal combustion vehicles, it seems that there is no need to worry too much about the downforce. It can be seen from Figure 1.7 and Figure 1.8 that an electric vehicle weighing 2000 kg has more downforce than an internal combustion vehicle weighing 1200 kg even in the worst case. Besides, the additional weight brought by the batteries also significantly increases the rolling resistance. That's why tire manufacturers today special tires with low rolling resistance specifically for electric vehicles, which causes extra costs. The additional weight brought by the batteries also significantly increases the rolling resistance. That's why tire manufacturers today produce tires with low rolling resistance, which causes extra costs, specifically for electric vehicles. Considering these situations, increasing the lift coefficient of electric vehicles (until the battery weight is significantly reduced) can give positive results in many ways to increase efficiency, contrary to the popular opinion.

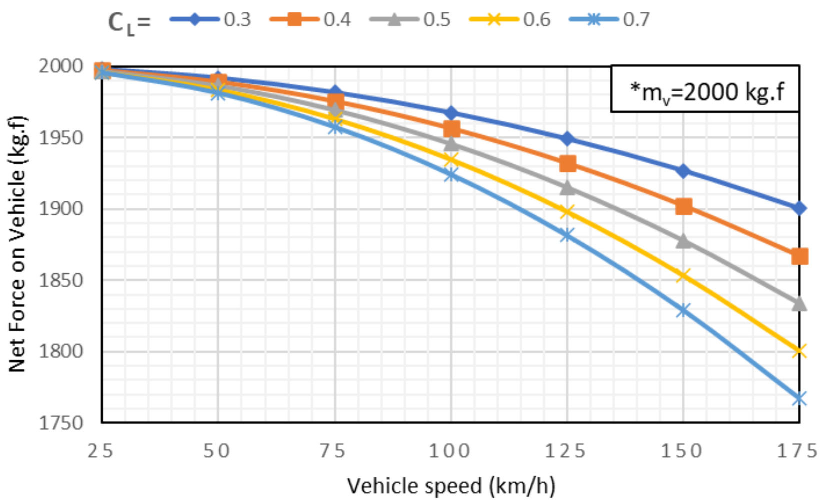

Figure 1.7. Net normal force exerted on an ICE vehicle with 1200 kg mass.

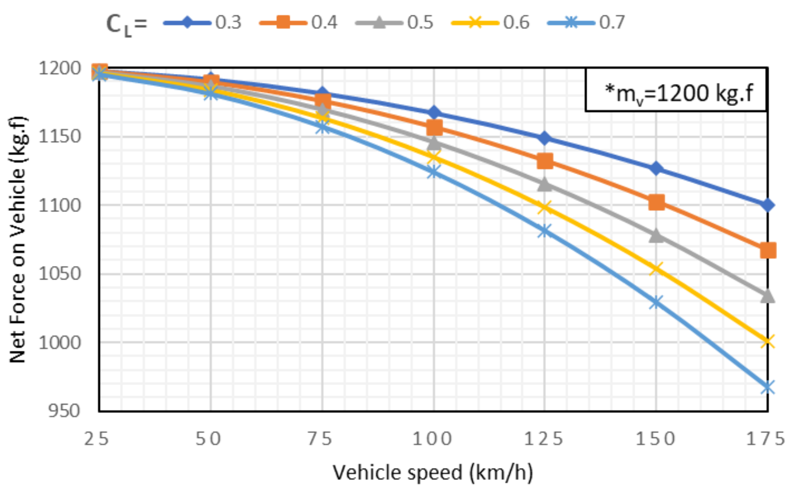

Figure 1.8. Net normal force exerted on an EV with 2000 kg mass.

On the other hand, with the driving range that has not yet reached the desired levels in electric vehicles, there is serious competition in producing a more efficient product in electric vehicles. To increase efficiency, it is very critical to improve the battery capacity/weight ratio, the battery management systems, the efficiencies of electric motors as well as vehicle aerodynamics. Considering EVs' electric motor efficiencies reduce rapidly at high speed and the drag power required increases in direct proportion to the cube of vehicle speed, aerodynamics plays an important role in designing EVs. To illustrate the effect of change in C_D on battery consumption due to aerodynamic drag at various speeds, Figure 1.9 is represented. It can be seen from the graph that, the reduction of drag coefficient has a remarkable effect on driving mileage considering recent battery capacities which are around 90 kWh at most for a mid-class price/performance car.

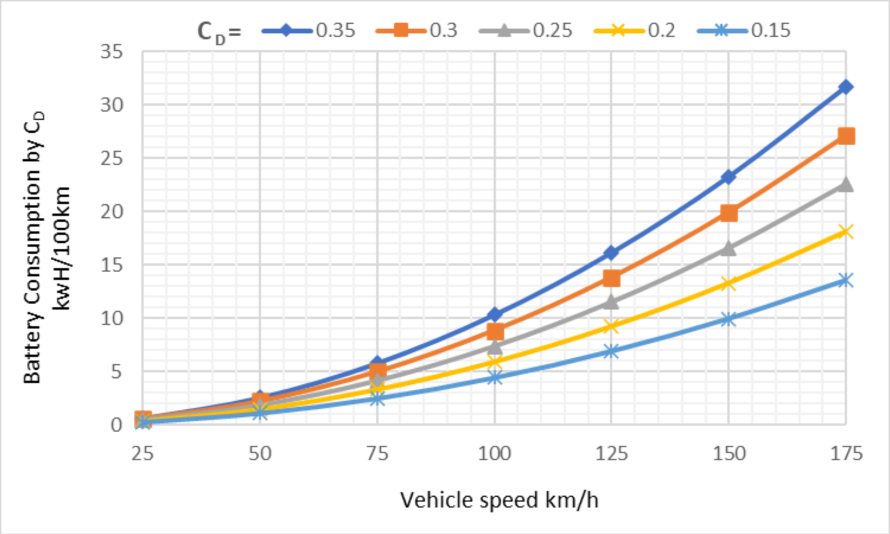

Figure 1.9. Battery consumption due to aerodynamic drag at various speeds with different vehicles

Another critical change in vehicle automotive when it comes to EVs, is regenerative braking systems. These systems convert the kinetic energy of the vehicle into electrical energy by directing it to batteries when decelerating the vehicle. Thus, it prevents wasting energy instead of conventional brakes converting kinetic energy into wasting thermal energy. Briefly, in the near future, conventional brakes may become history or at least lose their significance and their usage frequency of them become less. It is known that conventional brakes need cooling by air into the wheelhouses which causes substantial aerodynamic drag. Considering regenerative brake systems utilization is becoming the norm for EVs, less brake cooling would be required, and less aerodynamic drag can be attained by deflecting the airflow from wheelhouses to the around of the car.

1.4. Generic Vehicle Models

In automotive aerodynamics studies, wind tunnels (usually used force measurements) and water tunnels (usually flow visualization i.e., PIV) are used as experimental methods, and computational fluid dynamics methods are used numerically. In experimental methods, using vehicle models with a one-to-one scale is a very laborious and expensive method. Because, especially in design improvement processes (optimization), it may be necessary to produce many prototypes considering the cycle of design: produce, test, and revise the design. It is not difficult to predict that this would be very expensive, time-consuming, and inconvenient. For the CFD methodologies, all optimization procedures can be performed on computers, and this reduces the amount of cost and time noticeably what many automobile manufacturers exactly do. By doing so, the design is improved step-by-step, and only the final design must be tested and validated experimentally. Nevertheless, vehicle CAD files are difficult to access (know-how concerns) for those interested in research in the field of vehicle aerodynamics, other than the designers of vehicle manufacturers. Even if these models are available, it is difficult to create a common literature because the designs of vehicle models are frequently updated and there are many different vehicle models. On the other hand, creating a common literature on automotive aerodynamics is another important point so that researchers can share, collaborate, validate, and compare their data. To do this, generic vehicle models are great opportunities for researchers. Generic car models have generally simpler shapes, open-CAD files, and open-source data.

For this purpose, in the research and improvement investigations of vehicle aerodynamics performed for many years, the Ahmed body, which has dimensions similar to a ground vehicle, has been the subject of numerous research and most commonly studied generic body. According to the knowledge of the author of this study, the idea of creating a relatively simpler vehicle model arose with the experimental work done by Morel in 1978 [11]. In 1984, Ahmed et. al (Ahmed et al., 1984) introduced a model which is roughly similar in shape to the model put forward by Morel. Yet, with its long and slender form, their model began to reflect the proportions of the size of a typical family car in those years. This model is recognized as the “Ahmed body” in the aerodynamics literature although a very similar model has been presented in the literature by Morel before.

Since the study of Ahmed et. al, various generic ground vehicles have been created, too (almost all of them can be seen in (Le Good and Garry, 2004)). Because of the simple shape of these generic models, they have been studied in numerous investigations to elucidate flow characteristics and improve the aerodynamic performances of these models. Additionally, their being open source to literature led to the adoption of generic models widespread. Researchers have been able to share and verify their works utilizing these models. For instance, because of sharing experimental data with the ERCOFTAC database, it is possible to verify not only aerodynamic force coefficients but also the flow profiles of Ahmed body (“ERCOFTAC - Home”, y.y.).

1.5. Introduction of the DrivAer

Nonetheless, these blunt generic models are too abstract and far from reflecting the shapes of streamlined passenger vehicles these days. Application of flow control strategies and methods which were tested on generic models directly to the production cars may be rather optimistic and not feasible. On the other hand, despite there being some rare studies, mass-production vehicles are not open-source and brands are generally distant to share CAD data of their models due to concerns about privacy policies of their know-how. Moreover, these rare studies are far from creating widespread literature. At this point, BMW and AUDI AG in cooperation with the Technical University of Munich presented a new realistic and representative generic car model, namely DrivAer to close this gap in 2011 (Heft et al., 2012a). The first findings in the preliminary studies such as (Fotiadis et al., 2015; Heft et al., 2012b; Mack et al., 2012; Theissen et al., 2011; Wojciak et al., 2011) have shown that DrivAer models are more representative and have realistic flow properties similar to production cars. With the introduction of DrivAer, automotive aerodynamic literature got a realistic, relatively simple enough that researchers can focus on, an open-source model.

DrivAer ground vehicle model has various configurations such as estateback, notchback, and fastback in the sense of rear-end design; wheelless, smooth wheeled, and detailed wheeled (with rims) in the sense of wheel inclusion; smooth and detailed underbody designs; mirrored and without mirrors: open-grilled and closed grilled in the sense of air induction of engine compartment. These interchangeable parameters allow to researchers choose the desired configuration according to their focal points, demands, and facilities.

1.6. Flow Control Methods

Improving the aerodynamic performance of a vehicle is carried out by the way of flow control techniques. For example, active control strategies which necessitate energy addition to actuate the system are one group of the way of controlling the flow. Nevertheless, their energy demand makes active flow control methods disadvantaged over passive flow control which is the other main flow control strategy. The main strategy of passive flow control techniques lies behind geometry modifications of the body. Add-ons such as diffusers, spoilers, vortex generators, and fairings are the main passive flow control methods, of automotive aerodynamics to improve aero performance.

Passive flow control methods are advantageous over the active flow control methods in that they do not require extra energy from the outside. However, passive methods do not react to flow changes such as flow separation, force requirements in various conditions, and air-flow speed except for flexible add-on components. Their efficiencies are questionable and may decline for variable-state applications.

1.7. Deflectors

Since the introduction of the DrivAer model, whether active or passive, various flow control strategies have been started to test for these realistic bodies. Dimpling (Ballerstein and Horst, 2023) vortex generators (D. Wieser et al., 2015), tailpipe positioning (Renan Francisco Soares and De Souza, 2015a), and fluidic oscillators (Dirk Wieser et al., 2015) are some of these active and passive flow control methods implemented on realistic car models.

A deflector, as the name implies, is a flow control method that tries to improve aerodynamic properties by directing the airflow from one direction to another desired direction. They can be mounted in different regions of a vehicle such as wheel fronts, windows, rear ends, mirrors, etc. Deflectors which are the focal point of this paper have been one of the most frequently studied flow control strategies.

1.8. Adjoint and Gradient-Free Optimization

The adjoint optimization method has been considered the method for gradient-based optimization in CFD for a long time. The adjoint optimization tool is independent of the computational cost from the design variables number and it makes it efficient for problems with large design spaces. Although this method is a standard tool for aeronautical industries since the 70s, its consideration by the automotive industry took part in inlet ducted flows for 20 years. Then, external aerodynamicists considered utilizing the adjoint method for shape optimization of automobiles to improve aerodynamic performance.

Adjoint-based optimization is a prominent and efficient technique for works with large numbers of design variables in CFD. This technique is based on sensitivity computation i.e. derivative of the objective function w.r.t. the design variables (Othmer, 2014). The CFD simulation is thereby independent of the number of design variables and just involves one solution of the adjoint matrices of the governing equation, i.e., incompressible, RANS equations for this paper.

Whether adjoint solutions are implemented to a surface mesh or a volume mesh of the body to be optimized, information for the term ‘sensitivity maps’, can be generated. These sensitivity maps give hints about where surface mesh should move inward or outward to attain desired design variables. By using the solution data of the adjoint solver together with the plug-in of the mesh morphing modules, the optimal design can be achieved with a series of design iterations, independent of the design parameters. Nonetheless, it has been reported that there are some issues such as negative cell volume when using mesh morphing on complex geometries with a large number of meshes in some studies (Munoz-Paniagua et al., 2015; Tzanakis, 2014; Zaya, 2013). In addition, it requires a lot of design iterations if starting optimization procedures of the flow control method with an adjoint solver from the base model. This means a lot of computational costs as an adjoint solution will be done alongside a flow solution for a design iteration cycle.

On the other hand, gradient-free optimizations can be considered challenging because the design parameters and operating conditions can be very large. This means many prototypes or simulations, whether experimental or numerical, which can result in a very laborious and time-consuming process. It may be thought that these difficulties can be overcome more easily when it comes to numerical studies, however, it is known that even a simulation run with millions of meshes can take hours or even days to obtain accurate results. Considering this situation, limiting it to the design of the experiments with parametric optimization can provide to obtain the optimum result somewhat faster. Nevertheless, because of entering the design data through the user with parametric optimization, output results may be still far from the global optimum point. To overcome this, different gradient-based techniques are available. With these techniques, the global optimum can be approached and even reached.

2. PRELIMINARY WORK

2.1. Reference Geometries

Within the last decades, there have been many developments in automotive aerodynamics literature due to strict emission legislation and increasing energy demand.

When searching automotive aerodynamics literature, it can be seen that various vehicle models have been used in both computational and experimental investigations. According to (Le Good and Garry, 2004), these models can be divided into these categories: simple bodies (Ahmed body, Rover Bluff body model, etc.), basic car shapes (MIRA reference car, SAE reference car, etc.), and production cars. Although they can be used multi-purpose, generally simple bodies are used mainly for research, basic car shapes are used for calibration and correlation for experimental setup and research, and production cars are used with both prototype and small-scale model versions for specific study and correlation efforts.

In this sense, in the research and improvement studies of vehicle aerodynamics conducted for many years, the Ahmed body, which has dimensions similar to a ground vehicle, has been the subject of numerous research. According to the information of the author of this article, the idea of creating a relatively simpler vehicle model arose with the experimental work done by Morel in 1978 (Morel, 1978). In the relevant study, the forces generated on the vehicle were examined and as a result, it was stated that the aerodynamic forces of the body highly depend on the real slant angle. It was also revealed that the model has three different flow regimes according to the value of the rear slant angle. However, the size ratios of this model are far from reflecting the size ratios of passenger vehicles of its day (Le Good and Garry, 2004). Moreover, the trailing wake region is not completely independent of the frontal body of this model.

In 1984, Ahmed et. al (Ahmed et al., 1984) created a model which is roughly similar in shape to the model put forward by Morel. However, with its long and slender form, their model began to reflect the proportions of the size of a typical family car (Figure 2.1). Besides, front and rear flow became independent of their generic model. This model is recognized as the “Ahmed body” in the aerodynamics literature although a very similar related model has been presented in the literature by Morel before.

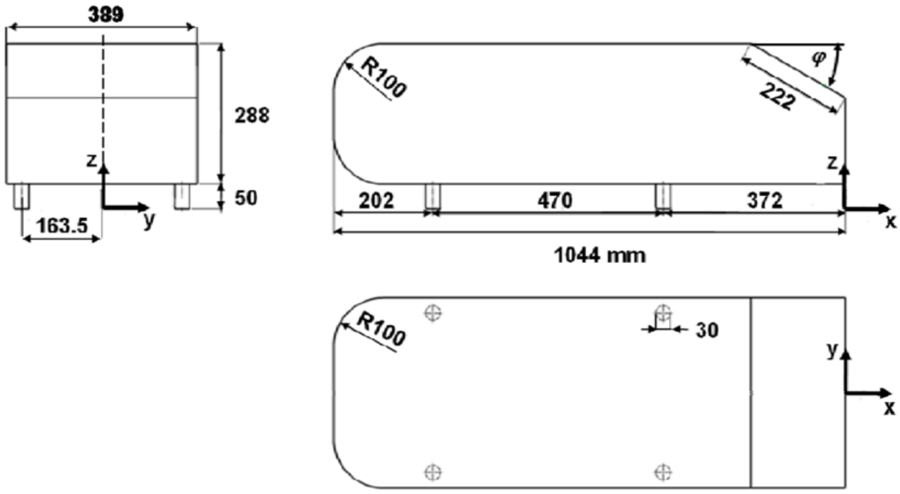

Figure 2.1. Dimensions of generic Ahmed body

In their study, it was stated that the drag force generated on the vehicle is largely caused by the rear part of the body. In addition, it has been revealed that this drag force is caused by pressure drag up to about 85% depending on the rear slant angle. In his study, Ahmed reiterated that, in parallel with Morel's findings, the angle of the slanted (φ) has a great influence on the change in the drag force, and three different flow regimes occur depending on this angle. In regime I, when φ<12.5°, the flow is fully attached to the rear slanted surface, and a longitudinal vortex pair is formed in the near-back region. In this region, C_D=0.25 and is almost independent of the rear slant angle. In Regime II, longitudinally elongated vortices in the wake region are stronger and have a 3-dimensional form in the range of 12.5°<φ<30°. However, as the back slope angle approaches 30°, the flow detaches from the rear slanted surface, forming D-shaped separation bubbles, and this detachment causes a low-pressure zone on the rear slanted surface and severely increases the vortices in the wake region. For this reason, the drag coefficient reaches a peak value at this angle. In cases where the rear slant angle is greater than 30°, the flow has completely separated from the rear slanted surface and there is no tendency to hold on to the rear surface of the body again. For this reason, the C_D value decreases significantly compared to the φ=30°, reaches equilibrium, and becomes almost independent from the rear slant angle at 35° (Huminic and Huminic, 2010).

The Ahmed body is probably the most investigated model that has improved by extending its body features later. For instance, (Fabijanic, 1996) included wheels and wheelhouses in the model, and in his experimental work, it was shown that wheel inclusion has a great contribution to the aerodynamic drag.

As for the basic car shapes category, the Rover model was presented by Windsor and Howell in the late 1980s to guide fundamental research of shape effects on aerodynamics. This reference model was devised by utilizing the proportions and sizes of medium cars of the era. The design has a chiseled front and inter-changeable back-ends allowing researchers to vary back slant angle with increments of 5° from 0° to 40°. Moreover, back slant angles of 27.5° and 32.5° were also added for extra resolution around the critical back slant angle. One of the important design characteristics of the model which is similar to the Morel and Ahmed models is that the length of the slanted face at the rear end is the same for all the rear ends to keep drag-induced effects consistent (Howell and Hickman, 1997).

(Aronson et al., 2000) were tried to evaluate the aerodynamic drag contribution from the front and rear wheels by performing both experimental and numerical studies using their new ASMO model. The model that could be downloaded from the internet has featured a square-back rear end, smooth surfaces, boat tailing, an underbody diffuser, and a more streamlined shape. The model has a such simple and clean geometry that it can easily mesh without requiring extra computational resources.

MIRA reference car is another one of the most well-known simplified car shapes that evolved from the correlation works conducted by European and North American Wind Tunnel operators (Carr, 1982). In their works, the model was in various configurations, and no-standard geometry could be consisted. (Carr, 1982) a designed a new reference vehicle – the MIRA Reference Car, derived from the proportions of “family-sized” production cars of the time by the means of collaboration and correlation investigations between researchers. The model is designed using production-based vehicles such as FIAT 124, a FIAT Ritmo, and a VW 1600. In his model, the vehicle body has interchangeable rear-ends with three configurations that stand for three main automobile body types: estateback, fastback, and notchback. This study also seems to have inspired the DrivAer project, which will be mentioned later. These models have distinctly different wake structures as reported by (Hucho, 2000). While three models are available representing common production automobile shapes, the MIRA model design range is also extended with a fourth configuration, a pick-up shape, too.

Although, (Le Good and Garry, 2004) categorize reference models into three classes, a new category can be identified according to the author of this work. The new category called “realistic models” can be encountered since the early 2010s evolved based on the need for more representative realistic automobile models. The above-mentioned simple and basic car shape models are too abstract and far from reflecting the shapes of streamlined passenger vehicles in this era. Implementation of flow control methods that were tested on simple models directly to the manufactured automobiles may be rather optimistic and not feasible. On the other hand, series-production cars are not available open-source and brands are generally distant to share CAD data of their models due to concerns about privacy policies of their know-how. Even if vehicle manufacturers share their models, studies on these models are quite rare and therefore it is not possible to create widespread and collaborative literature on them. From the point of this scientific gap, BMW and AUDI AG in cooperation with the Technical University of Munich presented a new realistic and representative generic car model, namely DrivAer to close this gap in 2011 (Heft et al., 2012a).

The first findings in the preliminary studies such as (Fotiadis et al., 2015; Heft et al., 2012b; Mack et al., 2012; Theissen et al., 2011; Wojciak et al., 2011) have shown that DrivAer models are more representative and have realistic flow properties similar to production cars., automotive aerodynamic literature is enriched with realistic models since the introduction of DrivAer which is relatively simple enough that researchers can focus on, an open-source model.

DrivAer ground vehicle model has various configurations such as estateback, notchback, and fastback in the sense of rear-end design; wheelless, smooth wheeled, and detailed wheeled (with rims) in the sense of wheel inclusion; smooth and detailed underbody designs; mirrored and without mirrors. These interchangeable parameters allow to researchers choose based on their work, demands, and facilities. Moreover, the model also was configured with an open-grille body type allowing the investigation of airflow through the engine compartment (Wittmeier and Kuthada, 2015).

Following the introduction of the realistic DrivAer model, two new realistic models were also introduced to the automotive aerodynamic literature. First, (Chenyi Zhang et al., 2019) represented a new realistic SUV model called AeroSUV. They stated that the number and share of SUVs in the market (especially in Europe) have increased remarkably within the last decades. SUVs characterize by a large cross-sectional area, an increased ground clearance, and larger wheel size. The DrivAer model was not capable of representing SUVs, hence the need for a new generic vehicle was met by a new open-access model, the so-called AeroSUV. The AeroSUV structure is similar to DrivAer except for a typical mid-class SUV's characteristic feature.

The second new project following the DrivAer models is GTU (Woodiga et al., 2020). It is a realistic generic pickup and SUV model to overcome additional aerodynamic challenges due to the complex wake structures of pickup trucks and SUVs. In the related work, the first experimental and numerical findings of this project were shared.

2.2. Flow Control Investigations

Improving the aerodynamic performance of a vehicle is conducted by flow control techniques. There are two salient flow control methodologies in automotive aerodynamics literature: active and passive flow control techniques. Active control strategies need energy addition to actuate the system and their energy demand makes active flow control methods disadvantaged over passive flow control which is the other main flow control strategy. On the other hand, passive flow control methods do not require external energy and they are based on geometric shape modifications.

Deflectors which are the main topic of this study have been considered as both passive and active flow control strategies in the automotive aerodynamic literature. An interesting research on the effect of tailpipe position on the aerodynamic performance of a vehicle was carried out by using a realistic DrivAer model (Renan Francisco Soares and De Souza, 2015a) to deflect wake flow at the rear end. Researchers of this paper used an empirical model to estimate exhaust mass flow rate and then tested a batch of various exhaust outlet positions at the rear part of a DrivAer fastback model. Although the coefficient of drag of the model was reduced slightly, (0.7% variance compared with the baseline model) this reduction can be more meaningful from a motorsport perspective according to the authors of this work.

(Cho et al., 2018) implemented horizontal and vertical plates as a deflector element to weaken the downwash of the upper flow and prevent the formation of a longitudinal vortex pair at the rear of the DrivAer notchback model. As a result, they obtained a drag reduction of 5.1% with an optimum horizontal plate. For the vertical plate case, a 3.3% reduction of drag was seen by weakening c-pillar vortices.

Another deflector plate investigation was carried out by (Kurec et al., 2022) on the DrivAer estateback model and they utilized these plates as airbrake devices. The result of this study has shown that deflector plates can change aerodynamic forces to decelerate vehicles.

The potential of deflector utilization at different locations of a vehicle was tested by (Nabutola and Boetcher, 2021). In this study, wheel deflectors as passive flow control elements and air-jet wheel deflectors were applied to the notchback DrivAer model and assessed numerically. The result of this study has demonstrated that wheel deflectors decreased the aerodynamic drag source of the wheel while it caused an overall aerodynamic drag increase of 10%. However, with a specified angle, air-jet deflectors could reduce the aerodynamic drag up to 1.5%.

Apart from the realistic DrivAer model applications, passive deflector investigations are more concentrated on simpler generic bodies. (Fourrié et al., 2011) adopted a rear deflector on an Ahmed generic model with a slant angle of 25°. They achieved a drag reduction by 9% and stated that flow control devices should be carefully implemented on such geometries considering all the flow structures that contribute to the model wake.

(Hanfeng et al., 2016a) studied rear deflectors which are fitted on the side and top of the rear end of Ahmed body, experimentally. As a result, they were able to change the flow regime and obtain drag reductions for side and top deflectors by 7.6% and 11.8%, respectively.

(Beaudoin and Aider, 2008) studied the effects of different deflector plates located on all edges of Ahmed body for different air velocities. The most efficient implementations were the two flaps on the side edges of the rear slant (drag reduction of 17.6%) and the flap on the top of the rear slant (drag reduction of 15%).

(Kim et al., 2016) designed a moving deflector by mimicking the movements of a bird's wings to control flow separation at the rear of Ahmed body at different freestream velocities. They achieve a significant aerodynamic drag reduction of up to 19%. It was noted that the drag reduction mechanism of the automatic moving deflector could be attributed to pressure recovery on the slanted surface.

The influences of a deflector on drag force and vortical structure at the rear of an Ahmed model with a 25° slant angle were investigated experimentally by (Hanfeng et al., 2016b). The passive control elements were devised at the leading edge and the side edges of the slanted surface. They achieved substantial drag reduction by 9.3%, 10.7%, and 10.9% for the width of 1%, 2%, and 3% of vehicle length, respectively.

Another interesting deflector application was done by (Lee, 2018). In that study, as an active flow control element, an air-jet deflector is mounted in front of the wheels of the Fabijanic model (wheeled model of Ahmed body). He found out that a drag reduction of 6.4% can be achieved when the jet speed was identical to the vehicle's driving speed. Moreover, he stated that brake cooling performance can be improved by tilting the imping jet direction to the brake caliper.

In literature, there are active deflection investigations, too. In one of them, Baek and Lee tested an active flow deflection method with continuous blowing by using the DrivAer estate model at the end of the roof for vertical deflection and at the C-pillar for lateral deflection (Baek and Lee, 2020). Their result indicates that the drag can be reduced by more than 6% for roof deflection due to increasing rear pressure when the blowing speed equals the vehicle's driving speed. The maximum drag reduction is attained for simultaneous roof and lateral blowing by 7.5%.

(Edwige et al., 2022) performed a numerical flow control method and verified the results with qualitative and quantitate data from Ahmed body. They applied three different active controls with pulsed, suction, and synthetic jets to investigate their effect on the flow topology and drag reduction. The results have shown that the active control method with the synthetic jet generated the best drag reduction without any air supply.

Diffusers are another passive control method and the modified sections expand under the car, hence improving the flow transition from the high-air-stream region (underneath the car) to the ambient atmosphere (Huminic and Huminic, 2010).

The modification is on the underbody in the form of a V shape enabling the venturi effect that is put on Bernoulli’s principle. According to this, airflow speeds up under the narrow until mid-region of the underbody and decelerates in the diffuser section which creates a vacuum underbody section (Jowsey and Passmore, 2010).

A diffuser does not reduce only lift force but also drag force. The diffuser provides space in the back region for the underbody airflow to decelerate which enables momentum transfer to the wake and a substantial pressure recovery at the rear back (Huminic and Huminic, 2012).

Nevertheless, the effectiveness of an underbody diffuser is so sensitive to design parameters and an underbody diffuser may result in drag rise and stall in some cases (Porcar et al., 2021). It has been stated in different studies in the literature that the diffuser angle should not be too much or too little. Accordingly, if the diffuser angle is too low, the pressure recovery potential of the diffuser may remain low (Huminic and Huminic, 2010).

On the other hand, if this angle is too high, there will be flow separations and the stall issue, i.e. increase in drag force, similar to that of airfoils (Guerrero et al., 2022; Jowsey and Passmore, 2010; Soso and Wilson, 2006; Taiming et al., 2020).

(D'Hooge et al., 2012) investigated the aerodynamic efficiency of the Tesla EV sedan car by varying wheel rim designs, numerically. They tested three-wheel configurations; fan concept, profiled spoke concept, and vented disc concept and compared these with the original one. As a result, the vented wheel with a large flat central section and venting around the perimeter provided drag reduction by 25 counts (1 count=0.001).

(Dirk Wieser et al., 2015) performed an active flow control methodology on notchback DrivAer by fluidic oscillators placed at rear-end. They varied the spacing of the actuators, the mass flow rate, and the position of actuation. A maximum reduction in the net drag forces of 3.5% and −3% was obtained for the actuation of fluidic oscillators at the c-pillars or the roof, respectively. Moreover, a drag reduction of up to 6% was attained for a higher momentum input.

(Aktas and Abdallah, 2017) conducted a numerical study to develop an electrical vehicle by using DrivAer realistic generic models. They devised the model with an air curtain, wheelhouse ventilation, spoilers at different locations on the car, and underbody vanes. The final design resulted in a drag reduction by 33-35 counts for the estateback and fastback models which means a C_D value of 0.236 for the estateback and 0.216 for the fastback.

(Mohammadikalakoo et al., 2020) carried out a passive flow control by adding linking tunnels at the rear of the Ahmed body, blowing the flow from the high-pressure zone at the sidewalls to the low-pressure zone of the wake region. They obtained a drag reduction of 5% with optimal configuration of the simulations. They noted that the reduction of the aerodynamic drag was ensured by the movement of a high-pressure flow to the wake zone.

(Pujals et al., 2010) applied small-scaled cylindrical vortex generators to delay flow separation at the rear-back of the Ahmed Body. According to their PIV measurements, remarkable drag reduction was ensured for all sets of wavelengths and streamwise locations by reducing pressure gradients in the turbulent boundary layer.

(Yang et al., 2022) investigated the effects of vortex generators and riblets on the rear slanted surface of the Ahmed body on flow field structures. They reported that these flow control devices had different flow mechanisms and notably changed the flow separation characteristics. The maximum drag reduction of 6.21% was obtained by the usage of a vortex generator on the rear surface. Furthermore, they stated that a further decrease in the aerodynamic drag can be achieved with a suitable combination, numerically an 8.62% drag reduction was measured.

In another vortex generator study, delta-winglet, cylindrical, and trapezoidal vortex passive flow control elements were implemented (Viswanathan, 2021). In this study, vortex generators were located at the end of Ahmed body roof and works were conducted on RANS based CFD solver at different yaw conditions. The maximum reductions were obtained for cylindrical and trapezoidal by 8.5% and 7.7% at smaller vehicle yawing conditions.

(D. Wieser et al., 2015) have performed an experimental study by attaching vortex generators to the roof of a vehicle at variable positions to evaluate their effect on the aerodynamic drag of a realistic DrivAer notchback model. According to the measurements, the maximum pressure coefficient was increased up to 0.2. Qualitative assessments depicted that flow separation could be reduced or completely suppressed. Hence, the lift force was reduced up to 33%. Nevertheless, drag force was found higher between 0.5-4% for all configurations. Thereby, it could be said that the drag force induced by the vortex generators was greater than the effect of the pressure recovery.

Manipulation of the turbulent boundary layer by surface roughness is a passive flow control method in fluid mechanics. The application of surface roughness as a flow control element into automotive aerodynamics has been continuously tested. In this kind of study, (Y. Wang et al., 2017) studied a dimpled non-smooth surface to decrease the aerodynamic drag of the Ahmed body. Moreover, an aerodynamic optimization method based on a Kriging surrogate model was performed further to maximize the drag reduction influence of the dimpled non-smooth surface. As a result, the aerodynamic drag was decreased by 5.20% for the optimal combination of design variables.

(Ballerstein and Horst, 2023) applied the dimple patterns on the surface of the DrivAer notchback model to reduce flow separation and aerodynamic drag force. They reported that all extruded dimple patterns on the rear window of the realistic vehicle model decreased drag and lift forces by up to 1.9% and 19.2%, respectively, compared with the base model of the notchback DrivAer. Besides it was stated that the dimpled surface flow control has shown less potential to reduce lift, however, but provided a notably aerodynamic drag reduction compared with vortex generators.

From the point of the above-mentioned review of automotive literature, it can be said that flow control strategies such as deflectors, surface roughness, diffusers, and add-on parts have great potential to increase efficiency and reduce emissions of automobiles. On the other hand, these conventional flow control strategies have considered and been started to test on more realistic vehicle models rather than old-school ground vehicle models to discover their applicability and feasibility of them on real cars.

2.3. Adjoint Optimization and Gradient Free Optimization Studies

The adjoint optimization method has been considered the method for gradient-based optimization in CFD for a long time. The adjoint optimization tool is independent of the computational cost from the design variables number and it makes it efficient for problems with large design spaces. Although this method is a standard tool for aeronautical industries since the

70s, its utilization for the automotive industry took part in inlet ducted flow for 20 years. Afterward, external aerodynamicists began to use the adjoint method for shape optimization of automobiles to improve aerodynamic performance.

(Othmer, 2014) published his review paper which involves mathematical aspects, specific applications, development processes, and future trends of the adjoint optimization method.

(Othmer et al., 2011) conducted a shape optimization on the rear spoiler area of Volkswagen XL1 by their proposed morphing technique. They achieved both drag and lift reductions by 1.5% and 30%, respectively. Considering the model has a C_D of less than 0.2 which means the car is aerodynamically already nearly perfect this further optimization was promising for the adjoint method.

Another benchmark study was performed by (Hojjat et al., 2014). They applied the mesh morphing partially on the side mirrors and the whole body of the Volkswagen Passat model. As a result, a relatively slight modification in the geometry of the side mirrors reduced the drag by 7% with 16 optimization cycles. Moreover, a 1.6% drag reduction has been attained without any smoothness or mesh regularity issues and within 20 steps.

(Christian Bach Rasmussen and Lasse Mose Lund, 2018) applied adjoint optimization on DIS1 serial-hybrid electric race car. They aimed at attaining a body kit to generate 1200kgf of downforce at 280km/h while maintaining drag, low enough for 280bhp to overcome the same conditions. The initial design was optimized with two parametric design iterations then they applied the discrete adjoint method. Their design objective was the improvement of downforce. The initial design was improved with 173.98kgf of downforce and the required power to overcome the aerodynamic drag force was lowered by 23.13 bhp by parametric optimization. The adjoint optimization further enhanced the downforce with 67.84kgf, while reducing the drag force with a force by 44.07bhp.

(Lång, 2019) investigated challenges and problems that occurred during the adjoint optimization. It was stated that the residual minimization scheme could be beneficial when facing convergency issues during adjoint solutions. It was also suggested that a mesh structure with less count could be used to overcome localized transient behavior if the adjoint solver has trouble converging. Besides, geometry can be cleaned and simplified in some regions to prevent local instabilities.

(He et al., 2018) proposed a discrete adjoint within a constrained shape-design optimization framework based on Open-FOAM. They morphed and optimized the ramp angle and shape at the rear of the generic Ahmed body. The results of the ramp angle matched the optimal value predicted by numerical simulations. They also validated the numerically obtained pressure distributions and wake structures with experimental data. Consequently, it was reported that the optimized geometry ensured a pressure recovery by changing the wake and the flow separation, providing a drag reduction of 9.4%.

(Zaya, 2013) studied capabilities of the adjoint solver of Ansys Fluent throughout the Volvo Cars Aerodynamic development process in collaboration with Volvo Cars, the Chalmers

University of Technology, and Ansys. They reported some convergency and negative mesh cell issues during the adjoint solutions and mesh morphing, respectively.

(Munoz-Paniagua et al., 2015) investigated the application of the adjoint optimization method on a train's nose to reduce aerodynamic drag force. They also evaluated the effectiveness, requirements, limitations, and capabilities of the method. Consequently, they obtained a reduction of a 7.2% of the aerodynamic drag force in 14 simulations.

(Papoutsis-Kiachagias et al., 2019) presented continuous adjoint-enabled, gradient-based optimization tools for multi-point, multi-objective industrial optimization problems. They tested the application of the tool to the shape optimization of a concept car aiming for minimum drag for a longitudinal wind and minimum yaw moment for a 30◦ side wind. The results have shown that a reduction in the drag and yaw moment can be achieved with 60 optimization cycles by 8% and 24%, respectively.

Although there are there are studies on the usage deflector plates for realistic generic vehicle model to control the flow, either they have not been investigated in the sense of variation the deflector angle (Aktas and Abdallah, 2017; Cho et al., 2018) or not implemented realistic generic bodies (Cheng et al., 2018, 2019; Fourrié et al., 2011; Hanfeng et al., 2016a). From this point of view, deflectors as passive flow control elements are tried to optimize to minimize aerodynamic drag force by using different optimization strategies. Considering that estateback, fastback, and notchback configurations of the DrivAer realistic model are chosen. Considering the computational resource and capabilities as well as possible adjoint solver instability and mesh morphing issues, the smooth underbody closed body without wheels, mirrors, and open grille is used for the sufficiency of coarser mesh. The deflector flow control element is tested for both the upper and lower sections at the rear parts of the model. The angle of the upper and lower diffuser is optimized step by step with parametric, Genetic Algorithm based response surface, and adjoint optimization, respectively. This order is not an arbitrary selection since global minimum is tried to be reached faster by parametric optimization without negative cell issues and instabilities of adjoint solutions. Output results are used as design of experiment (DOE) data for response surface optimization. Then, the result of the design obtained after getting closer to the global minimum with the response surface optimization is used as the primal result in the last step, the adjoint optimization. By following this optimization framework, global minimum is attempted to obtained with less design point, avoiding cell negative issue, less computational cost. The cost-effective RANS simulations are performed with Menter's k-ω SST turbulence model by using CFD Solver of Ansys Fluent. More details about the flow control method, meshing strategies, numerical setup, optimization procedures used in this investigation can be found in Material and Method section. Results of the study are evaluated from both quantitative and qualitative aspects to find out what underlies effectiveness in flow control of the upper and lower deflectors and how flow topology is affected in different regions of the DrivAer models. These detailed results are presented in the Result and Discussion part. Finally, general outcomes from this work can be seen in Conclusions.

3. MATERIAL AND METHODS

3.1. Simulation Procedures

In numerical studies, rigorous, and systematic CFD processes should be executed to ensure highly reliable solutions. Otherwise, the solutions of the simulations would not be consistent and meaningless. To do this, error sources should be minimized CFD. The definition of error implies that the deficiency is identifiable upon examination. There are two main error sources in the numerical solutions: unacknowledged and acknowledged errors.

Acknowledged errors (examples include round-off errors and discretization errors) have procedures for identifying them and possibly removing them. Otherwise, they can remain in the code with their error estimated and listed. As for, unacknowledged errors (examples include computer programming errors or usage errors) have no set procedures for finding them and may continue within the code or simulation.

One can differentiate between local and global errors. Local errors refer to errors at a grid point or cell, whereas global errors refer to errors over the entire flow domain. We are interested here in the global error of the solution that accounts for the local error at each grid point but is more than just the sum of the local errors. Local errors are transported, advected, and diffused throughout the grid.

The definition of error presented here is different than that an experimentalist may use, which is "the difference between the measured value and the exact value". Experimentalists usually define uncertainty as "the estimate of error". These definitions are inadequate for computational simulations because the exact value is typically not known. Further, these definitions link error with uncertainty. The definitions provided in the above paragraphs are more definite because they differentiate error and uncertainty according to what is known.

Typical acknowledged error sources are physical approximation error, physical modeling error, geometry modeling error, computer round-off error, iterative convergence error, discretization error, spatial discretization error, and temporal discretization error while unacknowledged errors are computer programming error and user error.

3.1.1. Physical Approximation Error

Physical modeling errors are those due to uncertainty in the formulation of the model and deliberate simplifications of the model. These errors deal with the continuum model only. Converting the model to a discrete form for the code is discussed as part of discretization errors. Errors in the modeling of the fluids or solids problem are concerned with the choice of the governing equations which are solved and models for the fluid or solid properties. Further, the issue of providing a well-posed problem can contribute to modeling errors. Often modeling is required for turbulence quantities, transition, and boundary conditions (bleed, time-varying flow, surface roughness). Mehta lists sources of uncertainty in physical models as 1) the phenomenon is not thoroughly understood; 2) parameters used in the model are known but with some degree of uncertainty; 3) appropriate models are simplified, thus introducing uncertainty, and 4) an experimental confirmation of the models is not possible or is incomplete. Even when a physical process is known to have a high level of accuracy, a simplified model may be used within the CFD code for the convenience of more efficient computation. Physical modeling errors are examined by performing validation studies that focus on certain models (i.e. inviscid flow, turbulent boundary layers, real-gas flows, etc...).

3.1.2. Computer Round-Off Error

Computer round-off errors develop with the representation of floating-point numbers on the computer and the accuracy at which numbers are stored. With advanced computer resources, numbers are typically stored with 16, 32, or 64 bits. Round-off errors are not considered significant when compared with other errors. If computer round-off errors are suspected of being significant, one test is to run the code at a higher precision or on a computer known to store floating point numbers at higher precision. One can attempt to iterate a coarse grid solution to a residual of machine zero; however, this may not be possible for more complex algorithms.

3.1.3. Iterative Convergence Error

The iterative convergence error exists because the iterative methods used in the simulation must have a stopping point eventually. The error scales to the variation in the solution at the completion of the simulations.

3.1.4. Discretization Errors

Discretization errors are those errors that occur from the representation of the governing flow equations and other physical models as algebraic expressions in a discrete domain of space (finite difference, finite volume, finite element) and time. The discrete spatial domain is known as the grid or mesh. The temporal discreteness is manifested through the time step taken. Discretization error is also known as numerical error. A consistent numerical method will approach the continuum representation of the equations and zero discretization error as the number of grid points increases and the size of the grid spacing tends to zero. As the mesh is refined, the solution should become less sensitive to the grid spacing and approach the continuum solution. This is grid convergence. Such thinking also applies to the time step. The grid convergence study is a useful procedure for determining the level of discretization error existing in a CFD solution. "Ordered" discretization errors are those dependent on the grid size and vanish as the grid size approaches zero. These are the errors that are addressed by a grid convergence study. Further details can be found on the pages entitled Examining Spatial (Grid) Convergence and Examining Temporal Convergence.

The discretization error is of most concern to a CFD code user during an application. Discretization errors are of major concern because they are dependent on the quality of the grid; however, it is often difficult to precisely indicate the relationship between a quality grid and an accurate solution before beginning the simulation. The level of discretization error is dependent on grid quality. The grid should be generated with consideration of such things as resolution, density, aspect ratio, stretching, orthogonality, grid singularities, and zonal boundary interfaces.

The level of discretization error is dependent on the features of the flow as resolved by the grid. Errors may develop due to the representation of discontinuities (shocks, slip surfaces, interfaces, ...) on a grid. Interpolation errors come about at zonal interfaces where the solution of one zone is approximated on the boundary of the other zone.

The truncation error is the difference between the partial differential equation (PDE) and the finite equation. The truncation error is a function of the grid quality and flow gradients. Dispersive error terms cause oscillations in the solution. One fix to this is adding artificial dissipation to decrease the size of the dispersive errors. Dissipation error terms cause a smoothing of gradients. However, a level of dissipation comparable to the actual physical viscosity may contaminate the solution. Boundary layers may thicken. The truncation error terms are those of the expansion which are not used in the discretized equation. If the order of the leading term of the truncation error is of second order, it is known as a numerical viscosity (dimensions of length^2/time), which is the dimensions of kinematic viscosity. A positive viscous term will indicate that errors will be damped whereas a negative viscous term will indicate that errors will grow (unstable).

Included in the discretization error are errors due to not properly converging the solution with respect to the iterations to the steady-state solution or within a time step. This is referred to as iterative convergence.

3.1.5. Computer Programming Errors

Programming errors are "bugs" and mistakes made in programming or writing the code. They are the responsibility of the programmers. These types of errors are discovered by systematically performing verification studies of subprograms of the code and the entire code, reviewing the lines of code, and performing validation studies of the code. The programming errors should be removed from the code prior to release.

3.1.6. Usage Errors

Usage errors are due to the application of the code in a less-than-accurate or improper manner. Usage errors may show up as modeling and discretization errors. The user sets the models, grid, algorithm, and inputs used in a simulation, which then establishes the accuracy of the simulation. There may be blatant errors, such as attempting to compute a known turbulent flow with an assumption of inviscid flow. A converged solution may be obtained; however, the conclusions drawn from the simulation may be incorrect. The errors may not be as evident, such as the proper choice of turbulence model parameters for separated flows with shocks. The potential for usage errors increases with an increased level of options available in a CFD code. Usage errors are minimized through proper training and the accumulation of experience.

The user may intentionally introduce modeling and discretization errors in an attempt to expedite the simulation at the expense of accuracy. This may be proper in the conceptual stage of a design study where more general information is needed at less accuracy. Even in the later stages, there may not be proper computational resources to simulate at the proper grid density. One must understand the level of accuracy accompanying the results. Usage errors should be controllable through proper training and analysis. Usage errors can exist in the CAD, grid generation, and post-processing software, in addition to the CFD code.

In the following sections, efforts to minimize error sources during numerical simulations of this study are explained.

3.2. Pre-processing

A CAD software, SpaceClaim, was used to solidify the model, identify the mesh regions to be cleaned, and determine the flow field and boundary conditions for the solver. In this study, three different DrivAer generic models closed body fastback, notchback, and estateback were used (Figure 3.1). Due to the limited computational sources, these models are selected smooth underbody, without wheels, engine inflow, and mirrors that highly increase required mesh counts significantly.

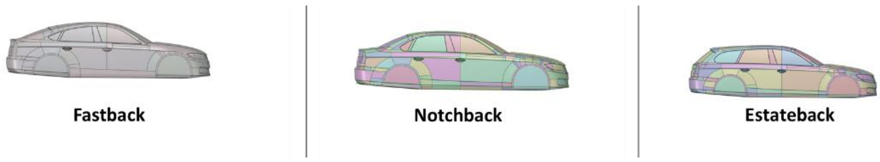

Figure 3.1. DrivAer geometries used in the numerical simulations.

While generating the flow domain, it was ensured that it was large enough by considering similar CFD studies in the previous literature. Thus, it is aimed that the flow velocity profiles are fully developed from the velocity inlet until they reach the object, the wake region behind the object is fully covered, and the blockage effects are kept to a minimum. For this purpose, blockage ratio of the test section is tried to keep (A_F/A_{test}) <%5. Çengel and Cimbala recommended that the blockage ratio be less than 7.5% (Cengel ve Cimbala, 2006). In addition, the side and top walls, which are fixed in experimental methods such as wind and water tunnels, were set as symmetry boundary condition in this CFD study, a method frequently used in the literature. With this method, it can be thought that the blocking effects are eliminated by defining the free slip condition on the top and side walls. In addition, the input velocity was entered as U_∞=45 m/s to satisfy the $Re_L=5.2\times10^6$ condition. Details on the flow domain and the boundary conditions are shared in Figure 3.2 and Table 3.1.

Table 3.1. Properties of flow domain

Flow Domain	Quasi 3-D, steady, turbulent, and incompressible
Length X height X width	14L X 3H X 3W
$\boldsymbol{A_F}$	≅2.3 m^2
$\mathbf{A_F/A_{test}}$ **(Blockage ratio)**	< 5%

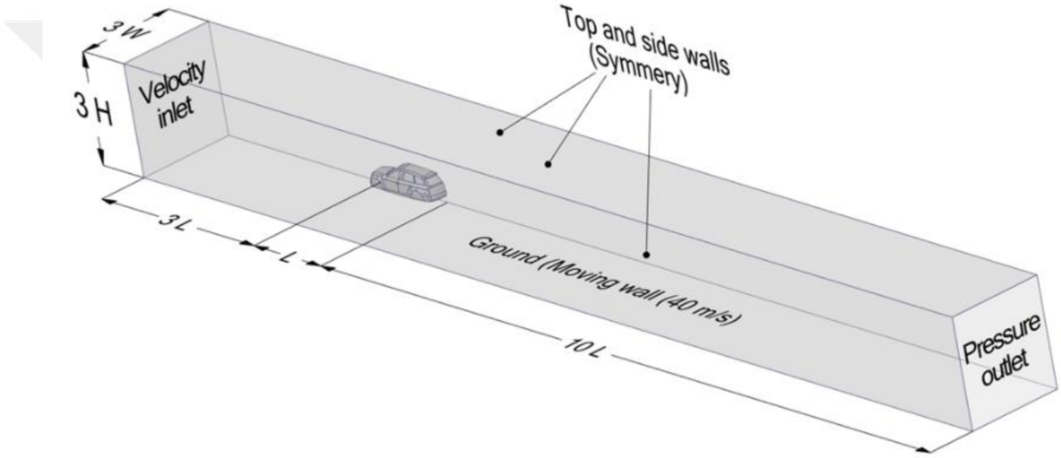

Figure 3.2. 3D view of the computational domain

3.3. Mesh Generation

Meshing, which is one of the most laborious and time-consuming stages in CFD simulations, is challenging for most users. Both the developments in CFD software and the detailed studies on this subject from day to day are guiding in meshing, and even the processes are automated by becoming independent of the user. However, many times CFD users find it difficult to determine the required level of mesh resolution in a CFD simulation. At this point, mesh independence tests are required for a CFD simulation. Mesh independence can generally be defined as the mesh level at which, in a CFD simulation, the difference in an output value of interest (drag coefficient, lift coefficient, flow profile, pressure drop, temperature, etc.) reaches below a certain value as the mesh resolution increases (Saraf et al., 2017). However, it is a matter of discussion here how much the increase in mesh resolution will be, in which regions the flow area will be densified, which output value will be of interest, and how much the change in output values should be.

Researchers follow different methods to ensure mesh resolution in general, specific to vehicle aerodynamics. For a sufficient mesh independence according to SAE, the change in drag coefficient at 50% increase in mesh resolution should be below ∇C_D=0.001 (Huminic and Huminic, 2012). However, there are different applications in the literature. For example, (Cho et al., 2018) increased the mesh resolution by 60%, while the mesh level which the variation is below 3% for C_D was considered mesh-independent. In another CFD study focusing on vehicle aerodynamics, (Read and Viswanathan, 2020) compared the C_D results obtained from different mesh resolutions with the experimental data and accepted the mesh level closest to the experimentally obtained data as independent of the mesh resolution. (Chunhui Zhang et al., 2019), on the other hand, increased the number of mesh counts by 33% and stated that the change in C_D was below 1% and accepted the simulations as independent of the mesh. However, there are studies in which C_L is considered as output data for mesh independence test. However, these studies show that the percentage change in C_L is more than 10%. This is because, in addition to the fact that the absolute values of C_L of the examined generic geometries are very small, they still give high errors in approximating the experimental data in C_L calculations in CFD simulations (Huminic and Huminic, 2017). To prevent this, especially in studies where C_L is considered as output for the mesh independence test, the counts change is considered instead of the percentage change. Accordingly, 1 count = 0.001 for C_L and C_D. Thus, the error caused by considering the percentage change is avoided, and both C_L and C_D results can be evaluated for resolution with mesh independence. For example, (X. Yu et al., 2018) assumed mesh-independent at the mesh level where the variation for C_L and C_D are below 2 counts. On the other hand, it can be seen in the literature that data outputs such as velocity profiles and flow structure in the wake region are used for mesh independence works. (Emmanuel Guilmineau, 2014; Tunay et al., 2016).

In this numerical study, Watertight Geometry Workflow task-based grid generation software developed by Ansys in Fluent-Meshing was used while creating the mesh. The main purpose of creating a mesh in CFD studies is to ensure a mesh structure with the high quality and low number of elements without sacrificing numerical accuracy. Thus, a balance between computation time and numerical accuracy can be achieved. For this purpose, mesh density is increased in the whole flow domain, where the resolution sensitivity is critical, by using the mesh refinement regions (i.e. Body of Influence or BOI) rather than the further regions of the domain. Two different BOIs were used, from the vehicle to the free stream: BOI I and BOI II and (Figure 3.3).

In addition, the mesh refinement tools of the software on elements of volume and surfaces were used to produce mesh of appropriate quality. This was ensured that the mesh quality was skewness <0.7 in all cases, which is quite a good value for such a complex flow field. (Lanfrit, 2005). In case of worse quality, CFD users may encounter difficulties in convergence and inaccurate results.

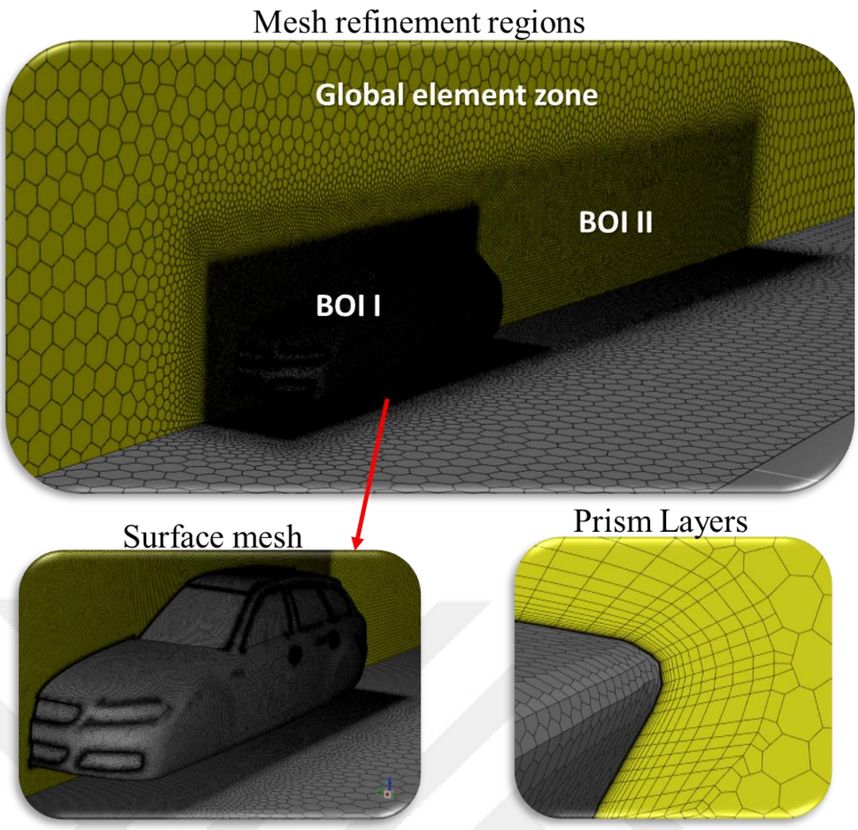

Figure 3.3. Views of the mesh structure and mesh refinement regions

In this study, Poly-Hexcore mesh element type, which has been developed in recent years, was utilized to obtain better mesh quality and numerical results with fewer mesh elements. Thanks to this type of mesh element, polyhedral mesh elements are used in transition zones, which give better results when transitioning from complex and narrow areas to free flow (Balafas, 2014), while hexahedral mesh elements are used in the freestream regions of the domain.

On the other hand, the correct resolution of the turbulent boundary layer is an critical issue in CFD simulations to accurately resolving or modelling the forces on the bodies subjected to flow (Schlichting and Gersten, 2016). In this sense, some users may use insufficient prismatic mesh layers or first mesh height incompatible with turbulence model in solution mesh.

Simulations were performed with meshes featured by the first cell height of h_0=0.04 mm. With this value of the first cell height, the y^+<5 condition was ensured, which is a requirement for the turbulence model used in this study (k-ω SST) to give accurate results (Menter, 1992). For more details on turbulent boundary layer, y^+, and how prismatic layers should be generated to resolve highly-gradient flow regions, readers can apply (Cengel ve Cimbala, 2006; Schlichting ve Gersten, 2016; Soares ve De Souza, 2015b) references.

The mesh independence test is based on the principle of determining the amount of mesh for vehicle aerodynamics simulations, at which a quantitative result (commonly C_D, C_L, C_P or velocity profile taken from the wake region etc.) is fixed while increasing the mesh number gradually (Şimşek, 2020; Yılmaz ve Çiçek, 2017). In this study, 3 different mesh levels obtained by changing the dimensions of the global mesh elements and the regions BOIs were tested. The characteristics of the mesh levels shared in Table 3.2.

Table 3.2. Dimensions used in the mesh independency tests

Grid Level		**Mesh 3**	**Mesh 2**	**Mesh 1**
Mesh element size (BOI I)		30 mm	20 mm	10 mm
Mesh element size (BOI II)		40 mm	30 mm	20 mm
Mesh element size (BOI III)		200 mm	150 mm	100 mm
First cell height at no-slip walls (h_0)		0.04 mm	0.04 mm	0.04 mm
Total elements of inflation layers (n_P)		20	20	20
Refinement ratio of the inflation layers		1.2	1.2	1.2
Total mesh counts*	**E**	1122037	2588710	6053255
	F	1080098	2416661	6046474
	N	1053810	2442436	6015424
* *E: Estateback F: Fastback N: Notchback*				

From this point of view, closed body DrivAer vehicle models were subjected to mesh independence tests using the k-ω SST turbulence model in Ansys Fluent CFD software. With the three different mesh resolutions created in these tests, a new fourth mesh level was created using Richardson extrapolation and GCI methods, which is closer to the experimental data and the mesh independence is satisfied to the desired level. The results were analyzed in terms of aerodynamic drag force coefficients.

3.3.1. Richardson Extrapolation

To ensure turbulent flow is modeled correctly in mesh independence tests, the mesh growth rate (r) must be greater than 1.3. (Celik et al., 2008). The mesh growth rate factor (r) is calculated as follows:

$$r_{21} = \frac{h_2}{h_1} \tag{1}$$

$$r_{32} = \frac{h_3}{h_2} \tag{2}$$

where 3, 2 and 1 indices stand for Mesh 3, Mesh 2 ve Mesh 1 levels while h is the average size of a mesh element in the flow domain. In a three-dimensional flow field, h is calculated as:

$$h_{ave} = \left[\frac{1}{N}\sum_{i=1}^{N}(\Delta v_i)\right]^{\frac{1}{3}} \tag{3}$$

where, N represents the total number of mesh elements used for the calculation, while Δv_i is the total volume of the mesh element indicated by the number in its subscript. The values of the above-mentioned parameters of the corresponding mesh levels in this study are shown in Table 3.3.

Table 3.3. Parameter values of the mesh levels

Vehicle Model	Parameter	Mesh 1	Mesh 2	Mesh 3
Estateback	Total mesh counts (N)	6053255	2588710	1122037
	Average cell size (h_{ave})	0.0432	0.0574	0.0758
	Mesh refinement ratio (r)	R_{21}=1.32	R_{32}=1.33	
Fastback	Total mesh counts (N)	6046474	2416661	1080098
	Average cell size (h_{ave})	0.0432	0.0587	0.0468
	Mesh refinement ratio (r)	R_{21}=1.36	R_{32}=1.31	
Notchback	Total mesh counts (N)	6015424	2442436	1053810
	Average cell size (h_{ave})	0.0433	0.0585	0.0774
	Mesh refinement ratio (r)	R_{21}=1.35	R_{32}=1.31	

Richardson extrapolation is a numerical method for estimating the value of a function for a given point or interval that is difficult or impossible to calculate analytically, using the value of at least two known points of the curve (Single et al., 1927). For CFD, by the adaptation of this method, the flow area is divided into an infinite mesh element (h→0) and it is possible to calculate the output values. The idea of that the dimensional discretization can be infinite was put forward by Roache. (Roache, 1997). On the other hand, in order to use extrapolation in CFD studies, it was stated that at least three mesh levels should be created (Stern et al., 2001). The equation of Richardson extrapolation is formulated as the p^{th} degree method as follows:

$$f_{RE} \approx f_1 + \left[\frac{f_1 + f_2}{r^p - 1}\right] \tag{4}$$

where r is the mesh growth rate as stated in the formulas in (1) and (2), and f_i denotes the mesh level output result indicated by the number in the i index (for example, C_D). The extrapolation value changes according to the degree to which it will be calculated (p). The p-value is calculated as follows:

$$p = \frac{1}{lnr_{21}} \left| \ln \left| {}^{\varepsilon_{32}}/_{\varepsilon_{21}} \right| + q(p) \right| \tag{5}$$

$$\varepsilon_{32} = f_3 - f_2 \tag{6}$$

$$\varepsilon_{21} = f_2 - f_1 \tag{7}$$

$$q(p) = \ln \left(\frac{r_{21}^p - s}{r_{32}^p - s} \right) \tag{8}$$

$$s = sign\left(\varepsilon_{32}/\varepsilon_{21}\right) \tag{9}$$

Here, it should be known that in cases where the mesh growth rate is constant ($r_{21}=r_{32}$), q(p)=0. However, in today's mesh software, it is often not possible to keep this ratio precisely constant.

It should be noted that numerical solution methods such as Regula False or Newton Raphson can be used to calculate equation (5). As can be seen in Table 3.3, the mesh growth rate is not constant in this study.

To determine the reliability of the values obtained by extrapolation calculations, the state of convergence (R) must be determined:

$$R = \frac{\varepsilon_{21}}{\varepsilon_{32}} \tag{10}$$

There are three possibilities for R:

1. Monotonic convergency (0 <R< 1)
2. Oscillatory convergency (R<0)
3. Divergency (R>1)

For a higher accuracy solution and convergence, it is suggested that the convergence state (R) should be in the monotonic convergence state (Shaharuddin et al., 2018).

3.3.2. Grid Convergence Index (GCI)

GCI is a method that ensures more regular and reliable results as the mesh sizes approach zero for mesh independence tests. In this method, calculations are based on the fractional error derived by Richardson extrapolation. The GCI calculates the percentage error of a mesh resolution to the asymptotic range, i.e. to the result of the numerical simulation that has become mesh independent. The small value of GCI indicates that the numerical result approaches the asymptotic result. Thus, it aims to minimize spatial discretization errors in CFD simulations. However, it should be noted there that the asymptotic range of values may guarantee acquiring the actual physical results. This is because error sources such as temporal discretization, physical modeling, simplification in geometry modeling, mathematical rounding, iterative convergence can also affect the result. GCI is calculated as follows for different mesh resolution levels:

$$GCI_{i+1,i} = F_s \frac{|\varepsilon_{i+1,i}|}{f_i(r^p - 1)} \times 100\% \tag{11}$$

where F_s, denotes safety factor. (Wilcox, 2006) stated that the factor of safety should be 1.25 for three or more levels of mesh resolution.

The error rates found by comparing the calculation results to the experimental situation are calculated as follows:

$$E_i = \left|\frac{f_{experimental} - f_i}{f_{experimental}}\right| \times 100\% \tag{12}$$

The parameter values of the GCI and extrapolation equations of the simulations for Mesh 1, Mesh 2 and Mesh 3 are presented in Table 3.4.

Table 3.4. GCI and Richardson extrapolation values for mesh levels

	$\lvert\varepsilon_{32}\rvert$	$\lvert\varepsilon_{21}\rvert$	**R**	**p**	GCI_{32}	GCI_{21}	GCI_{32}/r^pGCI_{21}
Estateback	-0.0262	-0.0083	0.3168	4.155	%8.77	%2.58	1.05
Fastback	-0.0169	-0.0059	0.3491	4.173	%9.84	%2.60	1.06
Notchback	-0.0232	-0.0072	0.3103	4.301	%10.96	%2.83	1.06

When the values are observed, there is a monotonic convergence situation for all three different vehicle models. On the other hand, it is seen that all GCI values are higher than 10% in the transition from Mesh 3 to Mesh 2. It is known that better results were obtained when the GCI value was less than 5% between the highest resolution mesh and the previous coarser mesh (Sukri et al., 2009). In the transition from Mesh 2 to Mesh 1 level, this condition is provided for all models. For the GCI_{21}, values of 2.58%, 2.60% and 2.83% were obtained in the estateback, fastback, and notchback models, respectively.

On the other hand, ensuring the $GCI_{32}/r^pGCI_{21} \approx 1$ in a CFD study is an indication that the solution is in the asymptotic value range. If the solution is not in the asymptotic range, the simulations cannot be said to be independent of the mesh. (Baker et al., 2020). It can be said from the findings in this study, this condition is satisfied for all three models.

On the other hand, the formula for estimating the next mesh growth rate (r*) to achieve a desired mesh convergence index (GCI*) is:

$$r_* = \sqrt[p]{GCI_{12}/GCI_*} \tag{13}$$

Using the above equation (13), the mesh growth rate (r*) is estimated for the next mesh resolution. Considering the GCI*=1 condition as the target, it is calculated that the new mesh resolution (Mesh*) for estateback, fastback, and notchback models should be created with 12 million mesh elements. The results for Mesh 1, Mesh 2, Mesh 3, calculated by Richardson extrapolation (RE) and for the new mesh level (Mesh*) generated for the case GCI*=1 are shown in Figure 3.4. C_D results of the DrivAer models and errors comparing to experimental results are shown in Table 3.6.

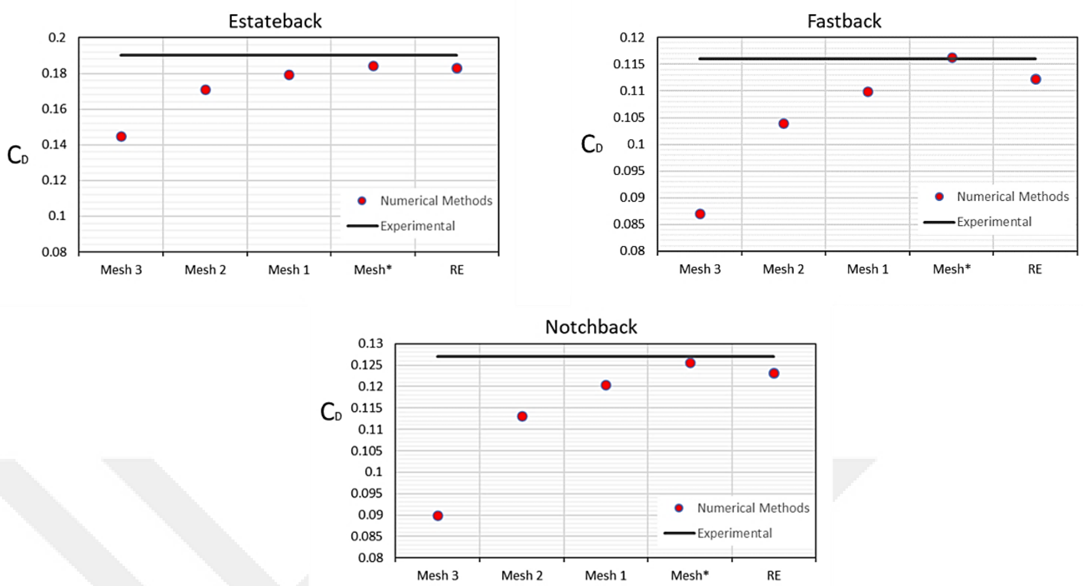

Figure 3.4. C_D outputs of the DrivAer configurations vs. calculation methods

Table 3.5. C_D results of the DrivAer models and errors comparing to experimental results

Model	Parameter	Mesh 3	Mesh 2	Mesh 1	Mesh*	RE
Estateback	C_D	0.1449	0.1711	0.1794	0.1844	0.1831
	E_i	23.74%	9.95%	5.58%	2.95%	%3.63
Fastback	C_D	0.0871	0.104	0.1099	0.1163	0.1122
	E_i	24.91%	10.34%	5.26%	0.26%	3.29%
Notchback	C_D	0.0905	0.1132	0.1204	0.1256	0.1231
	E_i	29.13%	10.87%	5.20%	1.10%	3.05%

When the results are examined, it can be seen that the error ratios are higher for Mesh 3 and Mesh 2 compared to the experimental data. It can be considered that the main reason for this situation is that DrivAer geometries require more mesh elements because of their complex geometry. As a matter of fact, when the CFD studies on DrivAer vehicle models are examined in the literature, the number of total mesh count is 50 million, even 200 million in some cases, in order to obtain accurate results (N. Ashton et al., 2016; N. Ashton and Revell, 2014; Neil Ashton and Revell, 2015; Emmanuel Guilmineau, 2014; Yazdani, 2015). For the Mesh 1 resolution level, the E_i<6% condition, which is more acceptable, could be obtained in all models. The values calculated by Richardson extrapolation were found with an error ratio of less than 4% in all models. The results closest to the experimental data were observed for the Mesh*. It can be said that 12 million mesh elements resulted in approximately with the same error ratios as the results commonly obtained with much more mesh elements counts in the literature. For instance, although Yazdani utilized 200 million mesh elements and an unsteady Spalart-Allmaras DDES hybrid turbulence model which requires substantial computational source and time, he attained C_D values with error ratios of 14.66%, 2.63%, and 10.24% for the fastback, estateback, and notchback models, respectively (Yazdani, 2015).

3.4. Numerical Setup

Setup stage of a CFD simulations involve acknowledged errors, iterative convergence errors, round-off errors, and physical modelling errors. To prevent these error resource rigorous usage of the solver is essential, hereby accuracy of the solutions can be sustained.

In this study, an incompressible, steady-state RANS approach has been adopted. As turbulence models, Menter's k-ω Shear Stress Transport (SST) (Menter, 1992) that have been widely used and validated in the literature (E. Guilmineau et al., 2018; Huminic and Huminic, 2017; Mohammadikalakoo et al., 2020; Siddiqui and Chaab, 2020; Chunhui Zhang et al., 2019) was utilized in this study. The model is a two-equation model that provides a solution to the RANS with a reasonable degree of accuracy at a reasonable computational expense. Despite Detached Eddy Simulations (DES), Large Eddy Simulations (LES), and Unsteady Reynolds-Averaged Navier-Stokes (URANS) ensure more accuracy for the flow field this would probably require much increased computational cost and power and hence, is out of the scope of this investigation. Moreover, there are various studies achieving reasonable accuracy used steady-state RANS turbulence models with cost effective mesh (Heft et al., 2012b; Renan F. Soares et al., 2017; Renan Francisco Soares and De Souza, 2015b).

While setting boundary conditions, the side and top walls were set as symmetry boundary condition in this CFD study, a method frequently used in the literature. With this method, it can be thought that the blocking effects are eliminated by defining the free slip condition on the top and side walls. In addition, the input velocity was entered as U=45 m/s to satisfy the $Re_L=5.2\times10^6$ condition. Details on the flow domain and the boundary conditions are shared in Figure 3.2 and Table 3.6.

Table 3.6. Boundary conditions setup used in the numerical simulations.

	Inlet	**Outlet**	**Ground**	**Top and Side walls**	**Vehicle surface**
Boundary Condition	Velocity Inlet	Pressure Outlet	Moving wall	Free-slip wall	No-slip wall
Value	45 m/s (uniform)	0 Pa	45 m/s	Zero shear stress	-

For numerical simulations, steady RANS equations were solved with a pressure-based, adiabatic, coupled solver without gravitational effects. At the inlet, reference pressure and temperature values of air were set $p_\infty = 1$ atm $t_\infty = 15\,°C$, respectively. The air freestream velocity was kept $U_\infty = 45\ m/s$ corresponding to a Reynolds number of $Re_L=5.2\times10^6$ (based on body length), and the turbulence intensity was 0.1 % at the velocity inlet. The pressure outlet was set to a gauge pressure of 0 Bar with 5% turbulence intensity at the exit.

To prevent iterative convergence error sources, it was ensured that all residuals were kept below 10^{-6} while only continuity residuals were below 10^{-4} throughout all simulations. Moreover, variances in coefficients of C_D and C_L were below 1 count by monitoring them. After the above-mentioned convergency criteria was satisfied, simulations have been conducted for 50 more iterations. On the other hand, 2^{nd} order upwind schemes were used for all corresponding turbulent quantities and double precision was set for all simulations to minimize the numerical round-off error sources. Pressure-velocity coupling was enabled by using SIMPLE algorithm. The brief scheme of the CFD procedures during the simulations in this study is presented in Figure 3.5.

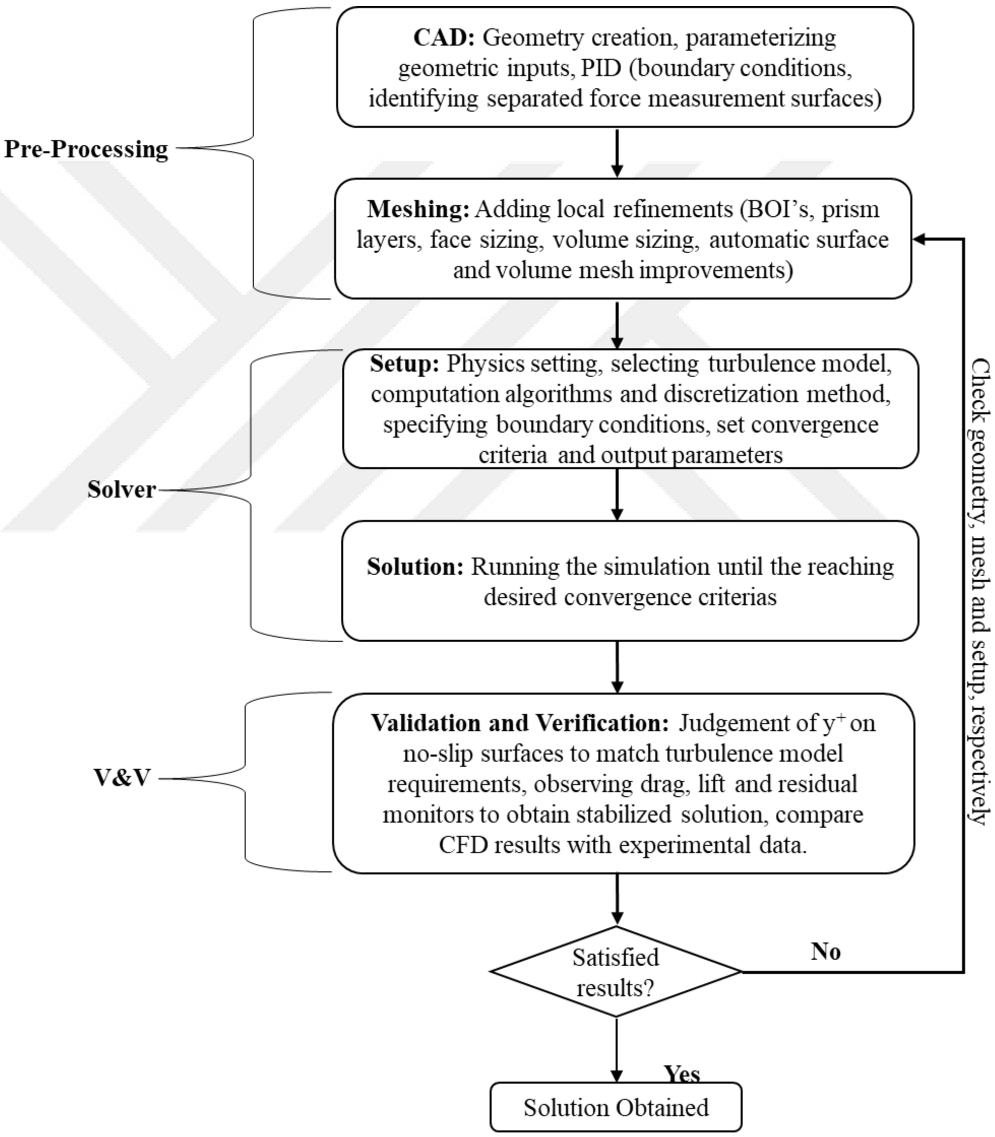

Figure 3.5. CFD procedures used in the numerical simulations.

3.5. Optimization Procedures

3.5.1. Parametric Optimization

Parametric optimization is one of the most often used gradient-free optimization techniques aiming to optimize considered (input) design variables to obtain minimum, maximum, or target value for (output) objective variables. In this paper, deflector angle (α) is the main design variable to optimize for achieving the minimum C_D objective variable for DrivAer generic vehicle. In parametric optimization, the α was varied between -15° to 45° with an angle increment of 5°. Length of the deflectors were parameterized, too. Nevertheless, since the curve shows a linear behavior in direct proportion to the deflector length, multi-objective optimization of the deflector angle would be redundant effort and increase the design points remarkably. Therefore, the deflector length was kept constant and only the deflector angle was examined as a design parameter. Finally, the parametric data set was used in the response surface optimization process as DOE. 54 design points were simulated throughout the parametric optimization procedure for all flow control elements of estateback, fastback, and notchback DrivAer models.

3.5.2. Response Surface Optimization

Following the parametric optimization, global minimum search algorithms of Response Surface Optimization have been used for numerical optimization. To seek for candidate minimum global minimum of C_D Genetic Algorithm was employed according to response surface of design parameter of α. The Genetic Algorithm was proposed by John Henry Holland (Holland, y.y.) in the 1970s and developed by Goldberg (Goldberg and Holland, 1989) in 1989. This algorithm is widely used to acquire high-fidelity solutions for optimization and search problems by relying on bio-inspired operators such as mutation, crossover, and selection.

To evaluate the effects of a phenomenon on a design, system, or process, it is indispensable to carry out some experiments for reducing cost and time factors. This necessity in industry and engineering resulted in the introduction of the design of experiments (DOE) technique. DOE requires a comprehensive and detailed process that significantly minimizes the cost and time or obtains a product with higher performance and reliability. While performing experiments and trial and error procedures, the primary objective is to observe the changes in output parameters by altering the design variables (Manshadi and Aghajanian, 2018).

In this study, Response Surface was used to optimize the response of interested design variables as an approximation method. Since the response surface method is reproduced on the DOEs, data provided by the parametric simulation results of CFD were used to create the Response Surface of design parameter of α. If the solution is adequately modeled by a linear function of independent design variables (or parameters), the function of approximation for the first-order model is:

$$f(x) = B_0 + B_1x_1 + B_2x_2 + \cdots + B_kx_k + \in \tag{14}$$

However, in the case of curvature response of design variables, higher-order polynomials should be modeled:

$$f(x) = B_0 + \sum_{i=1}^{k} B_ix_i + \sum_{i=1}^{k} B_{ii}x_i^2 + \sum_{i=1}^{k} B_{ij}x_ix_j + \in \tag{15}$$

where x_i and x_j stands for the design parameters, b, and $\in$ are the tuning parameters and error observed in the objective function $f(x)$, respectively.

In this paper, some of upper and lower deflectors were studied by applying parametric data as DOE to attain high quality and comprehensive model based on Response Surface Optimization. As a result of Genetic Aggregation based Response Surface Optimization, the candidate model for the global optimum of C_D. To enhance the reliability of the reliability of the candidate design points which were proposed by response surface optimization, these design points were verified as well as close values of the optimum design parameters by performing further simulations.

3.5.3. Adjoint Optimization

Computational Fluid Dynamics (CFD) is a central element of the automotive development process. Besides the classical external aerodynamics for the prediction of drag and lift coefficients, there is a whole plethora of applications for ducted flows: airducts for cabin ventilation, engine intake ports, exhaust systems including catalytic converters, air intakes, water jackets of cylinder heads, cooling plates for electric vehicle battery packs and many more. The standard procedure of developing these parts still consists of manual iteration loops between designer and computational engineer, and automatic optimization methods are being used systematically only for some selected CFD applications. Via an automatic process chain consisting of a CAD (Computer-Aided Design) system, meshing software, CFD solver and post-processor a black-box optimization algorithm, typically of the evolutionary strategy type, is employed to drive a parameterized CAD-model into an optimal state. Due to the high computational effort associated with black-box optimization, where the number of CFD evaluations scales roughly linearly with the number of design variables, the explorable design space is very limited: In our current practice, these methods cannot afford more than ten design parameters. An additional obstacle that inhibits the further adoption of black-box optimization within the regular automotive development process is the necessity of a versatile but stable CAD parameterization. For e.g., an engine intake, the setup of the parameterized model might take an experienced CAD engineer several weeks before it comes up to the stability requirements of an automatic optimization process chain. It is these limitations that call for a radically different approach to automotive CFD optimization especially in view of applications like entire vehicle aerodynamics that entail shape optimization of highly complex free-form geometries with a practically un- limited design space.

Traditionally, it involves manual loops of design modification and performance evaluation, which is not efficient. To improve the efficiency of this process, the combination of gradient-based optimization and the adjoint method for computing derivatives can be used to automatically optimize the design. The true benefit of using the adjoint method to compute derivatives is that its computational cost is almost independent of the number of design variables, which enables complex industrial design optimization.

Two different methods exist for formulating the adjoint of a flow solver: continuous and discrete. The continuous approach derives the adjoint formulation from the Navier–Stokes (NS) equations and then discretizes to obtain the numerical solution. In contrast, the discrete approach starts from the discretized NS equations and differentiates the discretized equations to get the adjoint terms. Although these two approaches handle adjoint formulation in different ways, they both converge to the same answer for a sufficiently refined mesh.

A gradient-based optimization (GBO) with discrete adjoint solver procedure for CFD involves computing the total derivative of df/dx , where f is objective function depends on design variables of x (boundary mesh, velocity inlet, boundary conditions, etc.) and state variables of w that determined by the solution of governing equations. Surface sensitivities were constructed for objective functions, (drag force) and x represents the design variable that controls the geometric shape via control points.

As mentioned earlier, to conduct GBO for aerodynamic shape optimization, the total derivative of df/dx must be calculated. Flow solution (f) depending on design variables (x) and state variables (w) is:

$$f = f(x, w) \tag{16}$$

where the design variables vector of $x = [\, x_1\,, x_2\,, x_3\,, \ldots, x_{n_x}\,]^T$ has length n_x, and $w = [\, w_1\,, w_2\,, w_3\,, \ldots, w_{n_w}\,]^T$ is the state variables vector with length n_w. With the implementation of the chain rule for the total derivative, we obtain:

$$\frac{df}{dx} = \frac{\partial f}{\partial x} + \frac{\partial f}{\partial w}\,\frac{dw}{dx} \tag{17}$$

It would be computationally expensive for many design variables as the computation of dw/dx via finite differences methodology would necessitate solving the governing equations n_x times. It can be avoided by using the fact that the residual derivatives w.r.t. the design variables must be zero for the governing equations to remain feasible w.r.t. variations in the design variables. Hence, with the application of the chain rule to the residuals, it can be written that:

$$\frac{dR}{dx} = \frac{\partial R}{\partial x} + \frac{\partial R}{\partial w}\frac{dw}{dx} \tag{18}$$

Where $R = [R_1, R_2, R_3, \ldots, R_{n_w}]^T$ is the flow residual vector. By substituting Equation (18) into Equation (17) and removing the dw/dx term:

$$\frac{df}{dx} = \frac{\partial f}{\partial x} - \frac{\partial f}{\partial x}\left(\frac{\partial R}{\partial w}\right)^{-1}\frac{\partial R}{\partial x} \tag{19}$$

By combining the $\partial R/\partial w$ and $\partial f/\partial w$ terms in Equation (6), the following equation can be solved linearly:

$$\frac{\partial R^T}{\partial w}\psi = \frac{\partial f^T}{\partial w} \tag{20}$$

to attain the adjoint vector $\psi = [\psi_1, \psi_2, \psi_3, \ldots, \psi_{n_w}]^T$. Then, by ψ is substituting into Equation (20) to solve the total derivative:

$$\frac{df}{dx} = \frac{\partial f}{\partial x} - \psi^T\frac{\partial R}{\partial x} \tag{21}$$

As x does not explicitly appear in Equation (20), Equation (21) should only be computed once for each function of interest hence, the required cost is almost independent of the number of design parameters, computationally. This is advantageous for a 3D optimization process since the number of f is usually less than ten whereas the number of design variables can be greater than ten f (He et al., 2018). In Ansys Fluent, Algebraic Multigrid (AMG) iterative approach is performed to solve an approximate solution to Equation (21). In the following step, the modified geometric model (Adjoint) is attained by moving the cell nodes using control points.

A Mesh deformation routine generally parametrizes the geometry with control points where the number of control points is much smaller than the number of grid points. The adjoint CFD solver provides sensitivity derivatives for all mesh nodes. To be used in conjunction with an adjoint CFD solver, the deformation routine also must handle sensitivity propagation from the grid points to the control points. The sensitivity computation could be left to automatic differentiation.

Mesh morphing was restricted to a region slightly larger than the upper and lower deflector sections. Equal spacing and greater distance than minimum surface mesh element strategies between control points were retained. Subsequently, numerical simulation is solved again for the new mesh. This corresponds to one design iteration for GBO. To achieve the target value (-1%) of a given objective function (drag force) 5 design iterations were performed in the current study. Keeping target value and design iterations as low as this value was a part of the strategy of the preventing mesh morphing issues. For more detail about GBO, AMG approach, and discrete adjoint solver of Ansys Fluent, the Ansys Adjoint Solver Manual can be seen in (ANSYS, 2013). The whole optimization framework conducted in this study is shown in Figure 5.

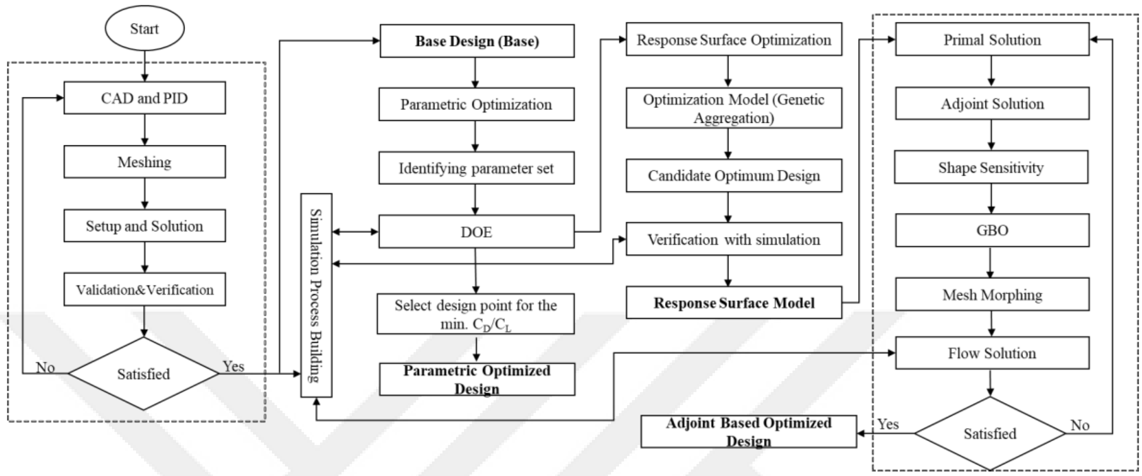

Figure 3.6. Optimization framework procedure used in this study.

3.6. Flow Control Methodology

Deflector plates are used to control wake flow for different applications of fluid mechanics. In this study, they were used to minimize aerodynamic drag force by aiming deflection of the upwash and downwash flows to the wake region. Hence, it was aimed that momentum transfer would be controlled by a deflector with a certain angle and it could influence the wake region. As shown in Figure 3.7, deflector plates were mounted on the upper and lower side edges of the DrivAer models. Besides, slant angle of the deflectors is shown in figure denote positive values of the angle parameter.

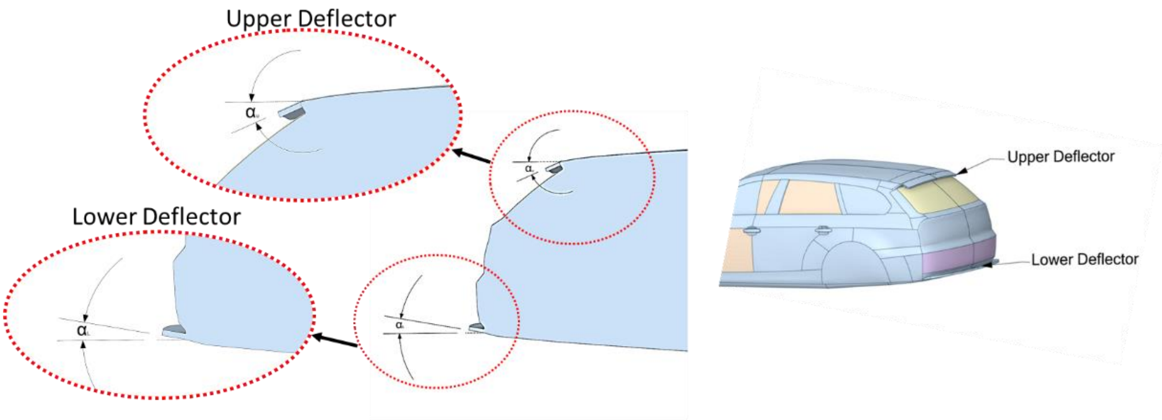

Figure 3.7. Deflector flow control elements and their locations

As a result of the optimization procedures, optimum deflector shape was tried to seek for minimum aerodynamic drag. However, optimization works were conducted for upper and lower deflectors, separately. After the determining the optimum shapes for upper and lower deflectors, the combined usage of the flow control tools was simulated. Eventually, to evaluate the effectiveness and influences of upper and lower deflectors, base model was compared with three different models equipped with upper, lower, and combined upper + lower deflector plates.

3.7. Power and Fuel Saving Rate

As Fluent software can only obtain the simulation result of the aerodynamic drag of the vehicle, it needs to establish the mathematical model of the aerodynamic drag and the fuel saving rate of the vehicle to obtain the vehicle fuel-saving rate based on the simulation result of the aerodynamic drag of the vehicle.

This work studies the situation of a vehicle traveling at a constant speed on a straight and well road. According to the theory of automobile (Z. Yu, 2009) the equation of vehicle driving is shown in the following formula:

$$F_t = F_f + F_w = Mgf + 0.5C_D A_F \rho {V_r}^2 \quad (22)$$

Where F_t is the vehicle driving force (N), F_f is the rolling resistance (N), F_w is the air resistance (N), M is the net force on the vehicle (kg), g is the acceleration of gravity (m/s^{-1}), f is the rolling resistance coefficient, C_D is the aerodynamic drag coefficient, A_F is the frontal (m^2), ρ is the air density (generally ρ=1.225 kg/m^3), and V_r is the driving speed (m/s). This work ignores the impact of natural wind on the driving and unit speed change (V_r is converted to U, m/s). The following formula shows the air resistance of the driving vehicle.

$$F_w = \frac{C_D A_F \rho U^2}{2} \quad W$$

The following calculates the rolling resistance coefficient as a function of vehicle speed .

$$f = 0.005 + \frac{1}{p}(0.01 + 0.0095\left(\frac{U}{360}\right)^2 \quad (24)$$

Where p denotes tire pressure (bar) in the formula. Moreover, engine power can be calculated from the formula:

$$P = \frac{F_t U}{\eta_t} \quad (25)$$

where η_t is the transmission system mechanical efficiency. The fuel consumption per one hundred kilometers at constant speed of a car (L/100km) is calculated in the following formula.

$$Q_s = \frac{Pb}{1.02U\rho g} \quad (26)$$

where b is the fuel consumption (g/kWh) and ρ is the fuel density (kg/L). On the other hand, net force exerted on the vehicle can be calculated in the following formula.

$$M = \left(m - \frac{F_L}{g}\right) = m - \frac{0.5C_L A_F \rho U^2}{g} \quad (27)$$

Formula (28) defines the rate of reduction of the aerodynamic drag coefficient and Formula (29) defines the rate of fuel saving.

$$\Delta C_D = \frac{C_{D0} - C_D}{C_D} \quad (28)$$

$$\Delta Q_s = \frac{Q_{s0} - Q_s}{Q_{s0}} \quad (29)$$

In Formulae (28) and (29), Q_{s0} is a 100-km fuel consumption with the base vehicle, and C_{D0} is the drag coefficient.

From Formulae (22) to (29), the authors can derive the relationship between saving rate and aerodynamic drag coefficient reduction rate (see Formula (30)), where $\mu = \frac{2Mgf}{C_{D0}A_F U^2}$.

$$\Delta Q_s = \frac{\Delta C_D}{1 + \mu} \quad (30)$$

On the other hand, power saving rate can be calculated as:

$$P_S = U(\Delta F_f + \Delta F_w) = 0.5A_F \rho U^3 (f \Delta C_L + \Delta C_D) \quad (31)$$

Where Δ symbolized parameters stand for change in value between the base model and flow-controlled model. Assumed parameters used in this paper to calculate the power and fuel saving rate are shown in Table 3.7.

Table 3.7. Parameters used in this paper to calculate the power and fuel saving rate

m	**g**	**ρ**	**U**	**f (based on U)**	**A_F**	**p**
1500 kg	9.81 m/s^{-1}	1.225 kg/m^3	45 m/s	0.015	1.09 m^2	2.3 bar (33 psi)

4. RESULTS AND DISCUSSIONS

In this section, quantitative values of aerodynamic forces on the vehicle versus as well as the wake statistics are presented. For the quantitative evaluations, different planes and zones were investigated to obtain wake statistics. Figure 4.1 and Figure 4.2. show the used planes and zones to illustrate the locations of the captured wake statistics. Besides, the identification of the wake region at the symmetry plane used in this paper is demonstrated in Figure 4.3.

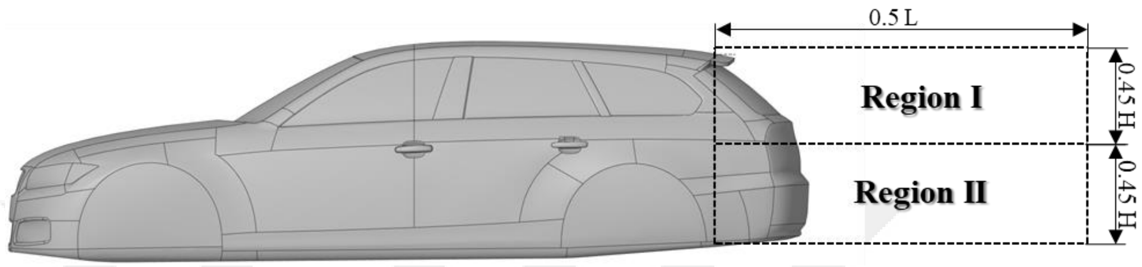

Figure 4.1. Illustration of Region I and Region II zones used in the wake statistic results.

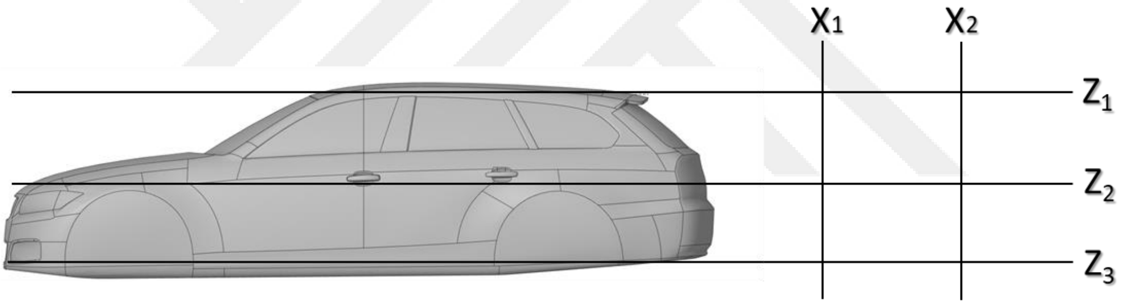

Figure 4.2. Sectional planes used in the wake statistic results.

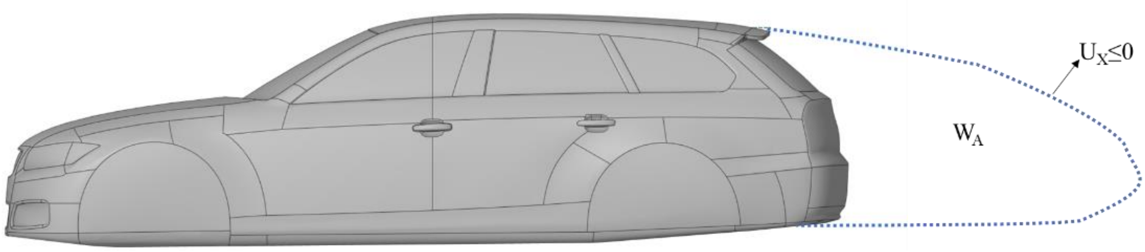

Figure 4.3. Wake region and its borders

4.1. Validation

In order to validate numeric simulations performed in this study, aerodynamic drag coefficient results of the three different closed-body DrivAer models (estateback, fastback, and notchback) without wheels, mirrors, detailed underbody, and engine flow were compared with the experimental data of the (Mack et al., 2012; Miao et al., 2015). The comparison results of the investigation are depicted in Table 4.1, Table 4.2, and Table 4.3 for base configurations of estateback, fastback, and notchback, respectively.

Table 4.1. Comparison of force coefficients of CFD setups with the experimental data for the estateback model

	Estateback (Mack et al., 2012; Miao et al., 2015)	***Estateback*** (Mack et al., 2012; Miao et al., 2015)	***Current CFD Study (Estateback)***
Re_L	*$5.2x10^6$*	*$5.2x10^6$*	*$5.2x10^6$*
Ground	No-slip	Moving	Moving
C_D	0.190	0.192	0.1844 (ΔC_D=7.6 counts)
C_L	-0.494	-0.446	-0.4838 (ΔC_L=37.8 counts)

Table 4.2. Comparison of force coefficients of CFD setups with the experimental data for the fastback model

	Fastback (Mack et al., 2012; Miao et al., 2015)	***Fastbackback*** (Mack et al., 2012; Miao et al., 2015)	***Current CFD Study (Fastback)***
Re_L	*$5.2x10^6$*	*$5.2x10^6$*	*$5.2x10^6$*
Ground	No-slip	Moving	Moving
C_D	0.116	0.117	0.1163 (ΔC_D=0.7 counts)
C_L	-0.345	-0.295	-0.3313 (ΔC_L=36.5 counts)

Table 4.3. Comparison of force coefficients of CFD setups with the experimental data for notchback model

	Notchback (Mack et al., 2012; Miao et al., 2015)	***Notchback*** (Mack et al., 2012; Miao et al., 2015)	***Current CFD Study (Notchback)***
Re_L	*$5.2x10^6$*	*$5.2x10^6$*	*$5.2x10^6$*
Ground	No-slip	Moving	Moving
C_D	0.129	0.127	0.1256 (ΔC_D=1.4 counts)
C_L	-0.370	-0.319	-0.3591 (ΔC_L=40.1 counts)

The aerodynamic results of this CFD study give good accuracy between numerical and experimental results. For the aerodynamic drag coefficient, error ratios compared to the experimental method (ΔC_D) are 7.6, 0.7, and 1.4 counts for estateback, fastback, and notchback models, respectively. However, error ratios for the C_L are slightly higher compared to the experimental method, numerically ΔC_L results are 37.8, 36.5, and 40.1 counts for estateback, fastback, and notchback models, respectively. Although these errors can be acceptable, they can be attributed to mirror and top strut inclusion of the experimental data. The absence of struts and mirrors in the numerical setups is possibly the reason for the underestimation of the C_D compared with (Mack et al., 2012; Miao et al., 2015). Although overestimation of the downforce is acceptable compared with the experimental data, error sources such as physical modeling of turbulence model, spatial discretization errors, iterative convergence, and round-off may also be responsible for the variance. Besides, it is also important to note that experimental studies may have erroneous results to some extent (S. Wang et al., 2019). Despite all, this order of deviation still can be assumed in the acceptable engineering limits by some researchers (Davidson, 2016; Dobrev and Massouh, 2014; Mohammadikalakoo et al., 2020).

4.2. Estateback

4.2.1. Quantitative Analysis for Estateback

Parametric optimization quantitative results of upper deflector plates are given in Figure 4.4 for C_D and C_L output of the estateback configuration. It can be seen from the graph that curves of C_D and C_L represent concave up and down behavior versus deflector angle. Minimum C_D output is obtained with a deflector plate of 25° slant angle. However, it can be seen that reducing C_D sacrifices downforce for all cases. Besides, parabolic characteristics of the curves may imply a further reduction in other words global minimum can be still further for the optimum deflector angle of the upper plate.

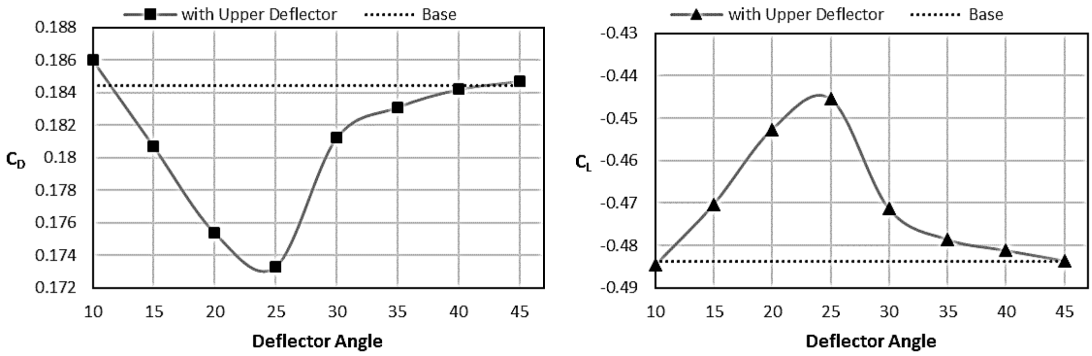

Figure 4.4. Parametric optimization results of estateback model with upper deflector

For the response surface optimization, the parametric optimization data set is used as DOE. Software predicts that an upper deflector plate with 23.75° could be a candidate point for the global optimum. To validate the result, the DrivAer estateback model with an upper deflector plate of 23.75° slant angle was simulated as well as closer values of the slant angles. As a result, the aerodynamic drag coefficient is reduced significantly with the response surface optimization tool (Figure 4.5). On the other hand, it can be said that the use of the upper deflector as a passive flow control element increases the C_L.

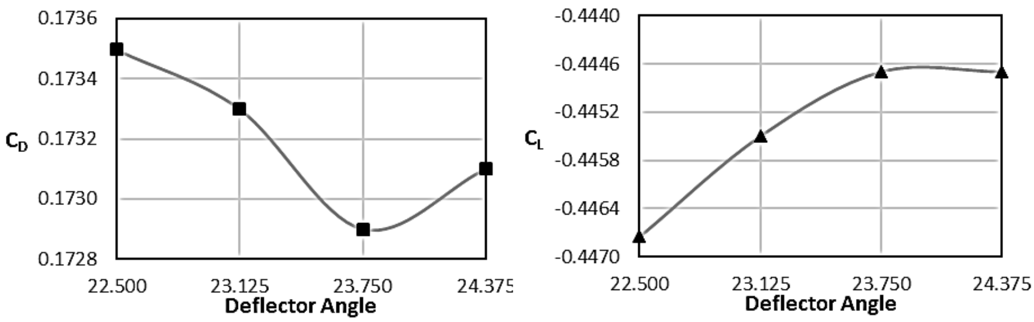

Figure 4.5. Response optimization results of estateback model with upper deflector

As for lower deflector plate usage, the curve of C_D is characterized by concave-up behavior versus deflector angle again (Figure 4.6). However, contrary to what is intuitively thought, minimum aerodynamic drag coefficient output is attained for the negative angle value of lower deflector plate with -5°. C_L output is substantially higher for lower values of deflector plates and reduces gradually with the increment of the deflector angle.

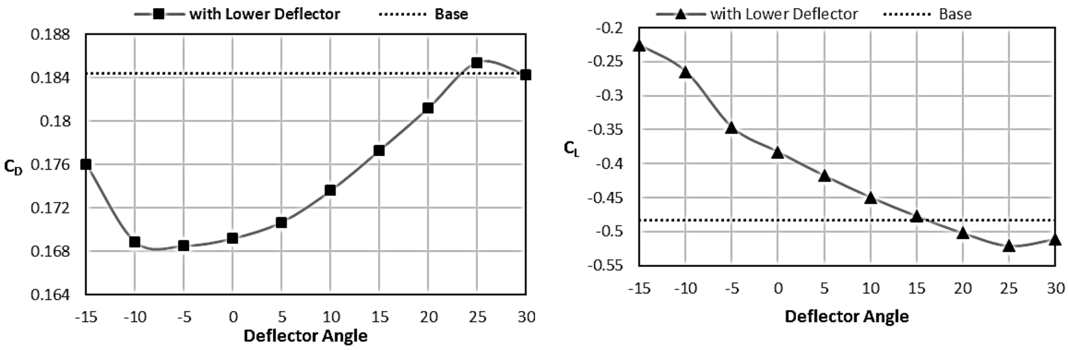

Figure 4.6. Parametric optimization results of estateback model with lower deflector

The parametric optimization data set is used as DOE for the response surface optimization. Software suggested that a lower deflector plate with -8° is a candidate design point for the global optimum. DrivAer estateback model with a lower deflector plate of -8° slant angle was simulated as well as closer values of the slant angles to verify the design point. Consequently, the aerodynamic drag coefficient is decreased remarkably with the response surface optimization tool (Figure 4.7). However, the use of the lower deflector as a passive flow control element caused downforce loss.

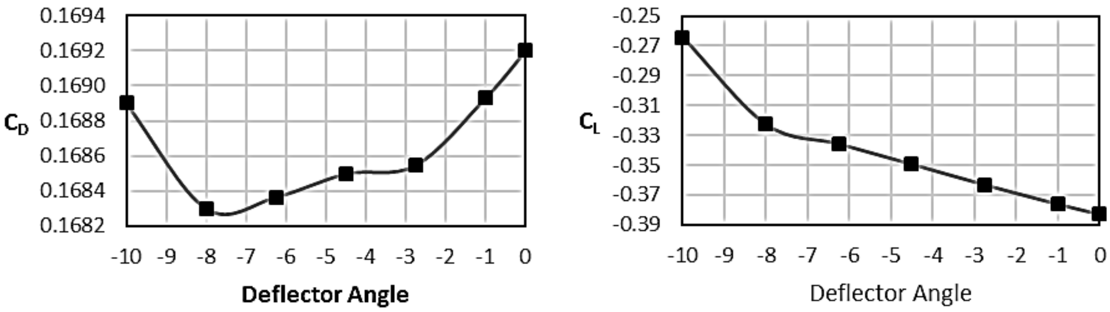

Figure 4.7. Response optimization results of estateback model with lower deflector

In the final step of the optimization process, adjoint optimizations were carried out to reduce the aerodynamic drag force further. Adjoint optimizations were conducted for upper and lower deflector plates, and the final design was obtained for both passive flow control elements. Consequently, the aerodynamic force results from the DrivAer estateback models with upper, lower, and combined upper + lower deflectors were compared with the base model in Figure 4.8. As a result, C_D values are reduced by 6.24%, 8.62%, and 17.90% for the estateback model equipped with lower deflectors and combined upper + lower deflectors, respectively. On the other hand, C_L output decreased by 8.08%, 28.44%, and 49.52% for the estateback model equipped with lower and combined upper + lower deflectors, respectively.

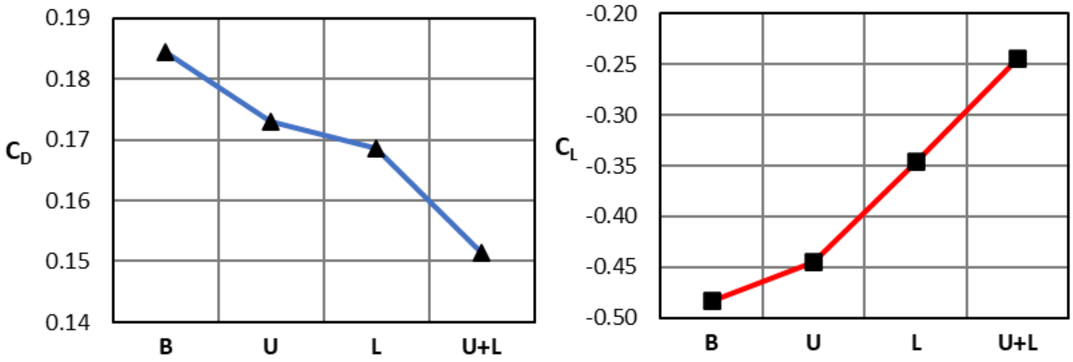

Figure 4.8. C_D and C_L results of the estateback without a deflector and with upper, lower, and upper + lower deflector.

To elucidate drag reduction mechanisms of the upper and lower deflector plates on the estateback model, detailed wake statistics are shared in Figures 4.9 and 4.10. Maximum and average TKE values for Region I and Region II is shown in Figure 4.9 while the wake area is presented in Figure 4.10. It is a known fact that estateback models have upwash-dominated wake flow (Avadiar et al., 2019), proof of this can be seen in the base model wake statistics. The huge difference in minimum and maximum values of TKE between the upper (Region I) and lower (Region II) regions of the wake is obvious. Due to the insufficient flow momentum on the roof of the vehicle, energy dissipation is remarkably higher compared with the lower region of the rear wake.

It can be seen that the upper deflector plate reduces TKE and wake area, significantly. Furthermore, upper and lower regions have more balanced wake statistics with upper deflectors. Nevertheless, an interesting result draws attention to the lower deflector plate. The contrary to drag reduction effect of a lower deflector, wake statistics increase significantly, and imbalance is higher between upper and lower regions. With the combined usage of upper and lower deflectors, this imbalance and turbulent statistics is reduced compared with the single usage of the lower deflector.

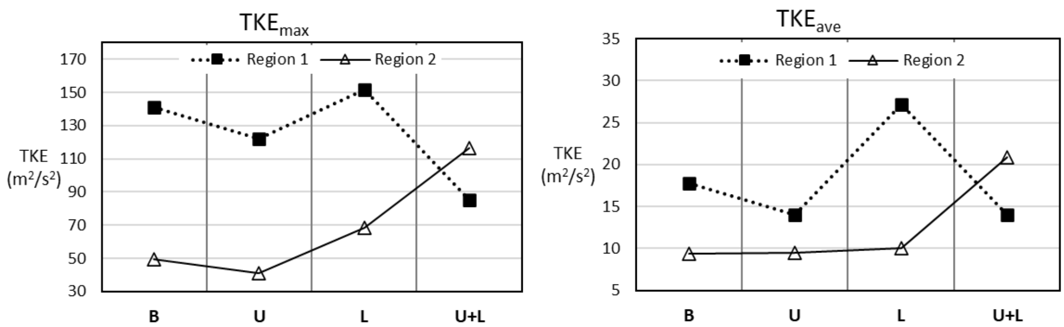

Figure 4.9. The maximum and average TKE values for estateback configurations in Region I and Region II.

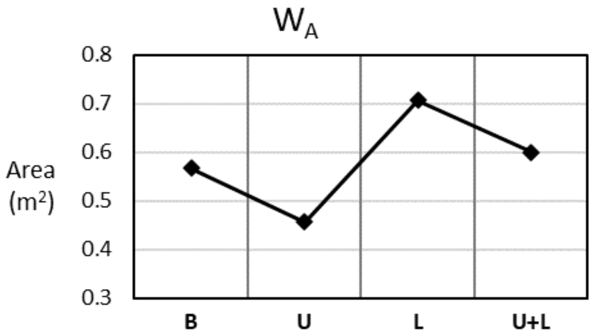

Figure 4.10. Wake area of estateback configurations.

4.2.2. Qualitative Analysis for Estateback

In this section, the upwash and downwash flow terms are used frequently to characterize airflow from the underbody and upperbody of the vehicle. To illustrate the upwash and downwash, readers can see Figure 4.11.

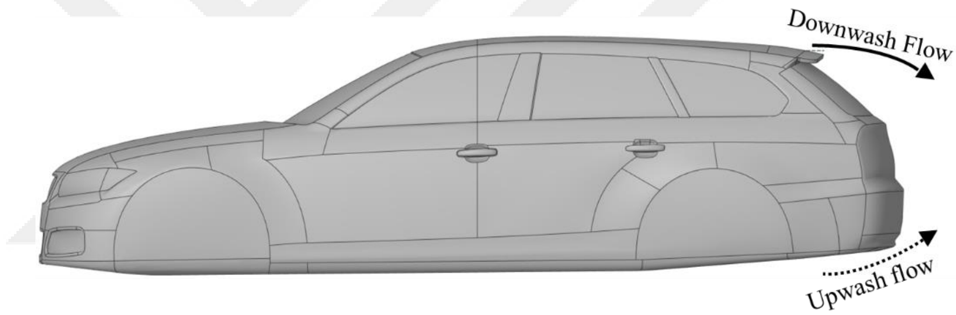

Figure 4.11. Illustration of the upwash and downwash flow.

Velocity contours of estateback DrivAer models without a deflector, with upper, lower, and upper + lower deflectors are shown in Figure 4.12. It can be seen that the upper deflector directs downwash flow to the middle of the wake region therefore, the interaction between the upwash and downwash is enhanced, and a narrower and elongated low-velocity region is assured compared with the base model. In the study of (Cho et al., 2018; Siddiqui and Chaab, 2020), it can be seen that flow control deflector usage elongates the wake region thus, it reduces aerodynamic drag. The narrower and longer wake of the upper deflector model is the indicator of drag reduction. It is reported that the estateback DrivAer model is characterized by strong upwash (Avadiar et al., 2019) therefore airflow has lower momentum at the upperbody of the estateback vehicles. By the way of the usage upper deflector, more balance between the upwash and downwash is ensured apparently. Although the upper and lower flow seems more converged, there is no full interaction between them. As for the lower deflector usage, the wake region is wider and longer contrary to upper deflector usage. However, the usage of a deflector with a negative slant angle leads to constraint airflow beneath the car. Strength of the upwash is reduced while more downwash flow is generated due the restricted flow. The stronger downwash elongated the wake and weaker upwash resulted in a wider wake by the usage of lower deflector. As stated before, elongated wake may reduce the aerodynamic drag while wider wake may cause a rise. The combined usage of the upper and lower deflectors resulted in strongest downwash and weakest upwash among all of them. The most balanced flow between upwash and downwash is apparent and flow interaction is the highest. Besides, both narrower and longer characteristics of the wake is sustained by the usage of combined upper and lower deflector, hence the lowest drag coefficient for the estateback model is obtained. Besides, flow upwash and downwash interaction is obtained with combined usage therefore, balanced energy dissipations on upper and lower regions can be attributed to this interaction. These results are in consistency with quantitative results it the sense of wake statistics of W_A.

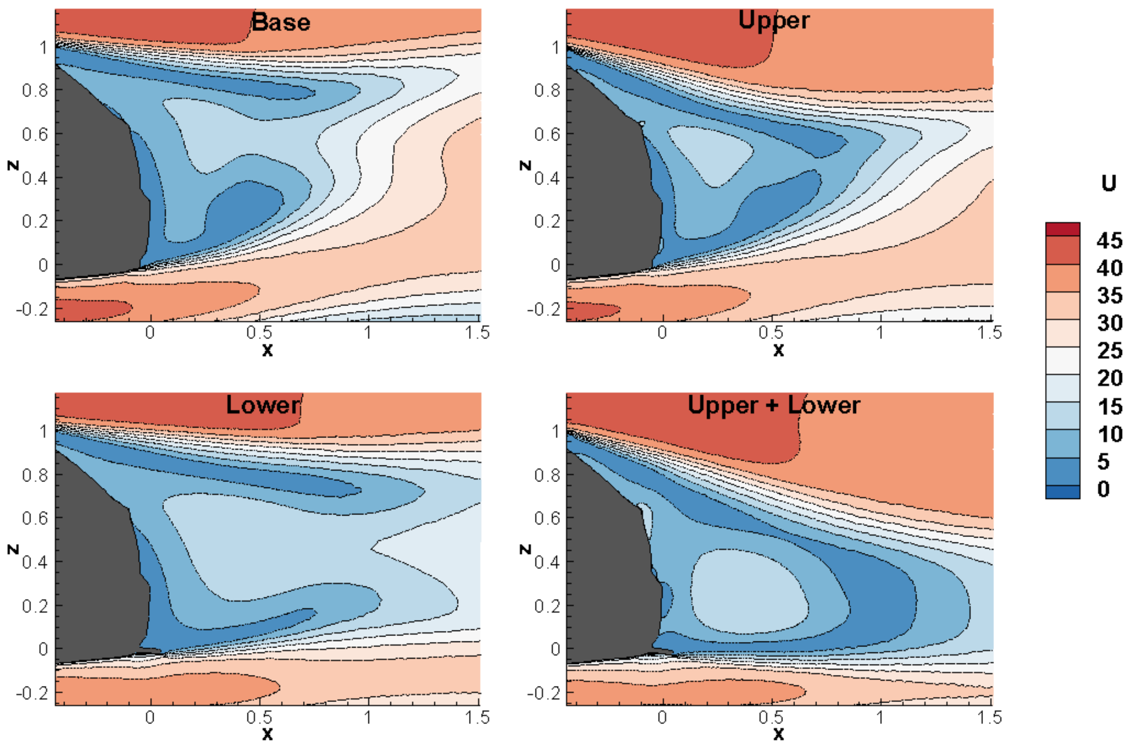

Figure 4.12. Velocity contours for estateback without a deflector and with upper, lower, and upper + lower deflector at symmetry plane.

Pressure coefficient contours for estateback without a deflector and with upper, lower, and upper + lower deflector at the symmetry plane are shown in Figure 4.13. It can be seen from the contours that upper deflector usage significantly increases the pressure at the wake and the higher-pressure zone is closer to the rear surface of the vehicle compared with the base model. On the other hand, although pressure is decreased at the far wake with the lower deflector usage, reasonable pressure rise near the rear surface can be seen. This is an inherent result of the increased downwash. More interestingly and more obviously, additional pressure recovery can be observed at the underbody diffuser section of the model with a lower deflector. The usual suspect of the further drag reduction mechanism may be behind this pressure recovery for lower deflector usage. Nevertheless, detailed qualitative analysis can be better to reach more clear indications of the drag reduction influence of the negative slanted deflector plate.

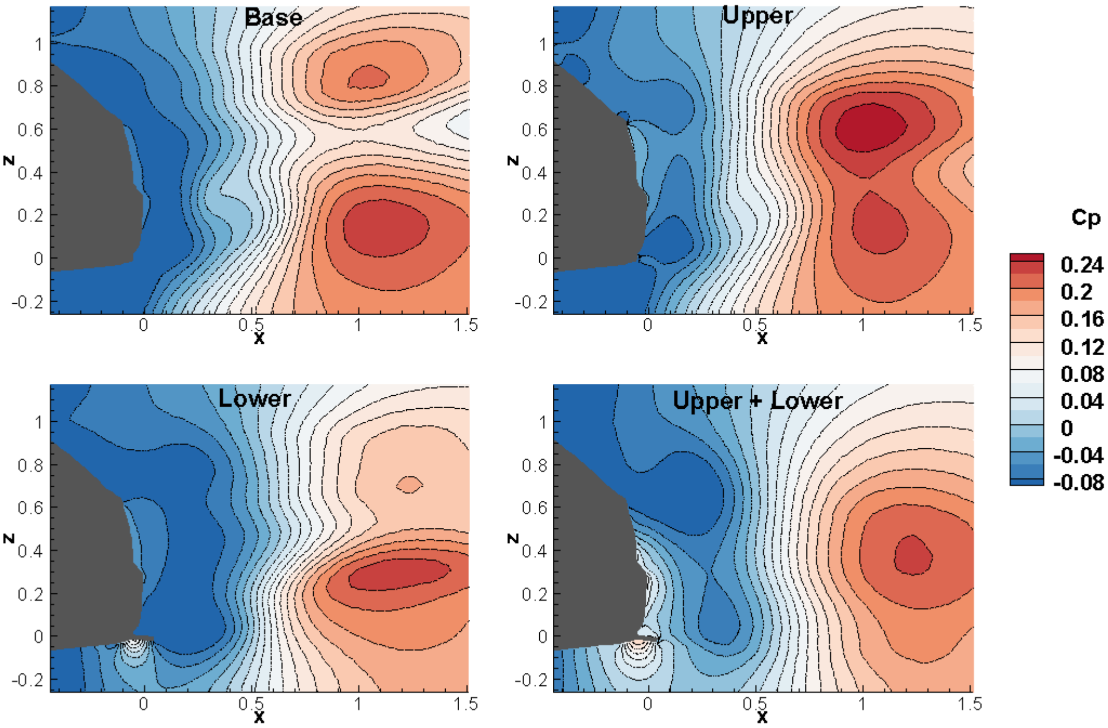

Figure 4.13. Pressure coefficient for estateback without a deflector and with upper, lower, and upper + lower deflector at symmetry plane.

In Figure 4.14 and Figure 4.15, velocity and pressure coefficient contours at the X_1 and X_2 planes are depicted while velocity and pressure coefficient contours at the Z_1, Z_2, and, Z_2 planes are shown in Figure 4.16 and Figure 4.17, respectively. In Figure 4.14 and Figure 4.16, the above-mentioned indications of the stronger downwash can be seen. However, upper and lower deflector usage leads to a lower velocity zone at the X_1 plane which is closer to the rear surface of the vehicle. Nonetheless, at the far region (X_2) and middle section (Z_2) of the wake, contrary results can be observed. On the other hand, it can be seen from Figure 4.14 that the upper deflector leads to pressure recovery both at X_1 and X_2 while the lower deflector reduces pressure at these planes. In addition, it can be said that single deflector usage increases the momentum of flow at the mounted edge while it reduces the airflow on the other side. Hence, reduced momentum cause pressure loss where the deflector is absent in the case of single utilization.

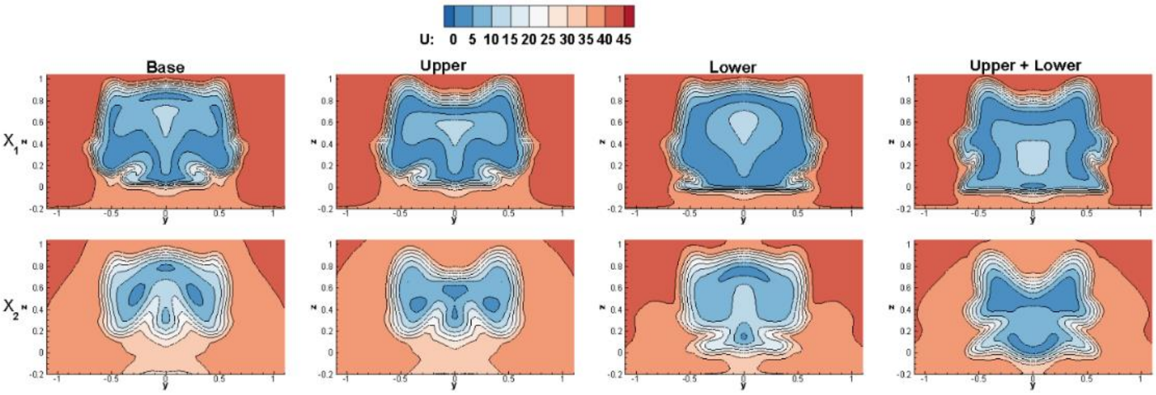

Figure 4.14. Velocity contours at the X_1 and X_2 planes

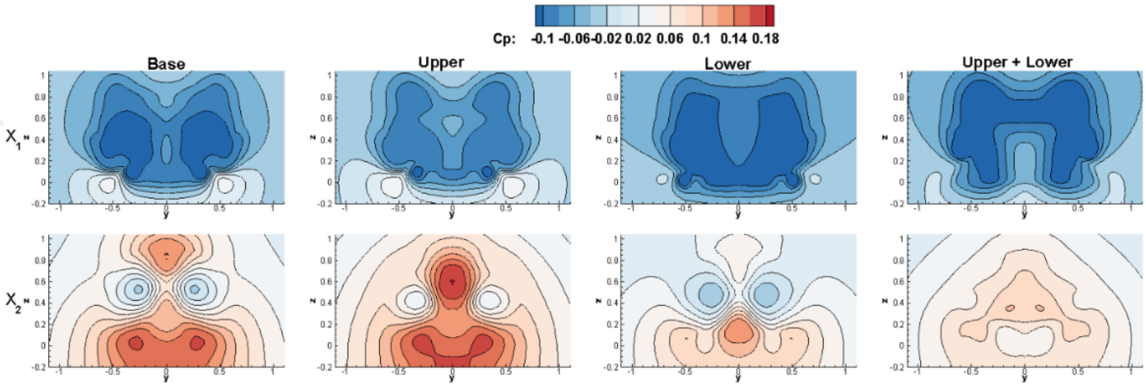

Figure 4.15. Pressure coefficient contours at the X_1 and X_2 planes

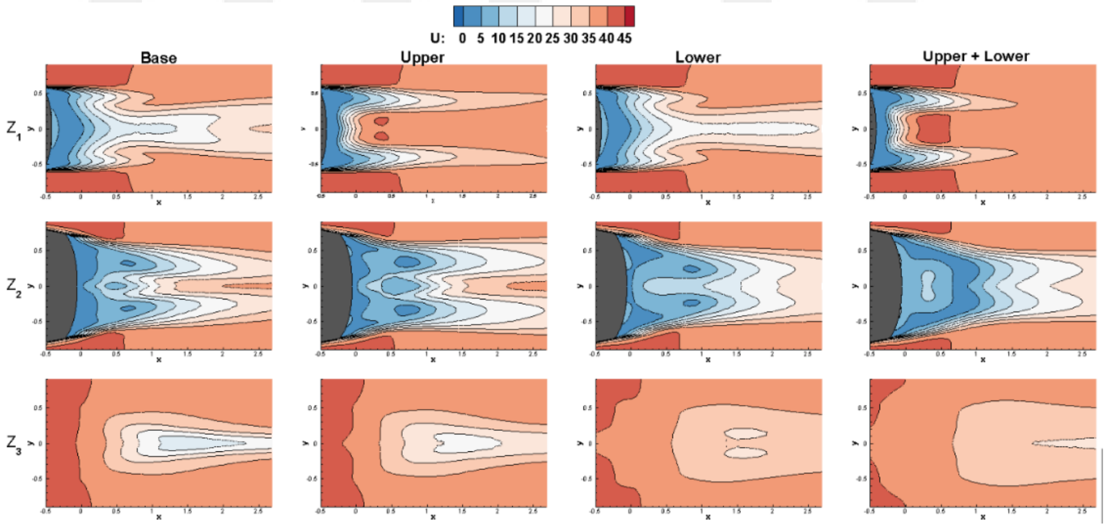

Figure 4.16. Velocity contours at the Z_1 Z_2 and, Z_3 planes

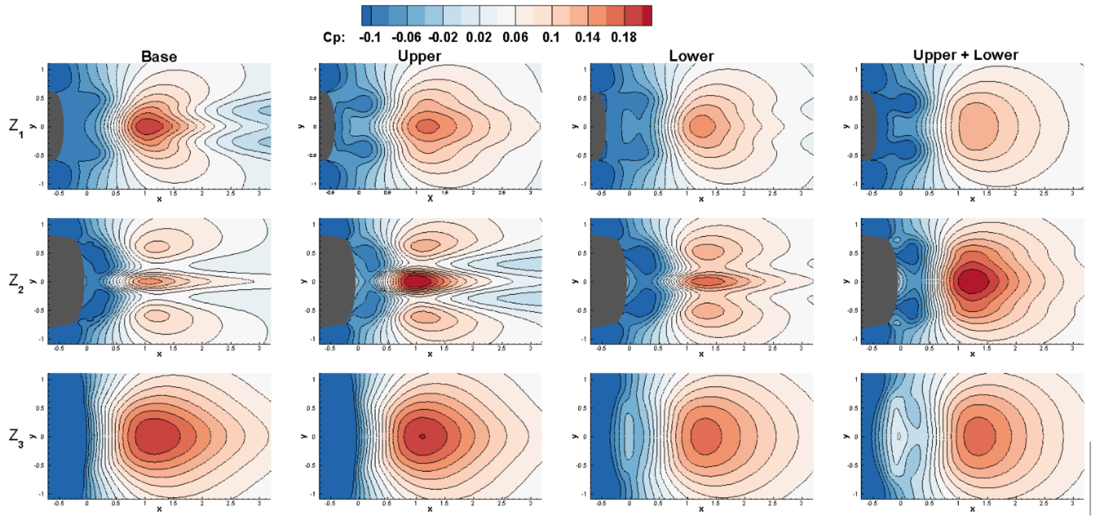

Figure 4.17. Pressure coefficient contours at the Z_1 Z_2 and, Z_3 planes

The clearest demonstration of the drag reduction mechanisms with the deflector usage can be observed in Figures 4.18 and 4.19. Lower deflector usage enhances a remarkable pressure recovery on the slanted diffuser section of the vehicle, hence reducing the drag. On the other hand, this recovery deteriorates the downforce gain of the underbody diffuser hence C_L increases notably. As for Figure 4.19, both upper and lower deflector usage ensures a remarkable pressure recovery on the rear surface of the vehicle, and this can be attributed to the stronger downwash.

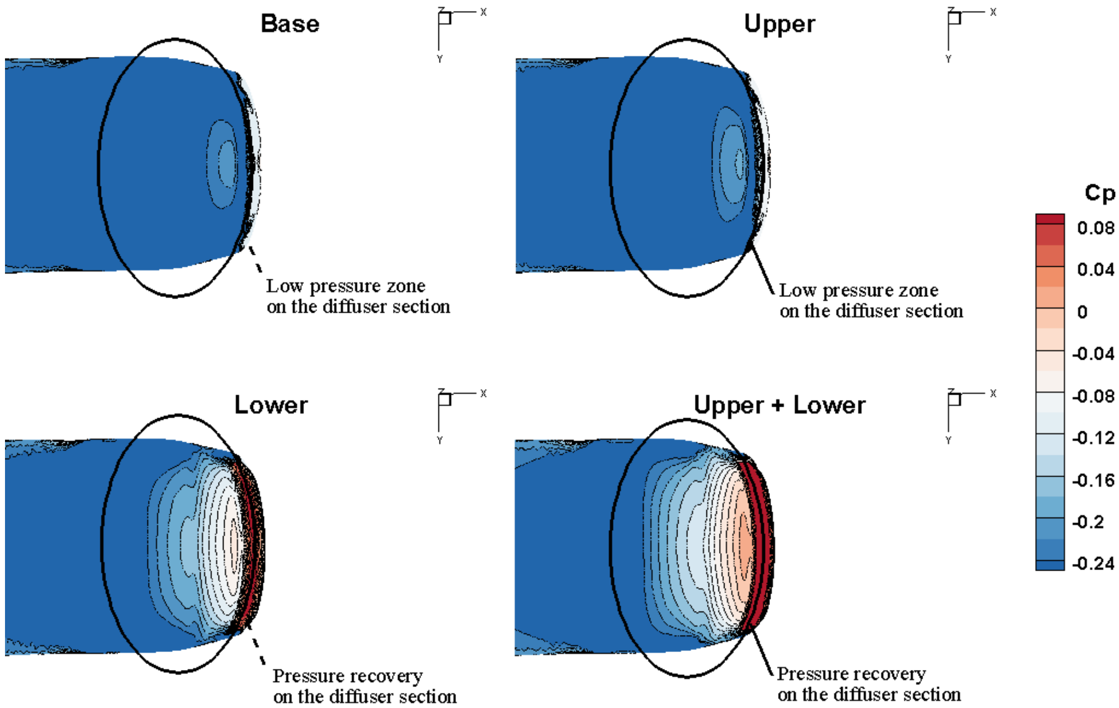

Figure 4.18. Pressure coefficient on underbody surfaces of vehicles

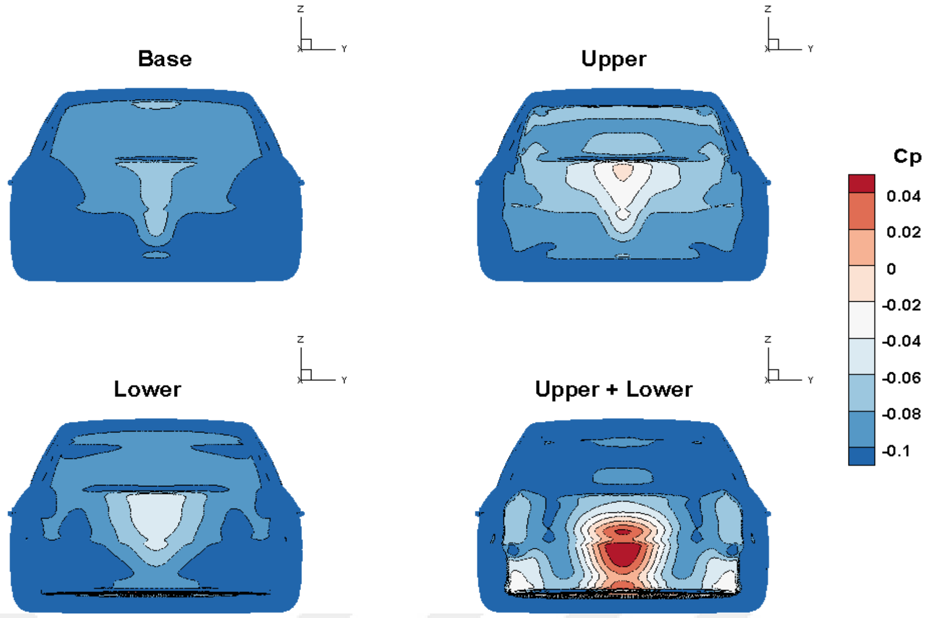

Figure 4.19. Pressure coefficient on rear surfaces of vehicles

4.3. Fastback

4.3.1. Quantitative Analysis for Fastback

Parametric optimization results of upper deflector plates are given in Figure 4.20 for the C_D and C_L output of the fastback model. In the graph, curves of C_D and C_L have concave up and down behavior against the deflector angle. The deflector plate with a 20° slant angle has the minimum C_D output while reducing C_D causes downforce loss in general. Besides, the characteristic of the C_D curve implies a further optimization with a specific deflector angle of the upper plate.

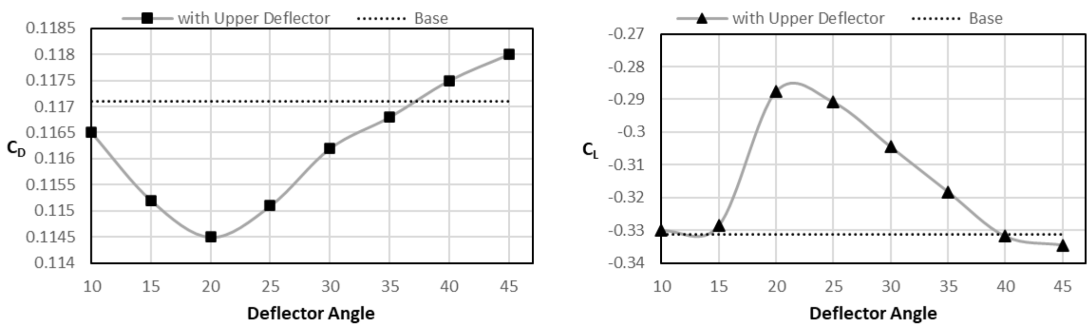

Figure 4.20. Parametric optimization results of fastback model with upper deflector

For the response surface optimization, by the parametric optimization data set of the upper deflector simulations, software suggested that the upper deflector plate with 20.25° could be a candidate point for the global optimum. To validate this, the DrivAer fastback model with an upper deflector plate of 20.25° slant angle was simulated as well as closer values of the slant angles. As a result, the aerodynamic drag coefficient is decreased further with the response surface optimization tool (Figure 4.21). Nevertheless, the usage of the upper deflector as a passive flow control element increases the C_L.

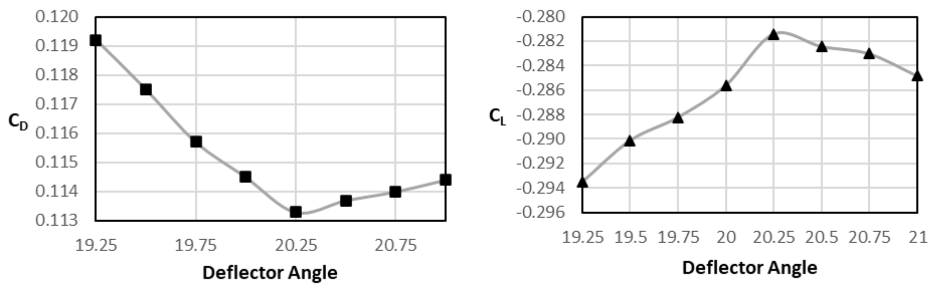

Figure 4.21. Response optimization results of fastback model with upper deflector

As for lower deflector plate usage, the curve of C_D is characterized by concave-up behavior versus deflector angle again (Figure 4.37). However, contrary to the estateback model, minimum aerodynamic drag coefficient output is observed for positive angle value with a lower deflector plate with 5°. C_L output is substantially higher for lower values of deflector plates and reduces gradually with the increment of the deflector angle.

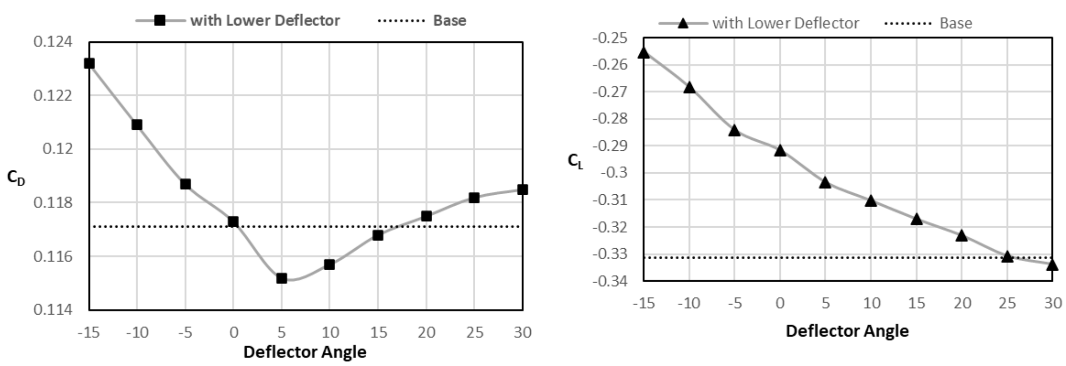

Figure 4.22. Parametric optimization results of fastback model with lower deflector

In the response surface optimization phase of the lower deflector on fastback, it was found that the lower deflector plate with 6.25° is a candidate design point for reaching the global optimum. DrivAer fastback model with a lower deflector plate of 6.25° slant angle was simulated as well as closer values of the slant angles to verify the candidate design of the lower deflector. Consequently, the aerodynamic drag coefficient is decreased remarkably with the response surface optimization tool (Figure 4.23). However, the usage of a lower deflector as a passive flow control element caused downforce reduction.

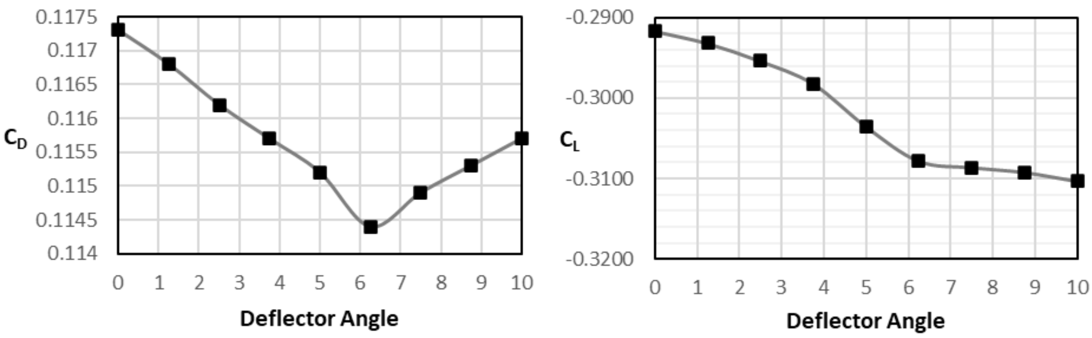

Figure 4.23. Response optimization results of fastback model with lower deflector

In the last stage of the optimization process, adjoint optimizations were carried out to decrease the aerodynamic drag force further. Adjoint optimizations were carried out for upper and lower deflector plates, and the final design was obtained for both passive flow control elements for the fastback model. Consequently, the aerodynamic force outputs from the DrivAer fastback with upper deflector, lower deflector, and combined upper + lower deflector plates were compared with the base model in Figure 4.24. As a result, C_D values are reduced by 2.57%, 1.63%, and 4.82% for the fastback model with upper, lower, and combined upper + lower deflector flow control elements, respectively. C_L results are reduced by 15.05%, 7.11%, and 44.85% for the fastback model devised with lower and combined upper + lower deflectors, respectively.

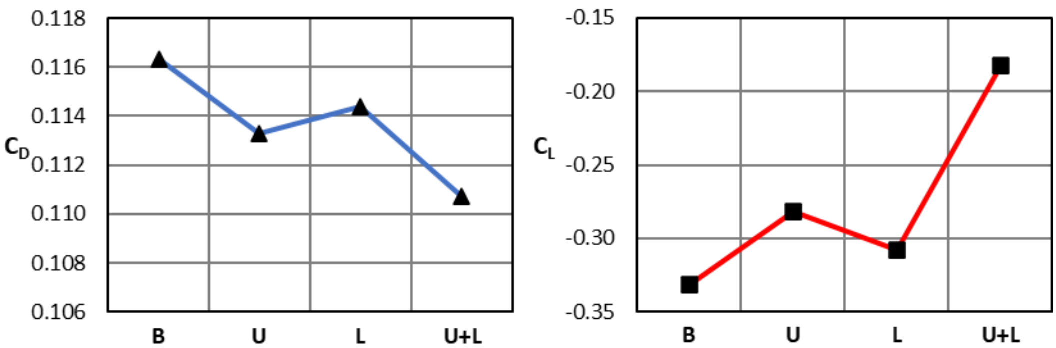

Figure 4.24**.** C_D and C_L results of the fastback without a deflector and with upper, lower, and upper + lower deflector.

To investigate the drag reduction effect of the upper and lower deflector plates of the fastback model, detailed wake statistics are shared in Figures 4.25 and 4.26. Maximum and average TKE values for Region I and Region II is shown in Figure 4.25 while wake area statistic for different fastback configurations is presented in Figure 4.26. It can be seen that wake statistics are remarkably lower for fastback configurations compared with the estateback body type. It is known that fastback and notchback bodies have stronger downwash flow than upwash contrary to estateback models. TKE statistic results are consistent with it.

For the base models, energy dissipation is almost at the same level in the lower and upper regions showing a balance of the upwash and downwash. The upper deflector plate reduces wake area and energy dissipation in the upper region, reasonably. The deflector used under the vehicle, on the other hand, has the opposite effect, reducing the energy loss in the lower region (Region II) while increasing it on the upper region (Region I) due to the loss of momentum. The wake area decreases for both upper and lower deflector usage however, the lower deflector reduces it more.

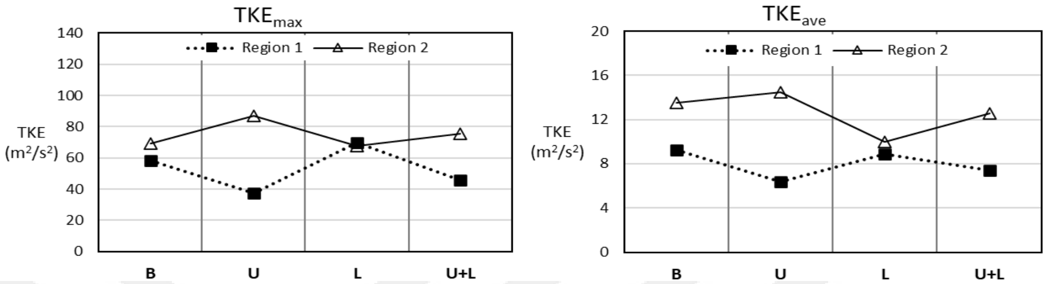

Figure 4.25. The maximum and average TKE values for fastback configurations in Region I and Region II.

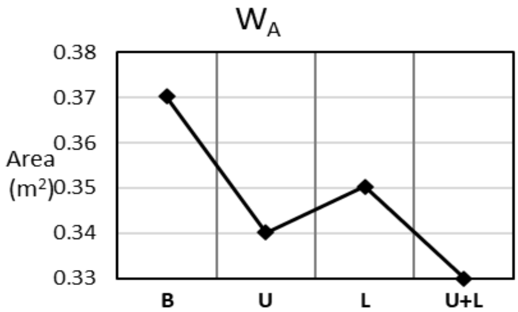

Figure 4.26. Wake area of fastback configurations.

4.3.2. Qualitative Analysis for Fastback

Velocity contours of the fastback configuration without a deflector, with upper, lower, and upper + lower deflectors are shown in Figure 4.27. Upper deflector usage leads to direct downwash more to the wake region hence, velocity recovery is ensured at the wake region close to the vehicle back. It is known that the fastback DrivAer model is characterized by a strong downwash (Avadiar et al., 2019) therefore airflow has lower momentum beneath the fastback vehicles. By the way of the usage upper deflector, a stronger downwash can be seen.

As for the lower deflector usage, the wake region is narrower and comparing with the base model. The usage of a deflector with a positive slant angle leads to enhanced airflow beneath the car. The strength of the upwash is increased while the downwash flow is weakened. As for the lower deflector model, the wake region is wider and larger contrary to the upper deflector devised fastback. The combined usage of the upper and lower deflectors resulted in a more balanced downwash and upwash. Moreover, a significant velocity increment is obvious near the back of the vehicle. These results are consistent with quantitative results in the sense of wake statistics of W_A.

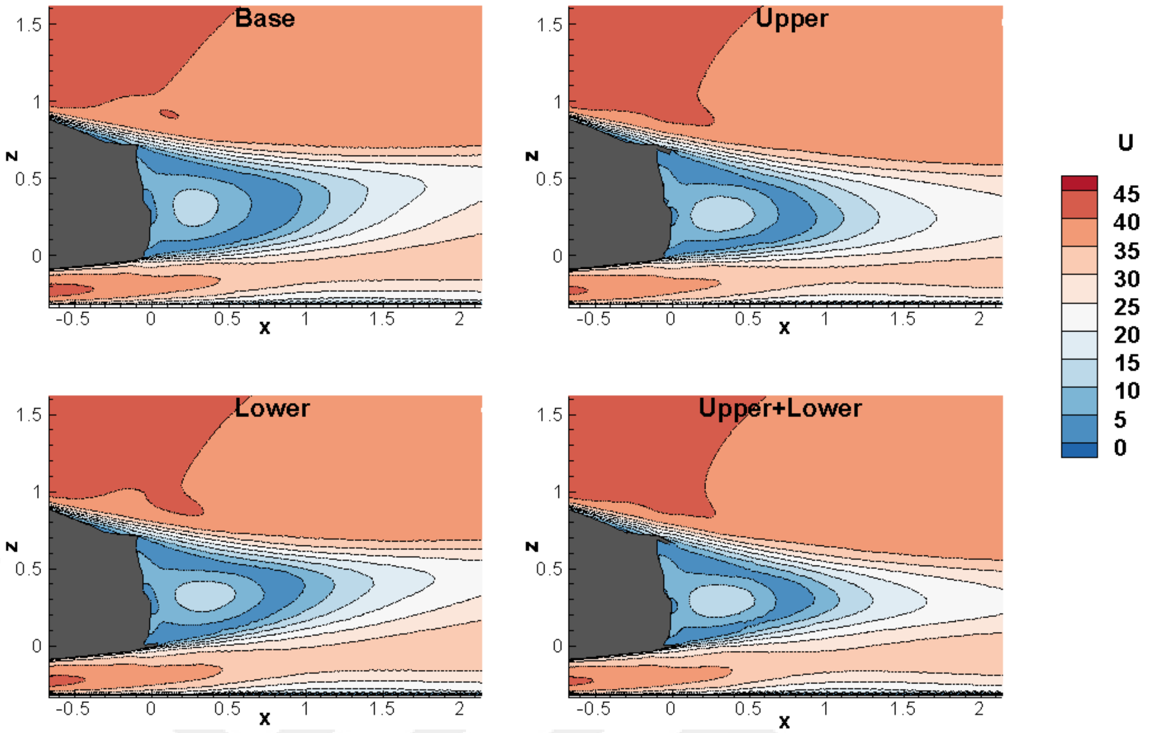

Figure 4.27. Velocity contours for fastback without a deflector and with upper, lower, and upper + lower deflector

Pressure coefficient contours for fastback without a deflector and with upper, lower, and upper + lower deflector at the symmetry plane are shown in Figure 4.28. It can be seen from the contours that upper deflector usage remarkably increases the pressure at the wake and the higher-pressure zone is closer to the rear surface of the vehicle compared with the base model. On the other hand, although pressure is decreased at the near wake region with the lower deflector usage, a slight pressure recovery can be observed at the underbody diffuser section of the model with the lower deflector. The main drag-reduction effect of the lower deflector will be discussed and illustrated in the following sections. With the simultaneous usage of the deflectors, substantial pressure rise is observed at the far wake. However, no apparent indicator of the drag reduction can be seen except for minor scaled variances between the base and upper + lower models.

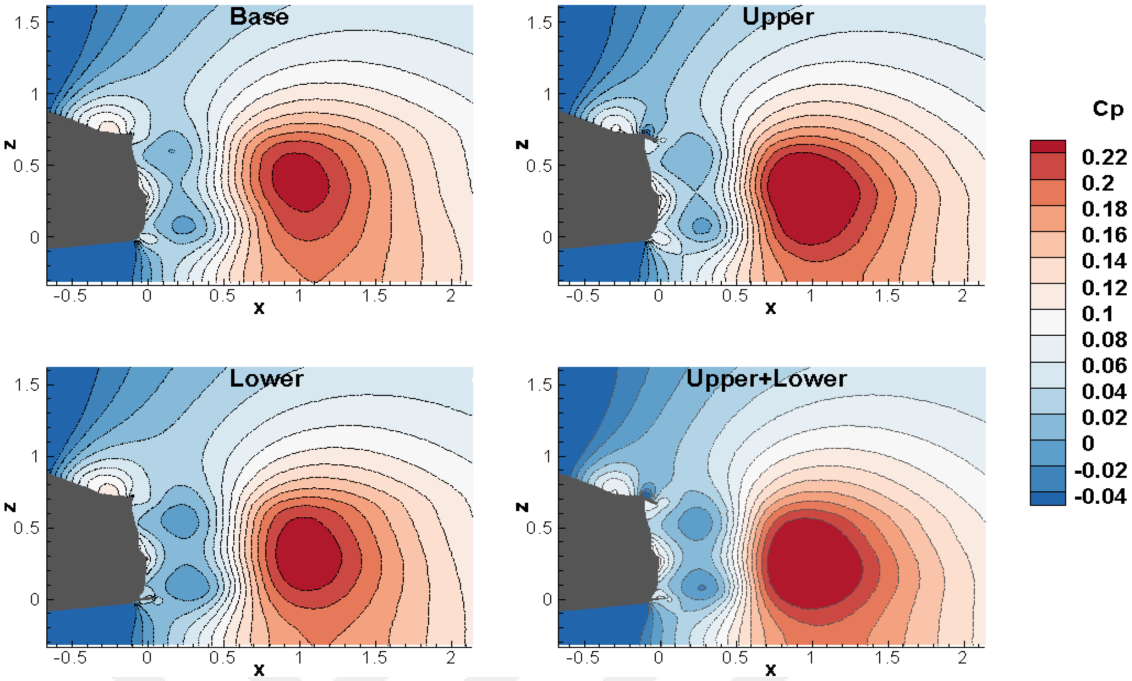

Figure 4.28. Pressure coefficient contours for fastback without a deflector and with upper, lower, and upper + lower deflector at symmetry plane.

In Figure 4.29 and Figure 4.30, velocity and pressure coefficient contours at the X_1 and X_2 planes are depicted while velocity and pressure coefficient contours at the Z_1, $Z_{2,}$ and, Z_2 planes are shown in Figure 4.31 and Figure 4.32, respectively. In Figure 4.29 and Figure 4.31, the above-mentioned indications of the stronger downwash can be seen at the Z_1 and upper regions of X_1 and X_2. Furthermore, upper and lower deflector usage ensures velocity recovery at the X_1 and X_2 planes. Besides the middle section (Z_2) of wake, wake elongation is satisfied by both upper and lower deflector plates. On the other hand, it can be seen from Figure 4.31 that the upper deflector enables a pressure recovery both at X_1 and X_2 while the lower deflector reduces pressure at these planes. In addition, it can be said that single deflector usage increases the momentum of flow at the applied edge while it reduces the airflow on the other side. Hence, reduced momentum cause a loss of pressure where a deflector is absent in the case of single utilization.

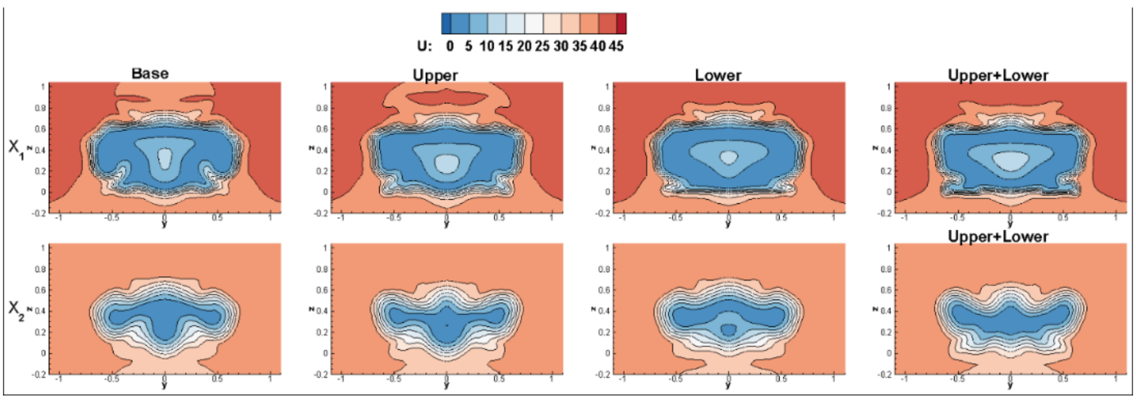

Figure 4.29.Velocity contours at the X_1 and X_2 planes

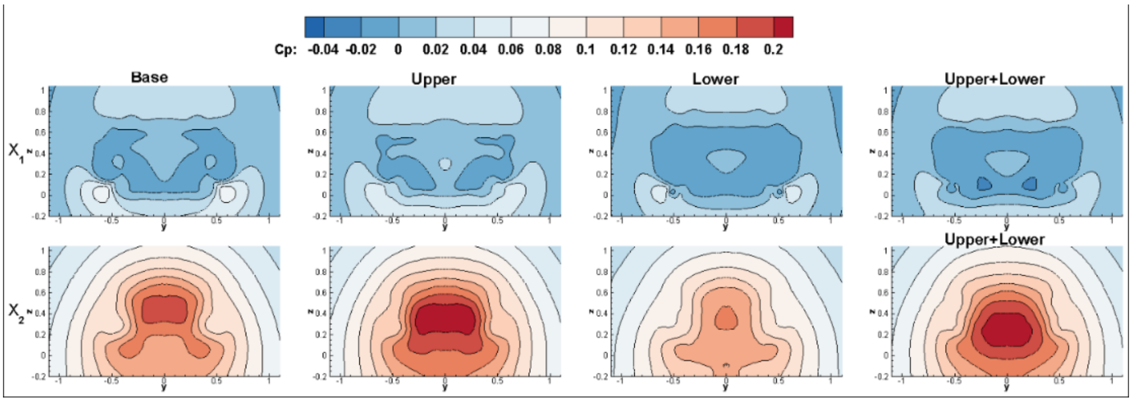

Figure 4.30. Pressure coefficient contours at the X_1 and X_2 planes

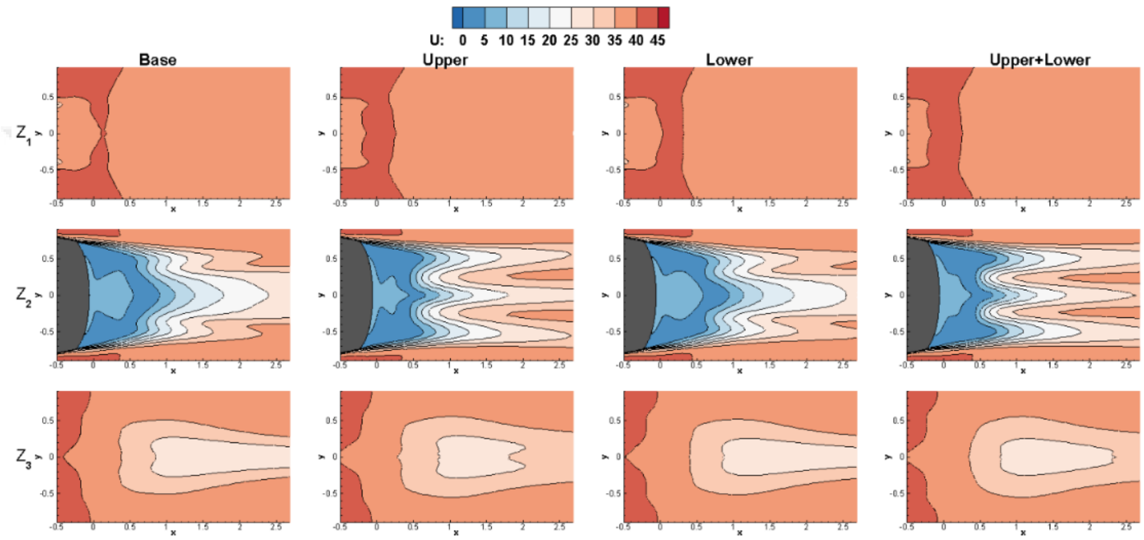

Figure 4.31. Velocity contours at the Z_1 Z_2 and, Z_3 planes

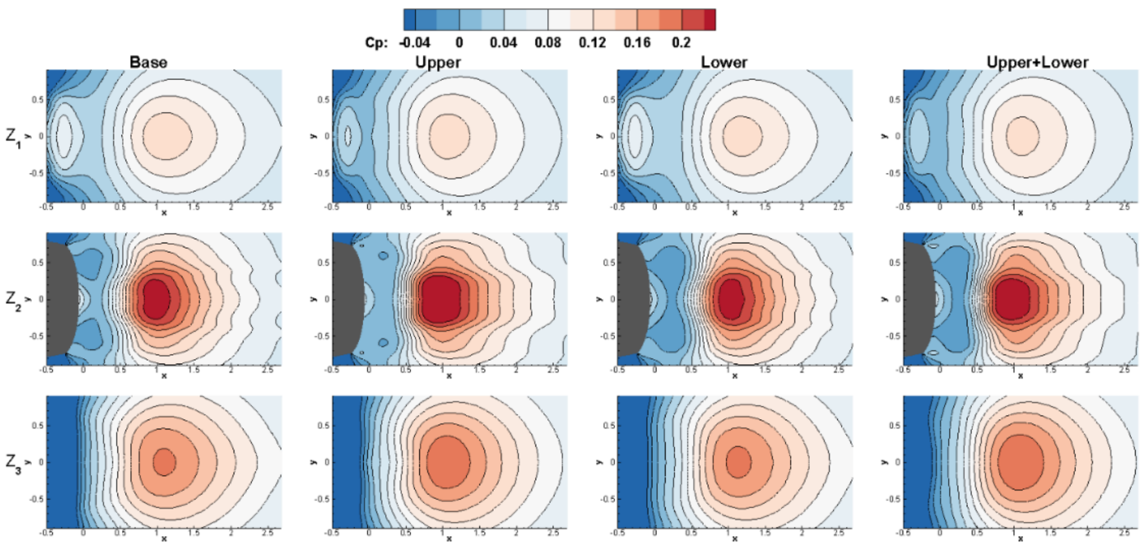

Figure 4.32. Pressure coefficient contours at the Z_1 Z_2 and, Z_3 planes

The most obvious effect of the deflector usage on drag reduction can be found in Figures 4.32 and 4.33. Lower deflector usage enhances a remarkable pressure recovery on the slanted diffuser section of the vehicle and positive inclined deflector surface; hence it reduces the drag. On the other hand, this recovery decreases the downforce gain on underbody surfaces, hence C_L increases significantly. As for Figure 4.33, upper deflector usage ensures a remarkable pressure recovery on the middle-rear surface of the vehicle, and this can be attributed to the stronger downwash. An interesting result is that additional pressure is recovered on the underbody surface of the vehicle by the upper deflector usage since upwash intensity and underneath flow are reduced which led flow detachment and stall on the underbody diffuser. This stall-like situation is explained by (Guerrero et al., 2022) such that a momentum deficit or too steep diffuser angle results in a drag crisis. However, the lower deflector provides a pressure recovery in a wider area of rear surfaces, it may be a result of enhanced side-flows.

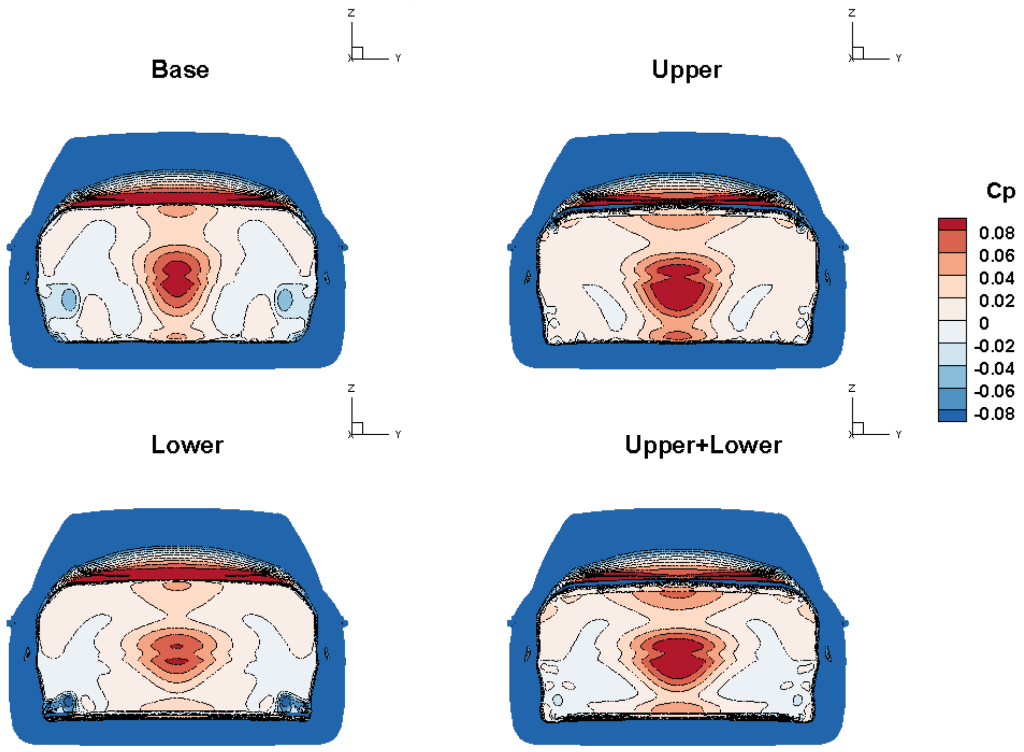

Figure 4.33. Pressure coefficient on underbody surfaces of vehicles

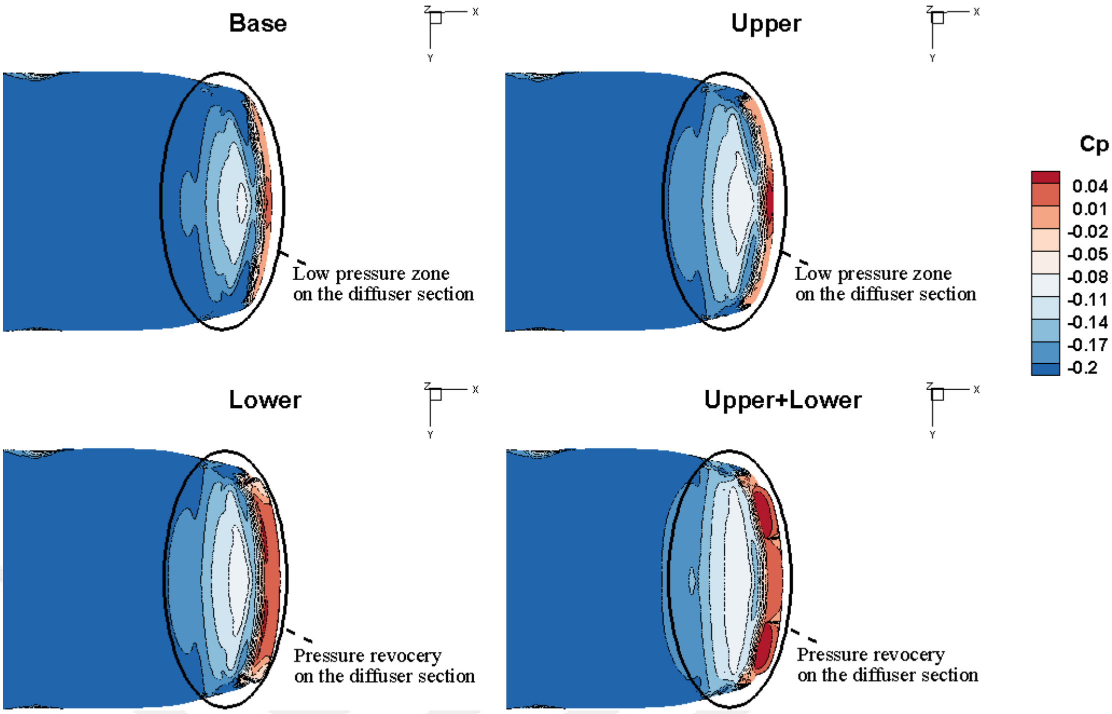

Figure 4.34. Pressure coefficient on rear surfaces of vehicles

4.4. Notchback

4.4.1. Quantitative Analysis for Notchback

C_D and C_L results of Parametric optimization for upper deflector plates are given in Figure 4.20 for the notchback model. It can be seen from the graph that the curves of C_D and C_L have similar trends as estateback and fastback DrivAer models. Minimum C_D output is observed with a deflector plate of 20° slant angle. However, when C_D reduction is acquired downforce loss occurs. Besides, curve characteristics are promising for potential further optimization for aerodynamic drag and the global minimum was investigated further to find the optimum deflector angle of the upper plate.

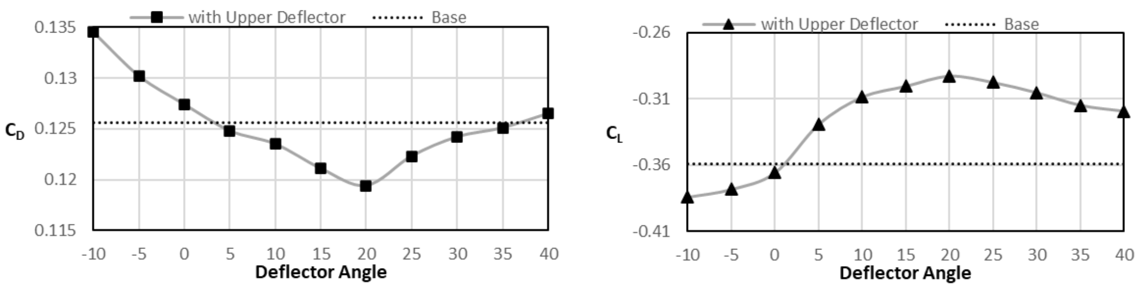

Figure 4.35. Parametric optimization results of notchback model with upper deflector

In response surface optimization process, the software predicts that the upper deflector plate with 20.75° could be a candidate point for the global optimum by using parametric optimization data. To validate the result, the DrivAer notchback model with an upper deflector plate of 20.75° slant angle was simulated as well as closer values of the slant angles. As a result, C_D is reduced further with the response surface optimization tool (Figure 4.36). Nevertheless, it can be said that the using a deflector as a passive flow control element increases the C_L.

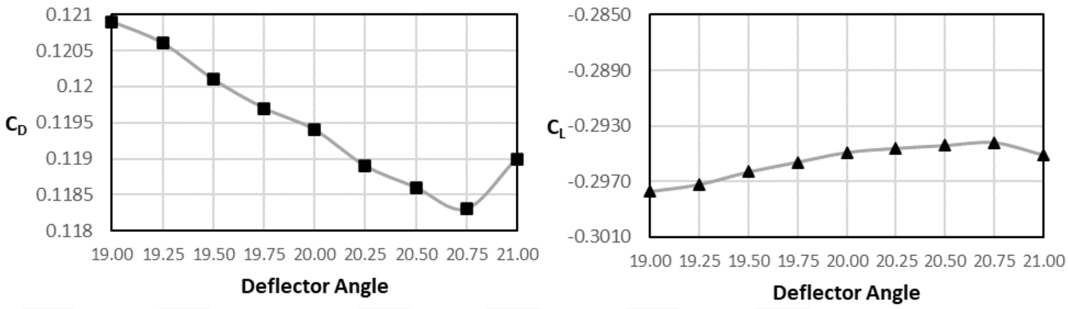

Figure 4.36. Response surface optimization results of notchback model with upper deflector

The curve of C_D is characterized by concave up behavior versus deflector angle again with lower deflector plate usage (Figure 4.37). However, contrary to the estateback model and the same as the fastback model, the minimum aerodynamic drag coefficient is obtained for a positive angle value with a lower deflector plate with 10°. C_L output is substantially higher for lower values of deflector plates and reduces gradually with the increment of the deflector angle.

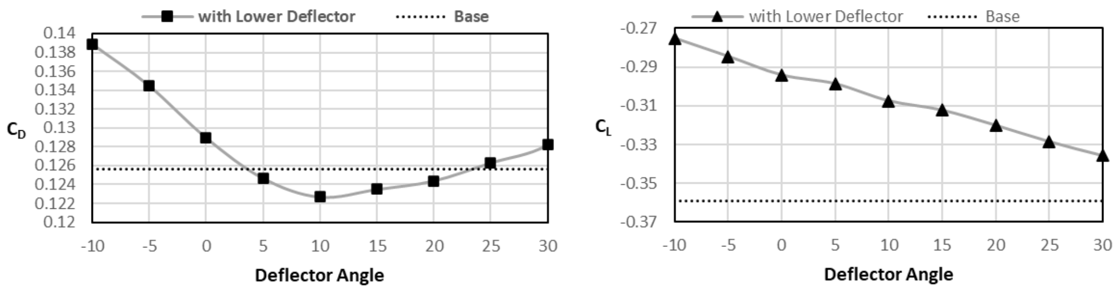

Figure 4.37. Parametric optimization results of notchback model with lower deflector

In the response surface optimization stage, a lower deflector plate with an 8° slant angle was predicted as a candidate design point for the global optimum. DrivAer notchback model with a lower deflector plate of 8° slant angle was simulated as well as closer values of the slant angles to verify response surface suggestion. Consequently, the aerodynamic drag coefficient is decreased slightly with the response surface optimization tool (Figure 4.38). However, the use of a lower deflector as a passive flow control element caused downforce reduction as same as other deflector plates.

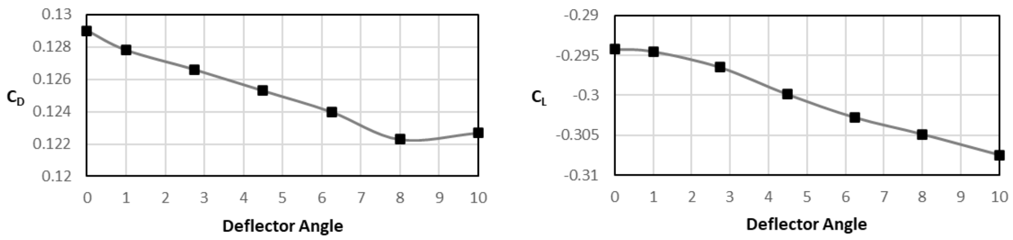

Figure 4.38. Response surface optimization results of notchback model with lower deflector

In the last stage of the optimization process, adjoint optimization simulations were conducted to minimize the aerodynamic drag force further. Adjoint simulations were carried out for combined upper and lower deflector plates at the same time, and the final design was obtained for both passive flow control elements. Consequently, the aerodynamic force output from the DrivAer fastback with upper deflector, lower deflector, and combined upper + lower deflector plates was compared with the base model in Figure 4.39. As a result, C_D values are reduced by 1.63%, and 4.82% for the fastback model equipped with a lower deflector and combined upper + lower deflectors, respectively. However, C_L output decreased by 15.05%, 7.11%, and 44.85% for the fastback model equipped with a lower deflector and combined upper + lower deflectors, respectively.

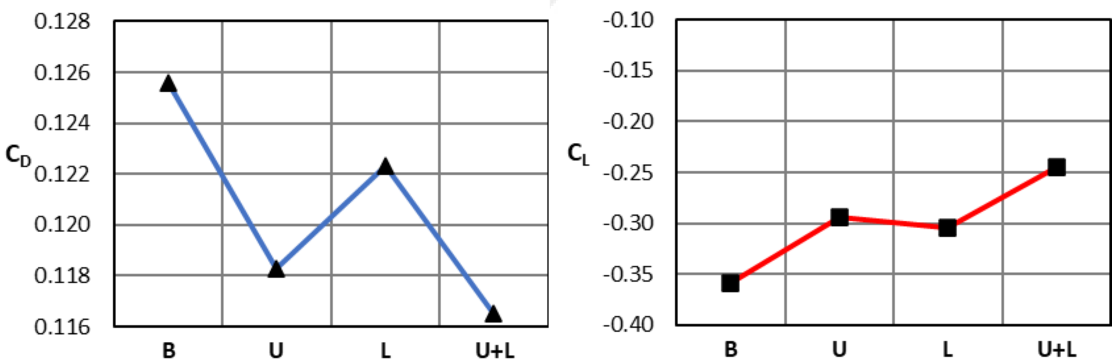

Figure 4.39. C_D and C_L results of the notchback without a deflector and with upper, lower, and upper + lower deflector.

Detailed wake statistics are shared in Figures 4.25 and 4.26 to investigate the drag reduction effect of the upper and lower deflector plates on the fastback model. Maximum and average TKE values for Region I and Region II are shown in Figure 4.25 while the wake area for different configurations of notchback models is presented in Figure 4.26. Although the notchback model has a more balanced upwash and downwash flow compared with estateback, the notchback model has a stronger downwash flow. By the usage of the upper deflector plate, downwash flow and momentum of it from the upper region are increased, hence average and maximum TKE is minimized in the upper region, and wake area statistics are reduced reasonably, on the other hand, decreased upwash leads to a rise in TKE statistics in Region II. However, lower deflector usage caused a more balanced energy dissipation in the upper and lower regions of the wake flow while the wake area is smaller compared with the base configuration of the fastback. Because of the weaker upwash, deflection of the underbody flow does not reduce wake size as much as upper deflection. The combined usage of deflector plates with optimum design ensures further reduction in wake area and more balanced upwash and downwash compared to single usage of them.

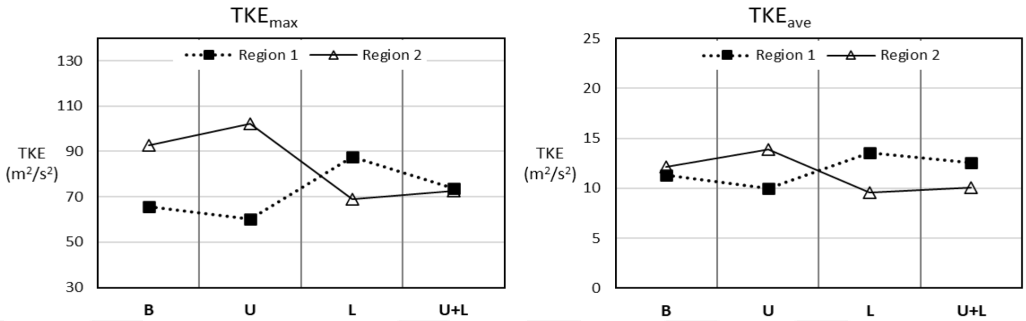

Figure 4.40. The maximum and average TKE values for fastback configurations in Region I and Region II.

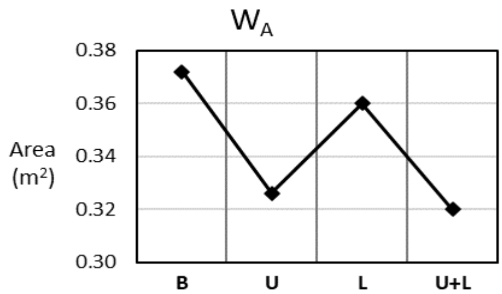

Figure 4.41. Wake area for notchback configurations.

4.4.2. Qualitative Analysis for Notchback

Velocity contours for notchback without a deflector and with upper, lower, and upper + lower deflectors are presented in Figure 4.42. It can be said that the base notchback model has a slightly wider low-velocity zone than the base fastback model. The usage of the upper deflector directs downwash flow to the wake region, and a narrower low-velocity region is ensured compared with the base model. It is known that the notchback DrivAer model is characterized by a strong downwash (Avadiar et al., 2019) therefore airflow has lower momentum beneath the notchback vehicles. By the way of the usage of an upper deflector, a stronger downwash is sustained. As for the lower deflector model, the wake region is wider and larger contrary to the upper deflector devised notchback. However, the usage of a lower deflector with a positive slant angle confines airflow beneath the car slightly. It seems less interaction leads to remarkable velocity recovery at the wake, thereby lower energy dissipation results from the previous part can be attributed to it. The combined usage of the upper and lower deflectors resulted in a stronger downwash and the weakest upwash among all of them. These results are consistent with quantitative results in the sense of wake statistics of W_A.

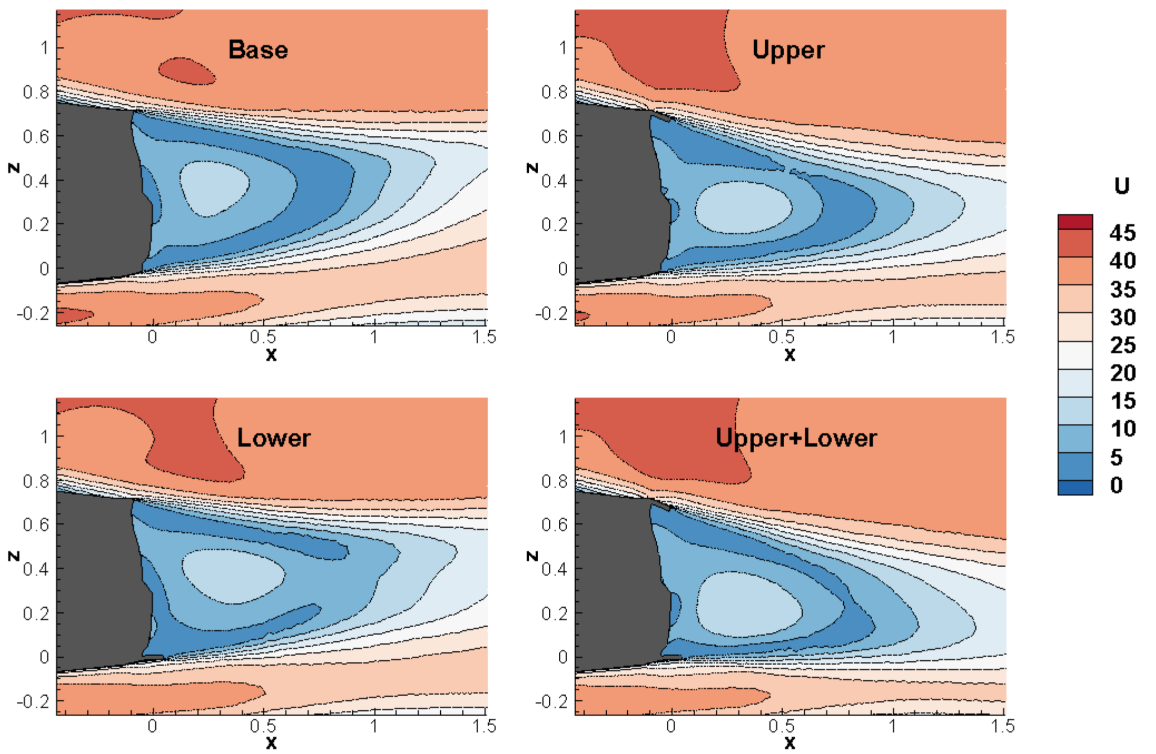

Figure 4.42. Velocity contours for estateback without a deflector and with upper, lower, and upper + lower deflector at symmetry plane.

Pressure coefficient contours for notchback without a deflector and with upper, lower, and upper + lower deflector at the symmetry plane are shown in Figure 4.43. Pressure coefficient contours show that upper deflector usage significantly increases the pressure at the wake and a higher-pressure zone is ensured closer to the rear surface of the vehicle compared with the base model. On the other hand, although pressure is decreased at the far wake with the lower deflector usage, no significant pressure recovery near the rear surface can be seen. However, there is a pressure rise on the underbody diffuser section. The drag reduction mechanism can result from this pressure recovery for lower deflector usage. Nevertheless, further qualitative analysis on surface pressures can be better to reach more clear indicators of the drag reduction influence of the lower deflector plate for the notchback model.

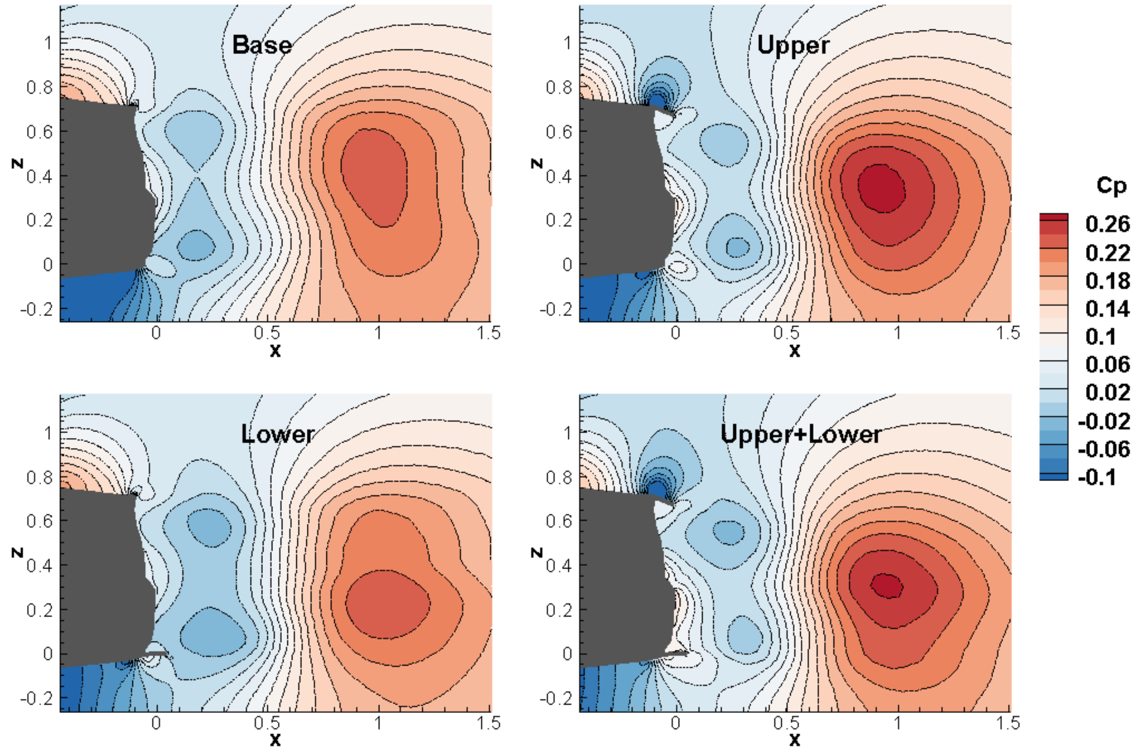

Figure 4.43. Pressure coefficient contours for fastback without a deflector and with upper, lower, and upper + lower deflector at symmetry plane.

Z_1, Z_2, and, Z_2 planes are shown in Figure 4.44, and Figure 4.45, respectively. In Figure 4.46 and Figure 4.47, stronger upwash can be seen in the upper regions for the upper deflector plate. Moreover, upper deflector usage leads to a higher velocity zone at the X_1 plane which is closer to the rear surface of the vehicle. Besides, at the far region (X_2) and middle section (Z_2) of the wake, parallel results can be observed. As for the lower deflector, velocity recovery is more obvious on the far wake. Wake elongation can be observed for the lower deflector model at Z_2.

It can be seen from Figure 4.44 that the upper deflector leads to pressure recovery both at X_1 and X_2 while the lower deflector reduces pressure at these planes. For the upper + lower model, a higher pressure zone is observed at X_1 while the X_2 plane is characterized by a lower pressure zone compared with the base notchback DrivAer model.

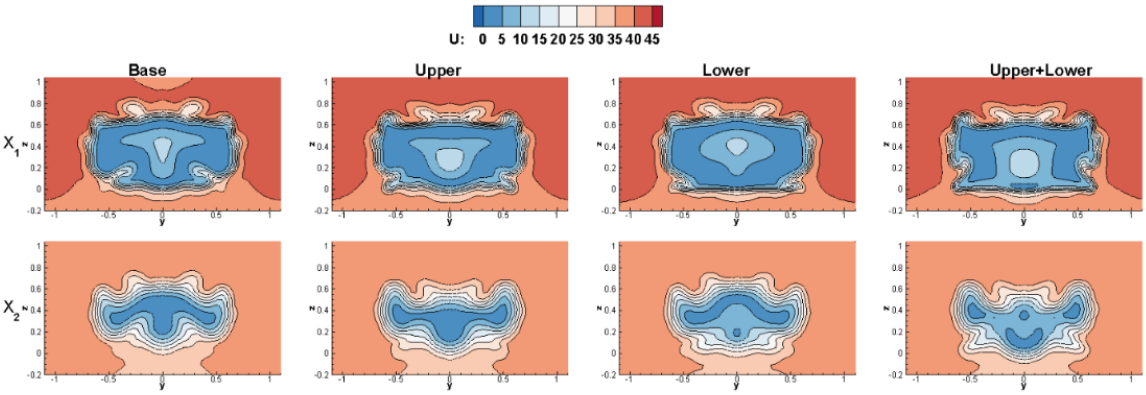

Figure 4.44. Velocity contours at the X_1 and X_2 planes

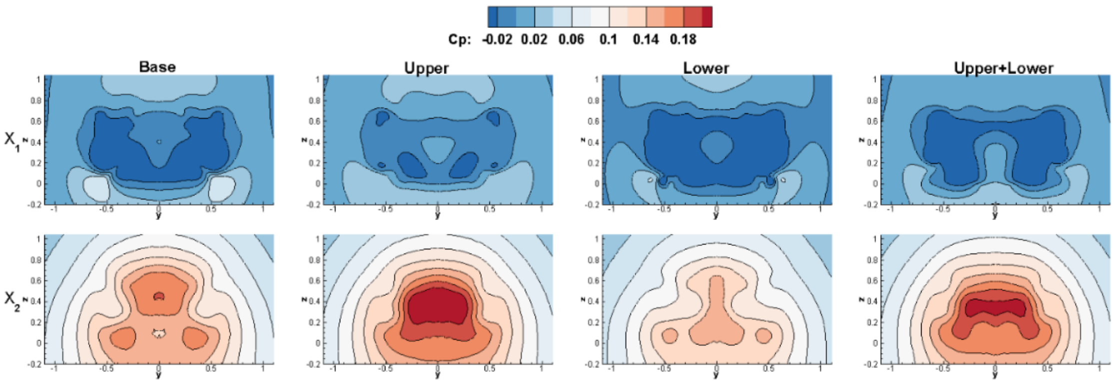

Figure 4.45. Pressure coefficient contours at the X_1 and X_2 planes

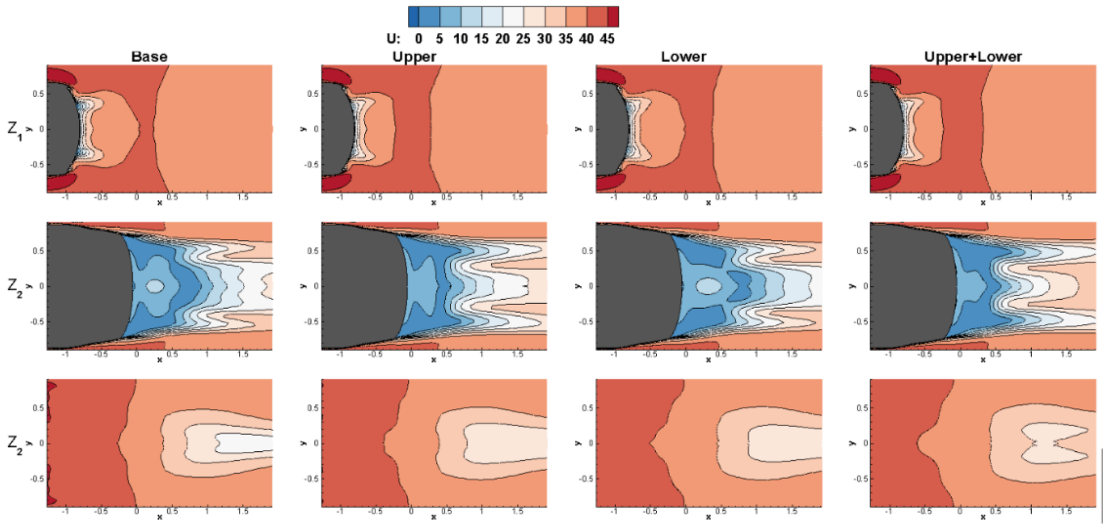

Figure 4.46. Velocity contours at the Z_1 Z_2 and, Z_3 planes

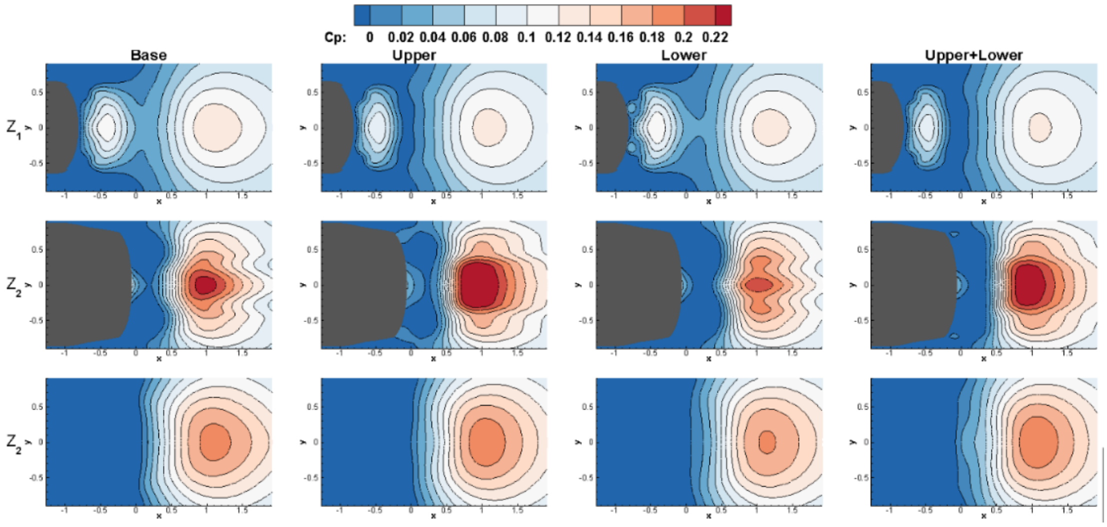

Figure 4.47. Pressure coefficient contours at the Z_1 Z_2 and, Z_3 planes

The most apparent representation of the drag reduction effects of the deflector usage as a flow control element on notchback can be observed in Figures 4.48 and 4.49. Upper deflector usage enhances a remarkable pressure recovery on the rear surface. Lower deflector usage provides this pressure gain on the slanted diffuser section of the vehicle and deflector underbody surface. These results show where the aerodynamic drag reduces. On the other hand, pressure recovery on the diffuser section deteriorates the downforce gain of the underbody diffuser hence C_L increases notably as stated quantitative analysis section. Moreover, combined usage of upper and lower deflector usage resulted in the most apparent pressure recovery on the rear surface of the vehicle.

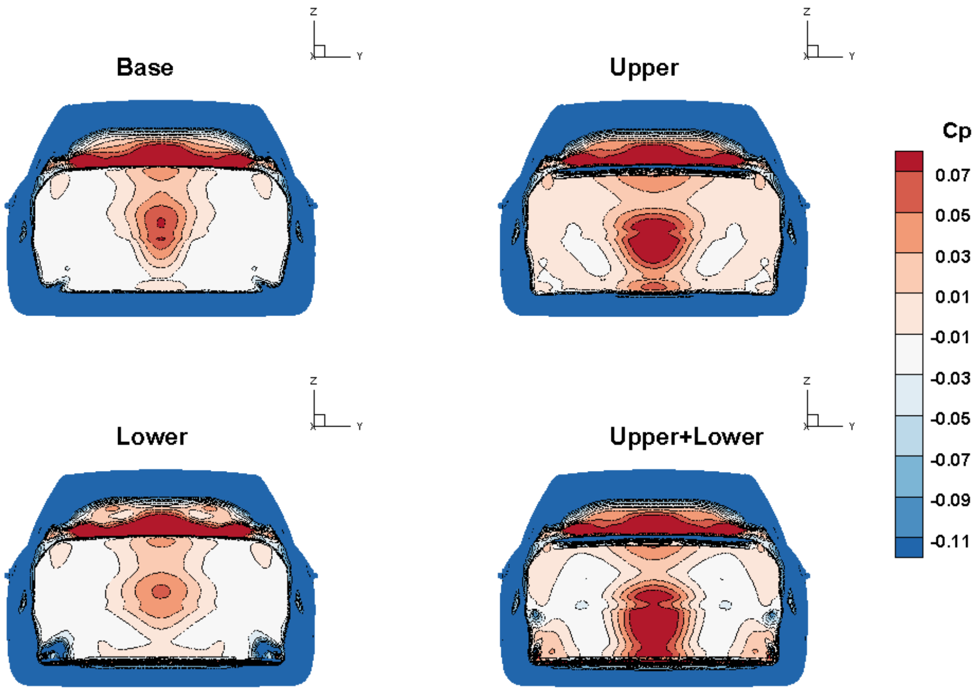

Figure 4.48. Pressure coefficient on underbody surfaces of vehicles

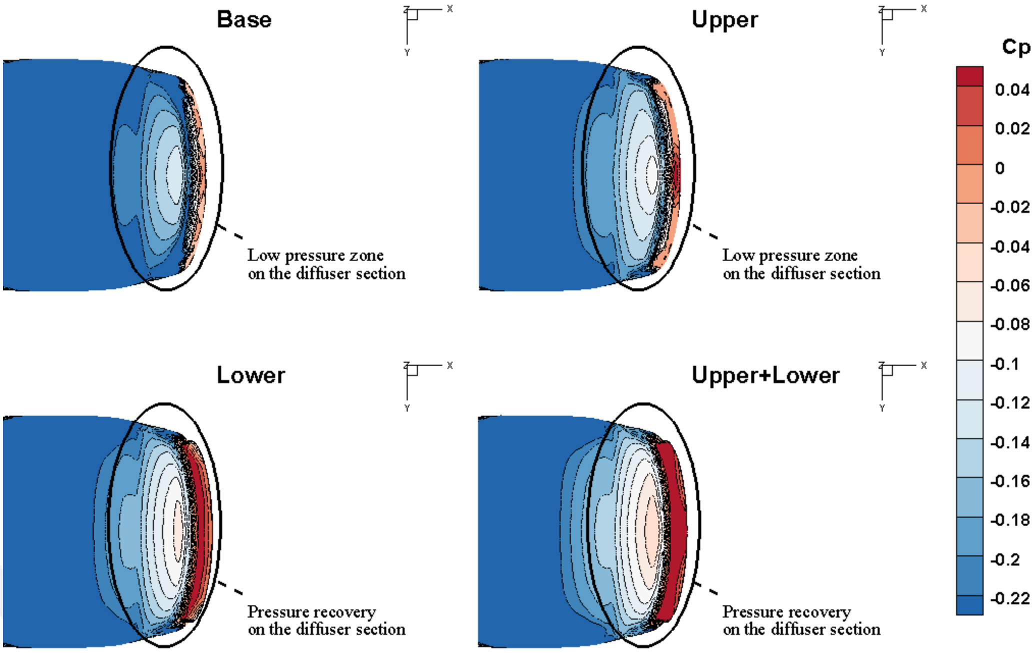

Figure 4.49. Pressure coefficient on underbody surfaces of vehicles

4.5. Results of Efficiency Analysis

In this section, the potential of the flow control methods is evaluated in terms of the resultant efficiencies. The calculations of this paper were performed by using power and fuel-saving rate formulas. Details of the calculation methods can be found in Section 3.4. Potential fuel (on the left) and power saving (on the right) of the flow control applied models are presented in Figure 4.50. It can be seen that the highest potential of the deflector is prominent for estateback models. Single usage of lower and upper deflectors on estateback can enhance fuel efficiency by 3.84% and 5.84% and power saving by 7.03% and 9.57% respectively. However, simultaneous utilization of both upper and lower deflectors can boost fuel and power saving improvement by up to 11.15% and 19.95%, respectively. In this regard, flow control elements have more potential for EVs.

The power and fuel-saving potential of the deflector are comparably lower for the notchback DrivAer closed-body model. Numerically, the power and fuel-saving rate of the simultaneous usage of the upper and lower deflector on the notchback is 8.04% and 3.84%, respectively. As for the fastback configuration, upper, lower, and upper + lower configured models can reduce fuel consumption up to 1.31%, 0.83%, and 2.47%; power consumption up to 2.83%, 1.81%, and 5.21%, respectively. The lower potential of deflector flow control elements on notchback and fastback models can be attributed to their more aerodynamic forms and streamlined shape as has been already explained in the qualitative assessment sections. Hence, it is known that they have significantly lower pressure drag to recover sourced by rear wake compared to the estateback model which has a more bluff shape.

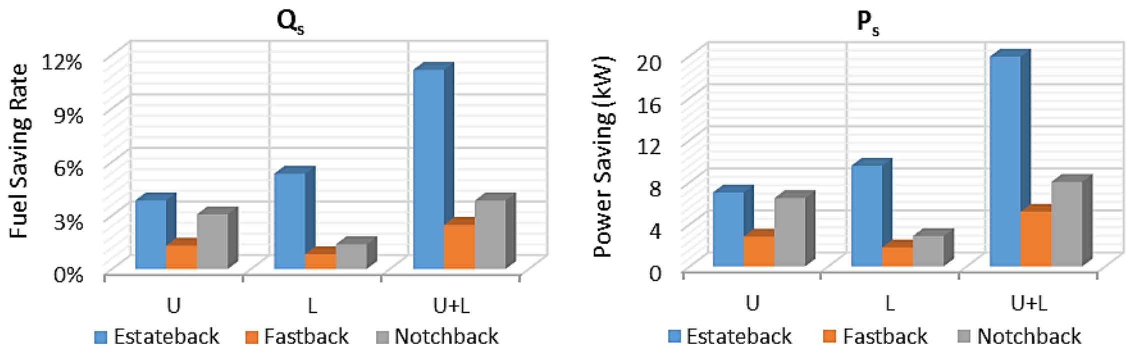

Figure 4.50. Efficiency analysis by fuel saving rate (left) and power saving (right) of flow control elements.

To state the difference in the effect of deflector plates on DrivAer configurations numerically, TKE and wake statistics are shown in Table 4.4 for the base model. Identifications of Region I, Region II, and the wake region can be found in Figure 4.1 and Figure 4.3.

It can be seen that the estateback configuration has a wider wake region compared with other models and is characterized by upwash. On the other hand, fastback and notchback base models have a narrower wake and more balanced upwash and downwash flow characteristics. However, the narrowest and most balanced flow characteristics can be seen in the fastback model. This explains how the fastback rear-ended model has the most aerodynamic model among them.

Table 4.4. TKE and wake area statistics for the base model of DrivAer closed body types

	Region 1		**Region 2**		**Wake Area**
	TKE_{max} (m^2s^2)	**TKE_{ave} (m^2s^2)**	**TKE_{max} (m^2s^2)**	**TKE_{ave} (m^2s^2)**	**W_A (m^2)**
Estateback	140.9	17.8	49.5	9.4	0.567
Fastback	58.4	9.2	69.2	13.6	0.369
Notchback	92.6	11.4	65.5	12.2	0.372

Consequently, it can be said that lower, upper, and upper +lower deflectors have a great effect on improving aerodynamic performance in terms of efficiency. However, they have been applied to relatively more abstract model since the models used in this work does not involve wheel, wheelhouses, or mirrors that lead to significant aerodynamic drag sources and affect flow structures, especially on wake. Moreover, whole investigations were conducted numerically. In this sense, experimental validation of the deflectors on wheels and mirrors including DrivAer models can provide more realistic insight into these flow control elements.

5. CONCLUSIONS

In this study, an optimization framework is performed for the aerodynamic shape optimization of a realistic generic model's upper and lower deflectors. The slant angle of the upper and lower deflector plates is optimized step-by-step via Parametric, Response Surface, and Adjoint optimization methods of Ansys Fluent's CFD solver. The outcomes from this study can be summarized as follows:

- Starting optimization procedure with parametric and response surface before the adjoint solver can reduce GBO design iterations and global optimum can be reached step-by-step without facing negative cell issue.
- To obtain lower aerodynamic drag, the optimum upper deflector plate angles are 23.73°, 20.25°, and 20.75°, while optimum lower deflector angles are -8°, 6.25°, and 8° for estateback, fastback, and notchback models, respectively.
- Compared to the base model, C_D values are reduced by 62.4, 25.7, and 58.1 while C_L values are increased by 39.1, 49.9, and 64.9 counts with optimum design of the upper deflector for estateback, fastback, and notchback models, respectively.
- Compared with the base model, C_D values are decreased by 86.2, 16.3, and 26.3 while C_L values are increased by 137.6, 23.5, and 52.2 counts with optimum design of the lower deflector for estateback, fastback, and notchback models, respectively.
- Compared to the base model, C_D values are reduced by 179, 48.2, and 72.5 while C_L values are increased by 239.6, 148.6, and 114.7 counts with simultaneous usage of the upper and lower deflectors for estateback, fastback, and notchback models, respectively.
- Detailed qualitative analysis is shown that deflectors have different drag reduction mechanisms at the wake for estateback, fastback, and notchback models.
- The upper deflector reduces wake statistics and attains pressure recovery at the back surface by improved downwash for all models.
- The lower deflector restricts airflow beneath the car for estateback. Hereby, this provides pressure recovery at the slanted diffuser section by blocking its diffuser functionality while the restricted airflow is deflected to the upperbody and results in pressure recovery at the rear surface by improved upwash, although it increases the wake region.
- For the fastback and notchback models, the drag reduction mechanism of the lower deflector lies behind enhanced upwash beneath the car.
- Combined usage of the upper and lower deflectors at the rear side edge of the DrivAer is more beneficial to minimize the aerodynamic drag source.

- The upper and lower deflector usage does not decrease only aerodynamic drag but also rolling resistance depending on reduced downforce.
- With this study, deflectors can be a remedy for improving vehicle efficiency. Considering the heavy batteries of EVs, the driving range can be extended and increased lift can be compensated by the weight of batteries without sacrificing downforce.
- In future work, experimental validation of the numerical study performed in this study can be done and deflector usage can be tested for a more realistic model configuration with wheel and mirror inclusion.

REFERENCES

Ahmed, S.R., Ramm, G., and Faltin, G., 1984. Some salient features of the time-averaged ground vehicle wake. SAE Technical Papers in . doi:10.4271/840300

Aktas, U., and Abdallah, K., 2017. Aerodynamics Concept Study of Electric Vehicles. Chalmers University of Technology / Department of Applied Mechanics. http://publications.lib.chalmers.se/records/fulltext/251548/251548.pdf from retrieved.

Anderson, J.D., 1997. A history of aerodynamics and its impact on flying machines. Cambridge University Press. from https://books.google.com/books/about/A_History_of_Aerodynamics.html?hl=tr&id=m9VfQgAACAAJ.

ANSYS, I., 2013. ANSYS Fluent Adjoint Solver Manual.

Aronson, D., Brahim, S. Ben, and Perzon, S., 2000. On the Underbody Flow of a Simplified Estate. SAE Technical Papers. doi:10.4271/2000-01-0485

Ashton, N., and Revell, A., 2014. Investigation into the predictive capability of advanced Reynolds-Averaged Navier-Stokes models for the DrivAer automotive model. The International Vehicle Aerodynamics Conference in (ss. 125–137). Elsevier. doi:10.1533/9780081002452.4.125

Ashton, N., West, A., Lardeau, S., and Revell, A., 2016. Assessment of RANS and DES methods for realistic automotive models. Computers and Fluids, 128, 1–15. doi:10.1016/j.compfluid.2016.01.008

Ashton, Neil, and Revell, A., 2015. Comparison of RANS and des methods for the DrivAer automotive body. SAE Technical Papers in (C. 2015-April). SAE International. doi:10.4271/2015-01-1538

Avadiar, T., Thompson, M.C., Sheridan, J., and Burton, D., 2019. The influence of reduced Reynolds number on the wake of the DrivAer estate vehicle. Journal of Wind Engineering and Industrial Aerodynamics, 188, 207–216. doi:10.1016/j.jweia.2019.02.024

Baek, S.W., and Lee, S.W., 2020. Aerodynamic drag reduction on a realistic vehicle using continuous blowing. Microsystem Technologies, 26(1), 11–23. doi:10.1007/s00542-019-04355-w

Baker, N., Kelly, G., and O’Sullivan, P.D., 2020. A grid convergence index study of mesh style effect on the accuracy of the numerical results for an indoor airflow profile. International Journal of Ventilation, 19(4), 300–314. doi:10.1080/14733315.2019.1667558

Balafas, G., 2014. Polyhedral Mesh Generation for CFD-Analysis of Complex Structures. from http://www.cie.bgu.tum.de/publications/masterthesis/2014_Balafas.pdf.

Ballerstein, N., and Horst, P., 2023. Manipulation of the aerodynamic behavior of the DrivAer model using dimple patterns. Journal of Wind Engineering and Industrial Aerodynamics, 233(January), 105216. doi:10.1016/j.jweia.2022.105216

Bayındrılı, C., Çelik, M., and Demiralp, M., 2018. Bir Otobüs Modeli Etrafındaki Akış Yapısının CFD Yöntemi İle İncelenmesi ve Sürükleme Kuvvetinin Pasif Akış Kontrol Yöntemi İle İyileştirilmesi. Journal of Polytechnic. doi:10.2339/politeknik.403993

Beaudoin, J.F., and Aider, J.L., 2008. Drag and lift reduction of a 3D bluff body using flaps. Experiments in Fluids, 44(4), 491–501. doi:10.1007/s00348-007-0392-1

Carr, G.W., 1982. Correlation of aerodynamic force measurements in MIRA and other automotive wind tunnels. SAE Technical Papers. doi:10.4271/820374

Celik, I.B., Ghia, U., Roache, P.J., Freitas, C.J., Coleman, H., and Raad, P.E., 2008. Procedure for estimation and reporting of uncertainty due to discretization in CFD applications. Journal of Fluids Engineering, Transactions of the ASME, 130(7), 0780011–0780014. doi:10.1115/1.2960953

Cengel, Y., and Cimbala, J., 2006. Fluid Mechamics: Fundamentals and Application. McGraw-Hill, 342.

Cheng, S.Y., Chin, K.Y., Mansor, S., and Abd Rahman, A.B., 2019. Experimental study of yaw angle effect on the aerodynamic characteristics of a road vehicle fitted with a rear spoiler. Journal of Wind Engineering and Industrial Aerodynamics, 184(November 2018), 305–312. doi:10.1016/j.jweia.2018.11.033

Cheng, S.Y., Mansor, S., Abdullah, M.A., and Zakaria, M.S., 2018. Numerical study of aerodynamic performance of hatchback vehicle fitted with a strip spoiler: Effect of yaw angle. Journal of Advanced Research in Fluid Mechanics and Thermal Sciences, 47(1), 108–118.

Cho, J., Park, J., Yee, K., and Kim, H.L., 2018. Comparison of Various Drag Reduction Devices and Their Aerodynamic Effects on the DrivAer Model. SAE International Journal of Passenger Cars - Mechanical Systems, 11(3), 225–238. doi:10.4271/06-11-03-0019

Christian Bach Rasmussen, and Lasse Mose Lund, 2018. Race Car Aerodynamic Design and Optimization via CFD and the Discrete Adjoint Method. www.en.esbjerg.aau.dk from retrieved.

D’Hooge, A., Palin, R.B., Johnson, S., Johnston, V., Duncan, B., and Gargoloff, J.I., 2012. The aerodynamic development of the Tesla Model S-Part 2: Wheel design optimization. SAE Technical Papers. doi:10.4271/2012-01-0178

Davidson, L., 2016. Assessment of Turbulence Models for Flow Simulation Around the Ahmed Body. Annual Review of Fluid Mechanics, 32(1), 1–32.

Dobrev, I., and Massouh, F., 2014. Investigation of relationship between drag and lift coefficients for a generic car model. Science Arts & Métiers (SAM), 171–174.

Edwige, S., Gilotte, P., and Mortazavi, I., 2022. Computational Analysis of Actuation Techniques Impact on the Flow Control around the Ahmed Body. Fluids, 7(2), 1–21. doi:10.3390/fluids7020052

ERCOFTAC - Home (y.y.). 16 March 2022, retrieved from https://www.ercoftac.org/.

Fabijanic, J., 1996. An Experimental Investigation of Wheel-Well Flows. SAE Technical Papers. doi:10.4271/960901

Fotiadis, G., Skaperdas, V., Iordanidis, A., and Peddiraju, P., 2015. The influence of mesh characteristics on external airflow CFD simulations of the DrivAer model. AMS Seminar Series.

Fourrié, G., Keirsbulck, L., Labraga, L., and Gilliéron, P., 2011. Bluff-body drag reduction using a deflector. Experiments in Fluids, 50(2), 385–395. doi:10.1007/s00348-010-0937-6

Goldberg, D.E., and Holland, J.H., 1989. Genetic Algorithms in Search, Optimization, and Machine Learning. Addison-Wesley Longman (Wesley Lon.). Boston. from https://books.google.com/books/about/Genetic_Algorithms_in_Search_Optimizatio.html?hl=tr&id=2IIJAAAACAAJ.

Guerrero, A., Castilla, R., and Eid, G., 2022. A Numerical Aerodynamic Analysis on the Effect of Rear Underbody Diffusers on Road Cars. Applied Sciences (Switzerland), 12(8). doi:10.3390/app12083763

Guilmineau, E., Deng, G.B., Leroyer, A., Queutey, P., Visonneau, M., and Wackers, J., 2018. Assessment of hybrid RANS-LES formulations for flow simulation around the Ahmed body. Computers and Fluids, 176, 302–319. doi:10.1016/j.compfluid.2017.01.005

Guilmineau, Emmanuel, 2014. Numerical Simulations of Flow around a Realistic Generic Car Model. SAE International Journal of Passenger Cars - Mechanical Systems, 7(2), 646–653. doi:10.4271/2014-01-0607

Hanfeng, W., Yu, Z., Chao, Z., and Xuhui, H., 2016a. Aerodynamic drag reduction of an Ahmed body based on deflectors. Journal of Wind Engineering and Industrial Aerodynamics, 148, 34–44. doi:10.1016/j.jweia.2015.11.004

Hanfeng, W., Yu, Z., Chao, Z., and Xuhui, H., 2016b. Aerodynamic drag reduction of an Ahmed body based on deflectors. Journal of Wind Engineering and Industrial Aerodynamics, 148, 34–44. doi:10.1016/j.jweia.2015.11.004

He, P., Mader, C.A., Martins, J.R.R.A., and Maki, K.J., 2018. An aerodynamic design optimization framework using a discrete adjoint approach with OpenFOAM. Computers and Fluids, 168, 285–303. doi:10.1016/j.compfluid.2018.04.012

Heft, A.I., Indinger, T., and Adams, N.A., 2012a. Introduction of a new realistic generic car model for aerodynamic investigations. SAE Technical Papers in . SAE International. doi:10.4271/2012-01-0168

Heft, A.I., Indinger, T., and Adams, N.A., 2012b. Experimental and numerical investigation of the drivaer model. American Society of Mechanical Engineers, Fluids Engineering Division (Publication) FEDSM (C. 1). doi:10.1115/FEDSM2012-72272

Hojjat, M., Stavropoulou, E., and Bletzinger, K.U., 2014. The Vertex Morphing method for node-based shape optimization. Computer Methods in Applied Mechanics and Engineering, 268, 494–513. doi:10.1016/J.CMA.2013.10.015

Holland, J.H., (y.y.). Adaptation in Natural and Artificial Systems. MIT Press. Cambridge. doi:10.7551/mitpress/1090.001.0001

Howell, J., and Hickman, D., 1997. The influence of ground simulation on the aerodynamics of a simple car model. SAE Technical Papers. doi:10.4271/970134

Hucho, W.-H., 2000. Hucho: Vehicle aerodynamics: present status and future development. Proceedings of the 3rd MIRA international vehicle aerodynamics conference in . UK.

Huminic, A., and Huminic, G., 2010. Computational study of flow in the underbody diffuser for a simplified car model. SAE Technical Papers. doi:10.4271/2010-01-0119

Huminic, A., and Huminic, G., 2012. Numerical flow simulation for a generic vehicle body on wheels with variable underbody diffuser. SAE Technical Papers in . SAE International. doi:10.4271/2012-01-0172

Huminic, A., and Huminic, G., 2017. Aerodynamic study of a generic car model with wheels and underbody diffuser. International Journal of Automotive Technology, 18(3), 397–404. doi:10.1007/s12239-017-0040-6

Jowsey, L., and Passmore, M., 2010. Experimental study of multiple-channel automotive underbody diffusers. Proceedings of the Institution of Mechanical Engineers, Part D: Journal of Automobile Engineering, 224(7), 865–879. doi:10.1243/09544070JAUTO1339

Katz, J., 1995. Race Car Aerodynamics : Designing for Speed. Bentley Publishers. Cambridge: Bentley Publishers.

Katz, J., 2016. Automotıve Aerodynamıcs. Wiley. John Wiley & Sons, Ltd.

Kim, D., Lee, H., Yi, W., and Choi, H., 2016. A bio-inspired device for drag reduction on a three-dimensional model vehicle. Bioinspiration and Biomimetics, 11(2), 0. doi:10.1088/1748-3190/11/2/026004

Kurec, K., Kamieniecki, K., and Piechna, J., 2022. Influence of Different Plates Arrangements on the Car Body. Energies, 15(2). doi:10.3390/en15020619

Lanfrit, M., 2005. Best practice guidelines for handling Automotive External Aerodynamics with Fluent.

Lång, M., 2019. CFD-Method for 3D Aerodynamic Adjoint Simulations For External Automotive Aerodynamics. www.liu.se from retrieved.

Le Good, G.M., and Garry, K.P., 2004. On the use of reference models in automotive aerodynamics. SAE Technical Papers. doi:10.4271/2004-01-1308

Lee, S.W., 2018. Computational analysis of air jet wheel deflector for aerodynamic drag reduction of road vehicle. Microsystem Technologies, 24(11), 4453–4463. doi:10.1007/s00542-018-3992-1

Mack, S., Indinger, T., Adams, N.A., Blume, S., and Unterlechner, P., 2012. The interior design of a 40% scaled drivaer body and first experimental results. American Society of Mechanical Engineers, Fluids Engineering Division (Publication) FEDSM in (C. 1, ss. 75–90). doi:10.1115/FEDSM2012-72371

Manshadi, M.D., and Aghajanian, S., 2018. Computational aerodynamic optimization of wing-design concept at supersonic conditions by means of the response surface method. Journal of the Brazilian Society of Mechanical Sciences and Engineering, 40(5), 1–15. doi:10.1007/s40430-018-1150-4

Menter, F., 1992. Improved two-equation k-omega turbulence models for aerodynamic flows. NASA Technical Memorandum, (103978), 1–31.

Miao, L., Mack, S., and Indinger, T., 2015. Experimental and numerical investigation of the DrivAer model. Proceedings of the ASME 2012 Fluids Engineering Summer Meeting in (ss. 1–8). Boston, Massachusetts, USA.

Mock, P., Kühlwein, J., Tietge, U., Franco, V., Bandivadekar, A., and German, J., 2014. The WLTP: How a new test procedure for cars will affect fuel consumption values in the EU. ICCT White Paper, 2014(9), 1–20. from http://www.theicct.org/sites/default/files/publications/ICCT_WLTP_EffectEU_20141029.pdf.

Mohammadikalakoo, B., Schito, P., and Mani, M., 2020. Passive flow control on Ahmed body by rear linking tunnels. Journal of Wind Engineering and Industrial Aerodynamics, 205. doi:10.1016/j.jweia.2020.104330

Morel, T., 1978. Aerodynamic drag of bluff body shapes characteristic of hatch-back cars. SAE Technical Papers. doi:10.4271/780267

Munoz-Paniagua, J., García, J., Crespo, A., and Laspougeas, F., 2015. Aerodynamic Optimization of the Nose Shape of a Train Using the Adjoint Method. Journal of Applied Fluid Mechanics, 8(3), 601–612. doi:10.18869/acadpub.jafm.67.222.22632

Nabutola, K.L., and Boetcher, S.K.S., 2021. Assessment of conventional and air-jet wheel deflectors for drag reduction of the DrivAer model. Advances in Aerodynamics, 3(1). doi:10.1186/s42774-021-00086-7

Othmer, C., 2014. Adjoint methods for car aerodynamics. Journal of Mathematics in Industry, 4(1), 1–23. doi:10.1186/2190-5983-4-6

Othmer, C., Papoutsis-Kiachagias, E.M., and Haliskos, K., 2011. CFD OPTIMIZATION VIA Sensıtıvıty-Based Shape Morphıng. 4th ANSA & μETA International Conference CFD in .

Palin, R., Johnston, V., Johnson, S., D'Hooge, A., Duncan, B., and Gargoloff, J.I., 2012. The aerodynamic development of the Tesla model S-part 1: Overview. SAE Technical Papers in . SAE International. doi:10.4271/2012-01-0177

Papoutsis-Kiachagias, E.M., Asouti, V.G., Giannakoglou, K.C., Gkagkas, K., Shimokawa, S., and Itakura, E., 2019. Multi-point aerodynamic shape optimization of cars based on continuous adjoint. Structural and Multidisciplinary Optimization, 59(2), 675–694. doi:10.1007/S00158-018-2091-3/Fıgures/22

Porcar, L., Toet, W., and Gamez-Montero, P.J., 2021. Study of the effect of vertical airfoil endplates on diffusers in vehicle aerodynamics. Designs, 5(3). doi:10.3390/designs5030045

Pujals, G., Depardon, S., and Cossu, C., 2010. Drag reduction of a 3D bluff body using coherent streamwise streaks. Experiments in Fluids, 49(5), 1085–1094. doi:10.1007/s00348-010-0857-5

Read, C., and Viswanathan, H., 2020. An aerodynamic assessment of vehicle-side wall interaction using numerical simulations. International Journal of Automotive and Mechanical Engineering, 17(1), 7587–7598. doi:10.15282/IJAME.17.1.2020.08.0563

Roache, P.J., 1997. Quantification of uncertainty in computational fluid dynamics. Annual Review of Fluid Mechanics, 29, 123–160. doi:10.1146/annurev.fluid.29.1.123

Saraf, A.K., Singh, D.M.P., and Chouhan, D.T.S., 2017. Effect of Dimple on Aerodynamic Behaviour of Airfoil. International Journal of Engineering and Technology, 9(3), 2268–2277. doi:10.21817/ijet/2017/v9i3/1709030335

Schlichting, H., and Gersten, K., 2016. Boundary-Layer Theory. Boundary-Layer Theory. Springer Berlin Heidelberg. doi:10.1007/978-3-662-52919-5

Shaharuddin, N.H., Ali, M.S.M., Mansor, S., Muhamad, S., and Zaki, S.A., 2018. Numerical study for flow over a realistic generic model, DrivAer, using URANS. Journal of Advanced Research in Fluid Mechanics and Thermal Sciences, 48(2), 183–195. from www.akademiabaru.com/arfmts.html.

Siddiqui, N.A., and Chaab, M.A., 2020. A Simple Passive Device for the Drag Reduction of an Ahmed Body. Journal of Applied Fluid Mechanics, 14(1), 147–164. doi:10.47176/jafm.14.01.31791

Şimşek, O., 2020. Üstten Akişli Kapak Akiminin Sayisal Modellemesi. Mühendislik Bilimleri ve Tasarım Dergisi, 8(3), 808–819. doi:10.21923/jesd.752914

Single, P.I., By, L., R, L.F., Interpenetrating, P.I.I., By, L., and G, J.A., 1927. VIII. The deferred approach to the limit. Philosophical Transactions of the Royal Society of London. Series A, Containing Papers of a Mathematical or Physical Character, 226(636–646), 299–361. doi:10.1098/rsta.1927.0008

Soares, Renan F., Garry, K.P., and Holt, J., 2017. Comparison of the Far-Field Aerodynamic Wake Development for Three DrivAer Model Configurations using a Cost-Effective RANS Simulation. SAE Technical Papers in (C. 2017-March). doi:10.4271/2017-01-1514

Soares, Renan Francisco, and De Souza, F.J., 2015a. Tailpipe Position over a Realistic 3D Road Car Model: The Effect on Drag Coefficient. SAE Technical Papers, 2015-Septe(September). doi:10.4271/2015-36-0522

Soares, Renan Francisco, and De Souza, F.J., 2015b. Influence of CFD Setup and Brief Analysis of Flow over a 3D Realistic Car Model. SAE Technical Papers, 2015-Septe(September). doi:10.4271/2015-36-0513

Soares, Renan Francisco, and De Souza, J.L.F., 2015c. Tailpipe Position over a Realistic 3D Road Car Model: The Effect on Drag Coefficient Copyright. SAE Technical Paper Series.

Soso, M.D., and Wilson, P.A., 2006. Aerodynamics of a wing in ground effect in generic racing car wake flows. Proceedings of the Institution of Mechanical Engineers, Part D: Journal of Automobile Engineering, 220(1), 1–13. doi:10.1243/095440705X69632

Stern, F., Wilson, R. V., Coleman, H.W., and Paterson, E.G., 2001. Comprehensive approach to verification and validation of CFD simulations—Part 1: Methodology and procedures. Journal of Fluids Engineering, Transactions of the ASME, 123(4), 793–802. doi:10.1115/1.1412235

Sukri, M., Ali, M., Doolan, C.J., and Wheatley, V., 2009. Grid Convergence Study for a Two-Dimensional Simulation of Flow Around a Square Cylinder At a Low Reynolds Number. Seventh International Conderence on CFD in the Minerals and Process Industries CSIRO, (December), 1–6.

Taiming, H., Xiaodong, Z., Zhongmin, W., and Zhengqi, G., 2020. Experimental and numerical investigations of the vehicle aerodynamic drag with single-channel rear diffuser. Proceedings of the Institution of Mechanical Engineers, Part D: Journal of Automobile Engineering, 234(8), 2216–2227. doi:10.1177/0954407019893849

Theissen, P., Wojciak, J., Heuler, K., Demuth, R., Indinger, T., and Adams, N., 2011. Experimental investigation of unsteady vehicle aerodynamics under time-dependent flow conditions - Part 1. SAE 2011 World Congress and Exhibition in . doi:10.4271/2011-01-0177

Tunay, T., Yaniktepe, B., and Sahin, B., 2016. Computational and experimental investigations of the vortical flow structures in the near wake region downstream of the Ahmed vehicle model. Journal of Wind Engineering and Industrial Aerodynamics, 159, 48–64. doi:10.1016/j.jweia.2016.10.006

Tzanakis, A., 2014. Duct optimization using CFD software “ANSYS Fluent Adjoint Solver”. Chalmers University of Technology.

Viswanathan, H., 2021. Aerodynamic performance of several passive vortex generator configurations on an Ahmed body subjected to yaw angles. Journal of the Brazilian Society of Mechanical Sciences and Engineering, 43(3). doi:10.1007/s40430-021-02850-8

Wang, S., Avadiar, T., Thompson, M.C., and Burton, D., 2019. Effect of moving ground on the aerodynamics of a generic automotive model: The DrivAer-Estate. Journal of Wind Engineering and Industrial Aerodynamics, 195, 104000. doi:10.1016/j.jweia.2019.104000

Wang, Y., Wu, C., Tan, G., and Deng, Y., 2017. Reduction in the aerodynamic drag around a generic vehicle by using a non-smooth surface. Proceedings of the Institution of Mechanical Engineers, Part D: Journal of Automobile Engineering, 231(1), 130–144. doi:10.1177/0954407016636970

Wieser, D., Nayeri, C.N., and Paschereit, C.O., 2015. Experiments with vortex generators applied to a notchback car model. 53rd AIAA Aerospace Sciences Meeting in . American Institute of Aeronautics and Astronautics Inc, AIAA. doi:10.2514/6.2015-1236

Wieser, Dirk, Lang, H., Nayeri, C., and Paschereit, C., 2015. Manipulation of the Aerodynamic Behavior of the DrivAer Model with Fluidic Oscillators. SAE International Journal of Passenger Cars - Mechanical Systems, 8(2), 687–702. doi:10.4271/2015-01-1540

Wilcox, D.C., 2006. Turbulence Modeling for CFD. DCW Industries ((Third Edi.). La Canada, CA: DCW Industries.

Wittmeier, F., and Kuthada, T., 2015. Open Grille DrivAer Model - First Results. SAE International Journal of Passenger Cars - Mechanical Systems, 8(1), 252–260. doi:10.4271/2015-01-1553

Wojciak, J., Theissen, P., Heuler, K., Indinger, T., Adams, N., and Demuth, R., 2011. Experimental investigation of unsteady vehicle aerodynamics under time-dependent flow conditions - Part2. SAE 2011 World Congress and Exhibition in . doi:10.4271/2011-01-0164

Woodiga, S., Howard, K., Norman, P., Lewington, N., Carstairs, R., Hupertz, B., and Chalupa, K., 2020. The GTU: A New Realistic Generic Pickup Truck and SUV Model. SAE Technical Papers, 2020-April(April). doi:10.4271/2020-01-0664

Yang, X., Hu, Y., Gong, Z., Jian, J., and Liu, Z., 2022. Numerical Study of Combined Drag Reduction Bases on Vortex Generators and Riblets for the Ahmed Body using IDDES Methodology. Journal of Applied Fluid Mechanics, 15(1), 193–207. doi:10.47176/jafm.15.01.32832

Yazdani, R., 2015. Steady and Unsteady Numerical Analysis of the DrivAer Model. Chalmers University of Technology.

Yılmaz, N., and Çiçek, İ., 2017. Standart Test Pervanesi Analizleri ile Hesaplamalı Akişkanlar Dinamiği Analiz Altyapisinin Doğrulanmasi. Mühendislik Bilimleri ve Tasarım Dergisi, 6(4), 681–690. doi:10.21923/jesd.400115

Yu, X., Jia, Q., Bao, D., and Yang, Z., 2018. A Comparative Study of Different Wheel Rotating Simulation Methods in Automotive Aerodynamics. SAE Technical Papers in (C. 2018-April). SAE International. doi:10.4271/2018-01-0728

Yu, Z., 2009. Automobile theory. Bejing, China 30ya: China Machine Press. from https://scholar.google.com/scholar_lookup?title=Automobile+Theory&author=Yu,+Z.&publication_year=2019.

Zaya, J., 2013. Aerodynamic Optimization of Ground Vehicles with the Use of Fluent's Adjoint Solver. Chalmers University of Technology.

Zhang, Chenyi, Tanneberger, M., Kuthada, T., Wittmeier, F., Wiedemann, J., and Nies, J., 2019. Introduction of the AeroSUV-A New Generic SUV Model for Aerodynamic Research. SAE Technical Papers, 2019-April(April). doi:10.4271/2019-01-0646

Zhang, Chunhui, Bounds, C.P., Foster, L., and Uddin, M., 2019. Turbulence modeling effects on the CFD predictions of flow over a detailed full-scale sedan vehicle. Fluids, 4(3). doi:10.3390/fluids4030148

CURRICULUM VITAE

Oğuz BAŞ, graduated from Hacı Mehmet Uçar Primary School in 2006 and graduated from Ankara Bahçelievler Anatolian High School in 2010. Then, he started his BSc degree in 2010 at Çukurova University, Automotive Engineering Department. He started his MSc education in the Automotive Engineering Department of Çukurova University in 2015 and graduated from the MSc in this department in 2018. Then, he started his Ph.D. education in the Automotive Engineering Department of Çukurova University in 2018. He has been working as Research Assistant at Amasya University, Mechanical Engineering Department since March 2016.